Modeling, Optimization and Estimation in Electric Arc Furnace (EAF) Operation

Modeling, Optimization and Estimation in Electric Arc Furnace (EAF) Operation

by

Yasser Emad Moustafa Ghobara, B.Eng

A Thesis
Submitted to the School of Graduate Studies
in Partial Fulfillment of the Requirements
for the Degree
Master of Applied Science

McMaster University

MASTER OF APPLIED SCIENCE (2013) McMaster University

(Chemical Engineering) Hamilton, Ontario, Canada

TITLE:	Modeling, Optimization and Estimation in Electric Arc Furnace (EAF) Operation
AUTHOR:	Yasser Emad Moustafa Ghobara, B.Eng (McMaster University, Canada)
SUPERVISOR:	Dr. Christopher L.E. Swartz
NUMBER OF PAGES:	xx, 140

ABSTRACT

The electric arc furnace (EAF) is a highly energy intensive process used to convert scrap metal into molten steel. The aim of this research is to develop a dynamic model of an industrial EAF process, and investigate its application for optimal EAF operation. This work has three main contributions; the first contribution is developing a model largely based on MacRosty and Swartz [2005] to meet the operation of a new industrial partner (ArcelorMittal Contrecoeur Ouest, Quebec, Canada). The second contribution is carrying out sensitivity analyses to investigate the effect of the scrap components on the EAF process. Finally, the third contribution includes the development of a constrained multi-rate extended Kalman filter (EKF) to infer the states of the system from the measurements provided by the plant.

A multi-zone model is developed and discussed in detail. Heat and mass transfer relationships are considered. Chemical equilibrium is assumed in two of the zones and calculated through the minimization of the Gibbs free energy. The most sensitive parameters are identified and estimated using plant measurements. The model is then validated against plant data and has shown a reasonable level of accuracy.

Local differential sensitivity analysis is performed to investigate the effect of scrap components on the EAF operation. Iron was found to have the greatest effect amongst the components present. Then, the optimal operation of the furnace is determined through economic optimization. In this case, the trade-off between electrical and chemical energy is determined in order to maximize the profit. Different scenarios are considered that include price variation in electricity, methane and oxygen.

A constrained multi-rate EKF is implemented in order to estimate the states of the system using plant measurements. The EKF showed high performance in tracking the true states of the process, even in the presence of a parametric plant-model mismatch.

ACKNOWLEDGEMENTS

I wish to express my sincere gratitude to my supervisor Dr. Christopher L.E. Swartz for his continued support and guidance throughout the course of this research project. Without Dr. Swartz's vision and guidance, this project would have never been successful. I am really honoured to have him as my supervisor.

I am also grateful to Dr. Gordon Irons and John Thompson for their valuable ideas and support in this project. Additionally, I would like to acknowledge the McMaster Steel Research Center (SRC), ArcelorMittal Contrecoeur Ouest and the Department of Chemical Engineering at McMaster University for their financial support.

I would like to thank all my professors who provided me with a solid academic foundation that helped me progress throughout this project especially, Kevin Dunn, Dr. Tom Adams and Dr. Prashant Mhaskar. I appreciate Kathy Goodram and Lynn Falkiner's administrative efforts and Dan Wright for his technical support.

A special thanks goes out to Zhiwen Chong, Yanan Cao, Tinoush Sheikhzeinoddin and Ian Washington for their support and help during this project. Also, I would like to thank my penthouse friends Alicia, Jaffer, Jake, Yaser, Chris, Matt, Ali, Brandon, Dominik and Chinedu for their moral support and making my graduate life experience memorable.

Finally, I want to thank my father Emad Ghobara, my brother Youssef Ghobara and my grandparents, Hafez Higgy and Nadia Higgy, for everything they have contributed in my life to reach this achievement. I am grateful for having my Uncle Khaled Higgy who made my stay in Canada remarkable.

This thesis is dedicated to my mother, Randa Higgy, for her continued suffering and support, without her I definitely would have never reached this point in my life.

Table of Contents

1 Introduction **1**

1.1 Process Overview 2

1.2 Motivation and Goals 3

1.3 Main Contributions 4

1.4 Thesis overview 4

2 Literature Review **7**

2.1 Modeling, optimization and control of EAF operation 8

2.1.1 Modeling Approaches 8

2.1.2 Economic Optimization 12

2.1.3 EAF Control Applications 14

2.2 Dynamic Optimization 16

2.3 Sensitivity Analysis and Parameter Estimability 18

2.4 Parameter Estimation 21

2.5 State Estimation 23

3 Mathematical Model **26**

3.1 Model Formulation 26

3.1.1 Solid Zone 27

3.1.2 Molten Metal Zone 31

3.1.3 Gas Zone 35

3.1.4 Roof and Walls 39

3.2 Slag-Metal Interaction Zone 40

3.2.1 Material Balance 41

3.2.2 Slag foaming 42

3.2.3 Energy Balance 44

3.3 JetBox Modeling 45

3.4 Radiation Model 46

3.4.1 Effect of slag foaming 49

3.5 Assumption regarding the melt rate 51

3.6 Comparing different melting scrap geometry 54

3.7 Simulation Studies 57

4 Parameter Estimation, Sensitivity Analysis and Economic Optimization **63**

4.1 Parameter Estimation and Model Validation 63

4.1.1 Sensitivity Analysis 64

4.2 Parameter Estimation 71

4.2.1 Raw Data 73

4.2.2 Maximum Likelihood Function 73

4.2.3 Model Estimation Results 75

4.3 Sensitivity Analysis on Scrap Composition 78

4.3.1 Effect of scrap composition on offgas chemistry 79

4.3.2 Effect of scrap composition on slag composition 81

4.3.3 Effect of scrap composition on zone temperatures and molten metal carbon content 83

4.4 Dynamic Optimization 87

4.4.1 Formulation 87

4.4.2 Case Studies 89

4.4.3 Results 90

5 State Estimation **94**

5.1 State Estimation 95

5.1.1 Kalman Filter 95

5.1.2 Extended Kalman Filter (EKF) 96

5.1.3 States 98
5.1.4 Measurement Structure 100
5.2 Implementing a constrained-multirate EKF 100
5.2.1 Linearization 100
5.2.2 Observability Analysis: 102
5.2.3 Plant and Estimator Models 104
5.2.4 Constrained multi-rate EKF 105
5.2.5 State augmentation and disturbance rejection 108
5.3 Results and Discussion 110
5.3.1 Observability 110
5.3.2 Case Study 1 110
5.3.3 Frequent molten metal temperature measurements 119
5.3.4 Case Study 2 120

6 Conclusions and Recommendations 129

6.1 Conclusions 129
6.2 Recommendations for Further Work 130
6.2.1 Modeling Approach 131
6.2.2 Optimization 131
6.2.3 State Estimation and Control 132

References **133**

A Modeling Details **141**

A.1 Molten Metal Temperature 141

A.2 Offgas flow rate and entrained air 142

A.3 Total Carbon entering the slag-metal interaction zone 143

A.4 Water entering the gas zone 143

A.5 View Factors Calculations 144

A.5.1 Roof 144

A.5.2 Wall 145

A.5.3 Scrap 146

A.5.4 Molten Metal 147

A.5.5 Arc 147

A.6 Procedure for normalizing the trajectories 149

B Parameter Estimation **150**

C State Estimation **152**

C.1 Converting DAE system to ODE state space model using linearization 152

C.2 Local Observability Results 154

C.3 EKF parameters 158

C.3.1 Tuning parameters 158

C.3.2 Constraints 160

C.3.3 Initial Conditions 161

C.4 EKF Trajectories 162

C.4.1 Case Study 1 162

C.4.2 Frequent molten metal temperature measurements on Case Study 1 168

C.4.3 Case Study 2 181

List of Figures

1.1 Electric Arc Furnace Operation 2

3.1 Schematic diagram of the EAF model (MacRosty and Swartz [2005]) 27

3.2 JetBox Diagram (Brhel [2002]) 46

3.3 EAF surfaces 50

3.4 Comparing the trajectories for term1 representing $[\Delta H_{fusion}\frac{T_{melt}}{T_{ss}}]$ and term2 representing $([\Delta H_{fusion} + C_p(T_{melt} - T_{ss}]\frac{T_{melt}}{T_{ss}})$ 52

3.5 Mass of solid scrap in the furnace 53

3.6 Melting rate of scrap 53

3.7 Temperature of the gas zone 55

3.8 Mass of solid scrap in the furnace 55

3.9 Temperature of the roof of the furnace 56

3.10 Temperature of the wall of the furnace 56

3.11 Active power trajectory 57

3.12 JetBox trajectories 58

3.13 Natural gas trajectory 60

3.14 Temperature trajectories 60

3.15 Mass of Scrap and Molten Metal trajectories 61

3.16 Offgas composition trajectories 61

3.17 Roof and Wall temperature trajectories 62

3.18 Foam height trajectory 62

4.1 Sensitivity analysis on the molten metal zone 67

4.2 Sensitivity analysis on the offgas composition 68

4.3 Sensitivity analysis on the slag-metal zone 69

4.4 Sensitivity analysis on the gas and scrap temperatures 70

4.5 Sensitivity analysis on combined measurements 71

4.6 Normalized Offgas Chemistry Predictions 76

4.7 Slag Composition Predictions 77

4.8 Molten Metal Temperature Prediction 77

4.9 Effect of scrap composition and fluxes on offgas chemistry 80

4.10 Effect of Scrap components on CO offgas composition 81

4.11 Effect of scrap composition and fluxes on Slag chemistry 82

4.12 Effect of scrap components on FeO slag composition 83

4.13 Effect of scrap composition on the zones temperatures and molten metal carbon content 84

4.14 Effect of Fe in scrap on the solid scrap zone temperature 85

4.15 Effect of scrap components on the molten metal carbon content . . . 86

4.16 Overall effect of scrap composition on the EAF operation 87

4.17 Active Power Optimized Trajectories 90

4.18 Methane Optimized Trajectories 91

4.19 JetBox1 Optimized Trajectory 92

4.20 JetBox2 Optimized Trajectory 92

4.21 JetBox3 Optimized Trajectory 93

5.1 The flow between the plant, estimator and estimator model 105

5.2 Interfacing gPROMS and *Matlab*® using gO:MATLAB tool 106

5.3 Multi-rate EKF implementation diagram 107

5.4 Gas zone state profiles for the base case (Case Study 1A) without disturbance state augmentation. (×) represents the estimated states while (–) represents the actual states 112

5.5 Slag zone state profiles for the base case (Case Study 1A) without disturbance state augmentation. (×) represents the estimated states while (–) represents the actual states 113

5.6 Molten metal zone state profiles for the base case (Case Study 1A) without disturbance state augmentation. (×) represents the estimated states while (–) represents the actual states 114

5.7 Solid zone state profiles for the base case (Case Study 1A) without disturbance state augmentation. (×) represents the estimated states while (–) represents the actual states 114

5.8 Solid zone state profiles for Case Study 1B with disturbance state augmentation. (×) represents the estimated states while (–) represents the actual states 115

5.9 Gas zone state profiles for Case Study 1B with disturbance state augmentation. (×) represents the estimated states while (–) represents the actual states 116

5.10 Slag zone state profiles for Case Study 1B with disturbance state augmentation. (×) represents the estimated states while (–) represents the actual states 117

5.11 Molten metal zone state profiles for Case Study 1B with disturbance state augmentation. (×) represents the estimated states while (–) represents the actual states 118

5.12 Molten metal temperature trajectories with frequent molten metal temperature measurements 119

5.13 Gas zone state profiles for the Case Study 2A without disturbance state augmentation. (×) represents the estimated states while (–) represents the actual states 122

5.14 Molten metal zone state profiles for the Case Study 2A without disturbance state augmentation. (×) represents the estimated states while (–) represents the actual states 123

5.15 Slag zone state profiles for the Case Study 2A without disturbance state augmentation. (×) represents the estimated states while (–) represents the actual states 124

5.16 Solid zone state profiles for the Case Study 2A without state augmentation. (×) represents the estimated states while (–) represents the actual states 125

5.17 Gas zone state profiles for the Case Study 2B with disturbance state augmentation. (×) represents the estimated states while (–) represents the actual states 126

5.18 Slag zone state profiles for the Case Study 2B with disturbance state augmentation. (×) represents the estimated states while (–) represents the actual states 127

5.19 Molten metal zone state profiles for the Case Study 2B with disturbance state augmentation. (×) represents the estimated states while (–) represents the actual states 128

5.20 Solid zone state profiles for the Case Study 2B with disturbance state augmentation. (×) represents the estimated states while (–) represents the actual states 128

C.1 Slag zone state profiles for the base case (Case Study 1A) without disturbance state augmentation. (×) represents the estimated states while (–) represents the actual states 162

C.2 Gas zone state profiles for the base case (Case Study 1A) without disturbance state augmentation. (×) represents the estimated states while (–) represents the actual states 163

C.3 Solid zone state profiles for the base case (Case Study 1A) without disturbance state augmentation. (×) represents the estimated states while (–) represents the actual states 163

C.4 Molten metal zone state profiles for the base case (Case Study 1A) without disturbance state augmentation. (×) represents the estimated states while (–) represents the actual states 164

C.5 Gas zone state profiles for Case Study 1B with disturbance state augmentation. (×) represents the estimated states while (–) represents the actual states 165

C.6 Solid zone state profiles for Case Study 1B with disturbance state augmentation. (×) represents the estimated states while (–) represents the actual states 166

C.7 Slag zone state profiles for Case Study 1B with disturbance state augmentation. (×) represents the estimated states while (–) represents the actual states 166

C.8 Molten metal zone state profiles for Case Study 1B with disturbance state augmentation. (×) represents the estimated states while (–) represents the actual states 167

C.9 Gas zone state profiles for the base case (Case Study 1A) without disturbance state augmentation using frequent MM.T measurements. (×) represents the estimated states while (–) represents the actual states 168

C.10 Slag zone state profiles for the base case (Case Study 1A) without disturbance state augmentation using frequent MM.T measurements. (×) represents the estimated states while (–) represents the actual states 169

C.11 Molten metal zone state profiles for the base case (Case Study 1A) without disturbance state augmentation using frequent MM.T measurements. (×) represents the estimated states while (–) represents the actual states . . . 170

C.12 Solid zone state profiles for the base case (Case Study 1A) without disturbance state augmentation using frequent MM.T measurements. (×) represents the estimated states while (–) represents the actual states 170

C.13 Gas zone state profiles for the base case (Case Study 1A) without disturbance state augmentation using frequent MM.T measurements. (×) represents the estimated states while (–) represents the actual states 171

C.14 Solid zone state profiles for the base case (Case Study 1A) without disturbance state augmentation using frequent MM.T measurements. (×) represents the estimated states while (–) represents the actual states 171

C.15 Slag zone state profiles for the base case (Case Study 1A) without disturbance state augmentation using frequent MM.T measurements. (×) represents the estimated states while (–) represents the actual states 172

C.16 Molten metal zone state profiles for the base case (Case Study 1A) without disturbance state augmentation using frequent MM.T measurements. (×) represents the estimated states while (–) represents the actual states . . . 173

C.17 Solid zone state profiles for Case Study 1B with disturbance state augmentation using frequent MM.T measurements. (×) represents the estimated states while (–) represents the actual states 174

C.18 Gas zone state profiles for Case Study 1B with disturbance state augmentation using frequent MM.T measurements. (×) represents the estimated states while (–) represents the actual states 175

C.19 Slag zone state profiles for Case Study 1B with disturbance state augmentation using frequent MM.T measurements. (×) represents the estimated states while (–) represents the actual states 176

C.20 Molten metal zone state profiles for Case Study 1B with disturbance state augmentation using frequent MM.T measurements. (×) represents the estimated states while (–) represents the actual states 177

C.21 Gas zone state profiles for Case Study 1B with disturbance state augmentation using frequent MM.T measurements. (×) represents the estimated states while (–) represents the actual states 178

C.22 Solid zone state profiles for Case Study 1B with disturbance state augmentation using frequent MM.T measurements. (×) represents the estimated states while (–) represents the actual states 179

C.23 Slag zone state profiles for Case Study 1B with disturbance state augmentation using frequent MM.T measurements. (×) represents the estimated states while (–) represents the actual states 179

C.24 Molten metal zone state profiles for Case Study 1B with disturbance state augmentation using frequent MM.T measurements. (×) represents the estimated states while (–) represents the actual states 180

C.25 Gas zone state profiles for the Case Study 2A without disturbance state augmentation. (×) represents the estimated states while (–) represents the actual states 181

C.26 Solid zone state profiles for Case Study 2A with disturbance state augmentation. (×) represents the estimated states while (–) represents the actual states 182

C.27 Slag zone state profiles for the Case study 2A without disturbance state augmentation. (×) represents the estimated states while (–) represents the actual states 182

C.28 Molten metal zone state profiles for the Case study 2A without disturbance state augmentation. (×) represents the estimated states while (–) represents the actual states 183

C.29 Gas zone state profiles for the Case Study 2B with disturbance state augmentation. (×) represents the estimated states while (–) represents the actual states 184

C.30 Solid zone state profiles for the Case Study 2B with disturbance state augmentation. (×) represents the estimated states while (–) represents the actual states 185

C.31 Slag zone state profiles for the Case Study 2B with disturbance state augmentation. (×) represents the estimated states while (–) represents the actual states 185

C.32 Molten metal zone state profiles for the Case Study 2B with disturbance state augmentation. (×) represents the estimated states while (–) represents the actual states 186

List of Tables

4.1 Roles of parameters in the model 65

4.2 Most Sensitive Estimated Parameters 74

4.3 Mean Squared Prediction Errors 75

4.4 Optimization summary for the 3 scenarios 93

B.1 Model parameters 151

C.1 Observability Results for Case Study 1B with augmented disturbances 156

Chapter 1

Introduction

Electric Arc Furnaces (EAFs) are used extensively in industry to convert scrap metal into molten steel. EAFs account for approximately one third of the world crude steel production, which approximately reached 1.5 billion tons in 2012 (World Steel Association [2012]). This is a highly energy intensive process and possesses a high degree of complexity. A typical batch consumes approximately 400 kWh/ton of steel (Fruehan [1998]) and modern furnaces are now consuming less than 300 kWh/ton of steel (Irons [2005]). Approximately 60% of the energy consumed by the EAF represents electrical energy and the other 40% accounts for chemical energy resulting from the burner materials and the chemical reactions occurring within the furnace (Matson and Ramirez [1999]). This high energy consumption of the EAF motivates the development of control and optimization strategies that would reduce production costs, while maintaining targeted steel quality (steel grade) and meeting environmental standards (carbon emissions). The high energy intensity during the operation of the furnace limits the number of measurements and makes modeling this process very complicated. Therefore, some assumptions are often made and a lot of uncertainty as a result exists.

1.1 Process Overview

The EAF considered in this work is an AC furnace with a capacity of approximately 100 tons/h. A schematic diagram of the EAF operation is shown in Figure 1.1. The scrap is loaded into the furnace and the roof is then closed, before the electrodes bore down the scrap to transfer electrical energy. Natural gas (CH_4) and oxygen (O_2) are injected into the furnace from the burners which get combusted releasing chemical energy that is also absorbed by the scrap. The scrap keeps melting through absorbing electrical, chemical and radiation energy. When sufficient amount of space is available within the furnace, another scrap charge is added and melting continues until a flat bath of molten steel is formed at the end of the batch. Through the evolution of carbon monoxide from the molten metal a slag layer is formed, which contains most of the oxides resulting from the reactions of the metals with oxygen. Slag chemistry is adjusted through oxygen and carbon lancing, beside some direct addition of carbon, lime and dolomite through the roof of the furnace. Cooling panels are used to cool down the roof and the walls of the furnace, in addition to the gas and molten metal zones. Each batch duration is approximately 60 minutes and two charges of scrap are usually involved within one batch cycle. Online data that are used in this work were obtained in collaboration with ArcelorMittal Contrecoeur Ouest in Quebec, Canada.

Figure 1.1: Electric Arc Furnace Operation

1.2 Motivation and Goals

As discussed earlier, the EAF is a very complex and highly energy intensive process. The EAF process is characterized by a low level of automation and high level of operator involvement. Several steel industries rely on past experience in the operation of their furnaces in terms of the recipes of material addition such as scrap, fluxes, methane, carbon, oxygen and power. Those additions can be performed in several ways and optimizing the correct timing and quantity of the additions can potentially save steel makers a significant amount of money.

The aim of this work is to develop a model that can be used to simulate an industrial EAF process and which can be used to implement different optimization and control strategies. This work builds on previous models found in the literature. This model could be used offline by plant operators to carry out what-if scenarios regarding different batches used by the plant. Also, sensitivity analysis case studies are performed in order to study the effect the scrap composition has on the different outputs from the EAF process. This could be used to predict the behaviour of different types of scrap in the EAF.

After developing a model that represents the complex industrial process, dynamic optimization is carried out which focuses on determining the optimal input profiles to maximize the profit from the process. The main aim of this component of the project is to investigate the capability of the optimizer to capture the trade-off between electrical energy and chemical energy based on their prices.

The EAF process is characterized by the shortage of continuous measurements and therefore not all the states are measured during the operation of the furnace. In order to use this model for real-time applications, state knowledge is always necessary. Therefore, a state observer is implemented to infer the current states of the system at every time step during the batch. An extended Kalman filter was chosen and used

to estimate the states of the process. Through the knowledge of the current states of the process, this could be used by the operator as an advisory tool to determine the optimal input trajectories of the furnace for the remainder of the batch. The first challenge in this area, is that the model developed is a differential-algebraic equation (DAE) model which had to be converted to an ordinary differential equation (ODE) system. The next challenge is dealing with the different sample rates for the measurements, and therefore a constrained multi-rate EKF was implemented to ensure reliable estimates and to accommodate the different measurement sample rates. This is considered to be a novel contribution to EAF operation.

1.3 Main Contributions

This work has three main contributions to EAF modeling and control. The first contribution is refining the model developed by MacRosty and Swartz [2005] to account for the operation of a new industrial partner. The reconfiguration accounts for some new modeling aspects, in addition to some assumptions that were not considered before. The second contribution is carrying out sensitivity analyses on some of the initial conditions in the EAF process such as the scrap components. Such sensitivity case studies help us better understand the conditions of the operation of the furnace and its relation to the outputs of the process model. The third contribution is estimating the internal states of the system using a nonlinear state observer such as the extended Kalman filter, while accounting for the constraints and the different sampling rates of the measurements.

1.4 Thesis overview

Chapter 2 – Literature Review

This chapter starts with a literature review on the current EAF models that have been developed. Previous optimization studies and control applications on EAFs are then reviewed. Sensitivity analysis techniques, as well as parameter estimation strategies are also discussed and reviewed. Finally, previous work on the implementation of an extended Kalman filter (EKF) is reviewed.

Chapter 3 – Mathematical Model

In this chapter, the process model formulation is discussed. The model used in this work is discussed in detail, showing all the relationships involved. Assumptions regarding the melting and radiation parts of the model are presented and validated.

Chapter 4 –Model Validation, Sensitivity Analysis and Optimization

Model validation is presented through parameter estimation and calibration against plant measurements. Sensitivity analysis is conducted to investigate the effect of the scrap composition and flux components on the EAF operation. The optimal operation of the furnace is then identified through dynamic optimization of the EAF process. Different scenarios are considered that include price fluctuations in electricity, methane and oxygen.

Chapter 5 – State Estimation

The formulation of a constrained multi-rate EKF is presented and two different case studies are investigated. The two case studies investigate the ability of the observer to track the true states of the process, while lacking the knowledge of the exact initial conditions. One of the case studies also includes the presence of parametric plant-model mismatch.

Chapter 6 – Conclusions and Recommendations

This final chapter addresses the main results and conclusions. Future potential work is also discussed and the motivation behind it is illustrated.

Chapter 2

Literature Review

The intent of this chapter is to review related previous work in the literature. First, previous EAF models that were developed and published in the open literature will be discussed. The use of the models developed to implement different optimization strategies for EAF operation and investigate optimal control strategies of the EAF will be described. Second, dynamic optimization formulation and methods used to solve such problems will be reviewed. Third, sensitivity analysis approaches to understand the input-output behaviour of dynamic systems will be reviewed. Fourth, parameter estimation techniques will be reviewed and finally a review on the application of state observers to estimate the internal states of dynamic systems will be discussed.

2.1 Modeling, optimization and control of EAF operation

2.1.1 Modeling Approaches

In order to be able to optimize or control a process, a model describing this process needs to be developed. The complexity of the EAF discussed in Chapter 1, motivated researchers to come up with different models that could describe the process to a required level of accuracy. This took into account the heat and mass transfer relationships. Models differed in complexity based on the amount of detail it could capture in the process. Different first principles approaches were taken by researchers to model the EAF batch process. Most of these approaches divided the EAF furnace into different zones or volumes in order to describe the mass and heat transfer within the zones and between each zone and another.

One of the earliest models that described the whole EAF process was developed by Matson and Ramirez [1997], in which the furnace was divided into two control volumes; a gas control volume and another control volume containing the slag, bath and some gas. The gas control volume mainly contained the free-board gases. The scrap was modeled as a surface made up of n identical spheres. Therefore, modeling the heat transfer can be reduced to one sphere, and then it can be scaled up to n spheres. The melting model was comprised of partial differential equations to compute the scrap temperature change and the rate of melting based on the sensible heat and the latent heat of fusion. Compounds of interest were chosen (CO, CO_2, H_2, O_2, N_2 and H_2O) as well as their precursors which included dissolved oxygen and hydrogen in the bath and carbon dissolved in the bath. Chemical equilibrium was assumed within each control volume through the minimization of the Gibbs free energy. Before a material balance was executed, the equilibrium state was calculated and this was to

ensure that equilibrium did exist at all time steps during the simulation. 17 material balances were used to track the transfer of material that were limited by concentration gradients, mass transfer coefficient and contact area. The model was able to predict the offgas chemistry and bath chemistry. A finite difference approach was used to solve the PDEs. The finite difference ODEs were augmented with a melting algorithm. When the temperature of the shell of the sphere reached the melting temperature, the melting algorithm was implemented causing a decrease in the radius of the spheres. At each time step, the temperature profile was monitored which then decides, if the next time step will involve a sensible heating or a melting iteration. The melting algorithm assumed no sensible heat transfer taking place, and as a result small time steps were used to attain a reasonable level of accuracy. Similarly, Bekker *et al.* [1999] developed a dynamic nonlinear ODE EAF model consisting of 14 equations based on first principles thermodynamics for use in a control application for the offgas system. The temperature of the bath, molten slag and gas were assumed to be the same. The model mainly consisted of a solid group, which contains the solid scrap and solid slag from fluxes that have not dissolved, and a fluid group which contains molten metal, molten slag and gas phase. It was assumed that all the heat from the arc is transferred to the molten metal, and a power division coefficient is used to differentiate between the energy available for melting the scrap and that responsible for heating the scrap to the melting temperature. All the oxygen blown into the steel reacts with Fe which is the major component in the bath. It was also assumed that the scrap does not contain any impurities. The CaO and MgO were lumped together in a single state variable. The solid group received energy from the fluid group. Hydrogen was ignored in the offgas composition system. The metallurgical reactions considered included those for C, Si, Fe as well as the reduction of FeO. The reaction rates for carbon and silicon are driven by the difference between their concentrations in the slag and bath and their equilibrium concentrations. Unlike Matson and Ramirez [1997], chemical equilibrium was calculated using reaction kinetics. The model was solved using a 4^{th} order Runge

Kutta fixed step size numerical method.

Modigell *et al.* [2001] developed an EAF model to serve as a simulation tool. The furnace was divided into four main reaction zones which are the molten metal, scrap, metal-slag and post-combustion zones. The scrap zone mainly contains the scrap, and the slag metal zone consists of the slag phase and a part of the metal bath. Chemical equilibrium was assumed in the zones due to the high temperatures which make them not limited by reaction kinetics. The model was validated against offgas composition in addition to end-point measurements. This included end-point bath chemistry in addition to masses of steel, slag and offgas.

Nyssen *et al.* [2004] et al. developed a model for the electric arc furnace, which was divided into fifteen sectors. A sector identifies the location of the scrap within the furnace. Each sector has different rate of melting depending on its location within the furnace and has its specific scrap layers. Ten modules describing the physical parts of the furnace were identified which are the scrap, liquid metal, slag, solidified metal, refractory lining, arc, furnace chamber exhaust gas system, burners and roof and panels modules. Mass and heat exchanges between the modules were considered. The liquid metal bath composition was determined based on the oxidation rates and metal-slag equilibrium. The model also was able to calculate the physical properties of the slag, as well as slag foaming. The model was implemented online at the Arcelor Profil Luxembourg Esch-Belval steelshop.

In contrast to the full EAF models described above, Guo and Irons [2003] developed a three-dimensional radiation model to quantify the radiative energy distribution within the furnace. The model used the power factor, current and voltage to determine the amount of energy radiated from the arc. It distinguished the energy received by a surface from the arc from that from the bath. It also determined the amount of heat extracted by the cooling panels and the roof, and considered the effect of slag foaming on the wall temperature and other parts of the furnace. MacRosty and Swartz [2005]

developed a first principles dynamic DAE model in which the furnace was divided into four main zones; slag-metal interaction zone, molten metal zone, gas zone and solid scrap zone. The authors used some of the conclusions of the work done by Guo and Irons [2003] to model the radiation part in the process. The scrap melting geometry was assumed to form a cone-frustum. Chemical equilibrium was assumed in the slag and gas zones, where chemical reactions take place. Chemical equilibrium was calculated through the minimization of the Gibbs free energy. It was assumed that all the oxygen lanced enters the slag phase and that no chemical reactions occur in the molten metal zone. A constant free-board gas pressure was assumed and was considered the main driving force for the air being ingressed into or expelled from the furnace. All reactions were limited by mass transfer relationships. Slag foaming was calculated through the duration of the batch. This model represents the basis for this research project, in which few modifications are carried out and will be discussed in Chapter 3.

Wendelstorf and Spitzer [2006] identified 7 volumes of the electric arc furnace to be balanced. This included the upper shell, lower shell, liquid metal, solid metal, slag, gas and roof. A system of equations was written based on conservation of mass, momentum and energy. No information was provided regarding the kinetics of the chemical reactions occurring in the furnace. One specific fit parameter was used to describe how the energy is distributed in the EAF system. The model was capable of predicting the tapping temperature and melt-down status to an accuracy depending on the precision of input measurements and the model, which was verified through a sensitivity analysis.

Stankevic *et al.* [2009] developed a mathematical model for calculating the heat and mass transfer relationships during a three phase electric arc furnace operation. A system of equations was formulated based on the conservation of mass, momentum and energy. Lateral radiation flow was also considered to determine the heating of

the melt.

One of the recent models developed in literature is by Logar *et al.* [2012a]. The authors developed a first principles multi-zone dynamic model for an 80 MVA AC furnace using mass and heat transfer relationships. The model used the principles from Bekker *et al.* [1999] and MacRosty and Swartz [2005] models as the basis for the model development and considered the conductive and convective heat transfer between the zones and the CO post combustion. Reaction kinetics were considered in the slag, gas and bath zones. The model illustrated 15 oxidation and reduction chemical reactions taking place. Constant activity coefficients close to 1 were assumed to calculate the chemical equilibrium and an ideal solution was assumed for the slag phase. The model also took into account some aspects such as electrode oxidation and slag foaming.

2.1.2 Economic Optimization

EAF models such as those discussed enabled researchers to identify potential opportunities for improving the EAF process in terms of optimal control. This is usually formulated as an optimization problem, in which some control variables are adjusted in order to maximize or minimize an objective function, which is usually an economic one.

Some of these approaches considered simplified models to apply optimal control strategies. Woodside *et al.* [1970] used a highly simplified model to control the decarburization rate in order to find the optimal power trajectory. A second-order nonlinear model involving two state variables was used, which are the reacted atoms of carbon and temperature. The control inputs represented the input power and the terminal reaction time. The total cost was minimized and some constraints were enforced on the carbon content, temperature and power input. Hard constraints were replaced

by soft constraints. The steepest descent and direct methods were used to solve the optimization problem. Gosiewski and Wierzbicki [1970] formulated an optimization objective function for the EAF taking into account the cost of power and time. The melting stage only was considered in the optimization problem, while the refining and oxidizing stages were not considered. A simplified single state model was used which relates the power input to the bath temperature. The control variables were the secondary transformer tap, which was assumed to remain at its maximum and the arc current. The optimization problem was solved using Pontryagin's maximum principle. Gitgarts and Vershinina [1984] used a dynamic statistical model to obtain the optimal electrical conditions in order to minimize the total costs. The electrical properties were related to the two states of the model representing the progression of the process through a sequence of stages and molten metal temperature. The optimization criterion considered the costs of energy, refractory materials and labour costs. Pontryagin's maximum principle was used to solve the optimization problem. Görtler and Jörgl [2004] developed a control system for a three phase industrial electric arc furnace. The aim was to optimally transfer electrical energy to the scrap without damaging the furnace walls. An electrical subsystem and a thermodynamic system were used to relate the arc radiation to the temperature of the furnace roof and walls. A fuzzy logic controller was used to manipulate the set-point of the impedances of the three phases and transformer tap to control the amount of arc radiation through measuring the temperature of the cooling panels. The optimization in this case focuses on how to select the electrical input parameters for a maximum meltdown power such that the temperatures of the roof and the walls of the furnace remain at the desired level, without causing any damage to the furnace structure.

Jones *et al.* [1999] discussed the use of offgas system analysis to identify and troubleshoot EAF operation. Through the offgas composition, temperature and flow, the operator can get feedback regarding the efficiency of heat transfer in terms of burners, lancing, amount of oil in scrap, etc. Through increasing the efficiency of heat transfer,

the overall operating costs could be decreased.

In contrast to the optimal control applied on subsystems of the EAF, some other approaches considered all the subsystems simultaneously. The disadvantage of the aforementioned approaches, is that optimizing a subsystem could have a negative impact on the rest of the system. Therefore, Matson and Ramirez [1999] developed a model for the EAF process as described previously and investigated an optimal operating strategy of the process. The performance incorporated the idea of faster, better, cheaper tending towards less processing time, maximizing the yield from raw material and maximizing the utilization of chemical energy. This included the CO emitted from the offgas system, the tapped molten metal temperature and the amount of FeO present at the tapping time. A performance criterion was optimized aiming to maximize yield, reduce cost and run sustainably through reducing carbon monoxide emissions. Similarly, MacRosty and Swartz [2007] considered the optimal performance based on an economic objective criterion to maximize profit. The model developed by MacRosty and Swartz [2005] was used and path constraints and end-point constraints were enforced on some of the variables. The trade-off between process inputs and processing time was illustrated and sequential approach was used to solve the optimization problem.

2.1.3 EAF Control Applications

Some applications were developed to control certain variables of interest in the EAF at specific ranges, through manipulating the inputs to the process. Oosthuizen *et al.* [1999] used the model by Bekker *et al.* [1999] and added three more states describing the mass flow of CO, CO_2 and N_2. The authors implemented a model predictive controller (MPC) to control the steel temperature, relative pressure in the furnace and the amount of CO in the offgas system. The manipulated variables were the fan speed,

slip gap width and the rate of addition of direct reduced iron (DRI). A linearized state space model was utilized and setpoints were specified for the steel temperature at the end of the heat, relative furnace pressure and the CO emission. Similarly, Bekker *et al.* [2000] used the model by Bekker *et al.* [1999] and implemented MPC control of the offgas system. The forced draught fan power and the air-entrainment slip-gap width were also the manipulated variables. The control variables were the relative pressure in the furnace, the CO content in the offgas and the offgas temperature. Unlike Oosthuizen *et al.* [1999], DRI was considered as a disturbance rather than a manipulated variable. Oosthuizen *et al.* [2004] extended the work done by Oosthuizen *et al.* [1999] and Bekker *et al.* [2000] by designing a linear MPC for the EAF with an economic objective function. The manipulated variables were the offgas fan power, slip-gap width, oxygen injection rate, DRI feed-rate and the graphite injection rate. The controlled variables were the relative furnace pressure, CO emitted to the atmosphere, offgas temperature, steel mass, steel temperature, percent of carbon in the steel melt and slag foam depth. This was implemented through translating the process economics into weights based on the cost of the feed materials and the economic implications of reaching or not reaching the control objectives. These weights are then included in a quadratic MPC objective function. Pozzi *et al.* [2005] discussed the use of a control system (EFSOP), which uses the measurements of the offgas composition at the fourth hole of the furnace. Through closed loop control, set-points are generated for the burners and oxygen lancing operations which control the combustion process in the freeboard gas volume. Information regarding the decarburization rate and amount of reacted carbon could be deduced based on the measurements of the CO and H_2 in the offgas system.

2.2 Dynamic Optimization

This section will focus on formulating the dynamic optimization problem for a differential-algebraic equation (DAE) system and outlining the key methods used to solve it. DAE systems are considered more challenging than purely algebraic systems due to the presence of differential states that are required to be integrated and the infinite-dimensional search space of the decision variables. The general form for the optimization of a DAE system is shown as (Cervantes and Biegler [2001]),

$$\min_{u(t),t_f} \phi(x(t_f), z(t_f), u(t_f), t_f,) \tag{2.1}$$

subject to :

$$\frac{dx(t)}{dt} = f(x(t), z(t), u(t), t) \tag{2.2}$$

$$0 = h(x(t), z(t), u(t), t) \tag{2.3}$$

$$0 \geq g(x(t), z(t), u(t), t) \tag{2.4}$$

$$x^L \leq x(t) \leq x^U \tag{2.5}$$

$$z^L \leq z(t) \leq z^U \tag{2.6}$$

$$u^L \leq u(t) \leq u^U \tag{2.7}$$

$$x_0 = x(0) \tag{2.8}$$

in which z(t) represents the algebraic variables, x(t) is the vector of differential state variables and u(t) is the set of control input variables. f, h and g represent the differential equation constraints, equality constraints and inequality constraints respectively.

Two key approaches for solving dynamic optimization problems are the sequential approach and simultaneous approach.

The simultaneous method involves discretizing both the control variables and the state variables. It discretizes the DAE system to form an algebraic equation system. This method is often referred to as a full discretization approach. The state variables are discretized through approximating them using a set of polynomials. This reduces the dynamic optimization problem into a finite nonlinear programming (NLP) problem. The optimization in this case is carried in the full space of the discretized variables. This is also referred to as the infeasible path approach (Vassiliadis *et al.* [1994]), because the differential equations are satisfied at the converged solution of the NLP only. The solution of the model and the optimization is carried out simultaneously.

The sequential approach discretizes the control variables only and as a result the ODE still holds. This allows the optimization to be carried out in the decision variables space only (Chachuat [2009]). The sequential method is also referred to as a single shooting method. It uses a set of initial conditions for the states and passes them to an ODE solver, which integrates the state variables. The final state value of each interval is used as initial state value for the next discretized interval, and as a result any error associated with the initial conditions will propagate until the end of the process. The ODE solver sends the time trajectories and the sensitivity information to the optimizer, which determines the optimal design parameters. Some approaches for obtaining the gradient information for the optimization include finite difference perturbations, integration of the adjoint equations and integrating the sensitivity equations (Vassiliadis *et al.* [1994]).

2.3 Sensitivity Analysis and Parameter Estimability

The application of sensitivity analysis techniques aims at understanding the effect of parameters on a system's response.

Local sensitivity analysis was used in parameter estimability applications to determine the optimal subset of parameters to estimate. Franceschini and Macchietto [2008] discussed the use of model based design of experiments techniques for increasing parameter precision. Parameter estimability was discussed, which checks if the parameters could be uniquely identified and a local sensitivity analysis on the response variables was performed. The rank test was used to check the estimability and the ill-conditioning of the estimation problem. On the other hand, parameter distinguishability was discussed which differentiates between rival models. Parameter correlations were investigated and minimized through including the information content of the experiment in the objective function and constraining the correlation coefficients between parameter pairs to a threshold value. A global sensitivity test was discussed, in which the effect on the output from changing one parameter is investigated, while the other parameters are changing as well. This enables discovering the degree of parameter interactions in a model. Two methods that were discussed are the Fourier amplitude sensitivity test (FAST) and Sobols method (Variance based Monte-Carlo method). Huang *et al.* [2010] reduced an Interleukin 6 (IL-6) signal transduction pathway model which consisted of 68 components and 118 parameters to a model containing 13 components and 19 parameters. A local sensitivity analysis was performed to identify the most sensitive parameters and the effective correlation between the parameters on the outputs was identified. The underlying model was represented by,

$$\frac{dx}{dt} = f(x, p, u) \tag{2.9}$$

$$y = h(x, p, u) \tag{2.10}$$

where x represents the state vector, y is the output vector of length n_y and u is the vector of inputs of the system. The sensitivity profile ($\partial y/\partial p^T$) would then be calculated as,

$$\frac{d}{dt}\frac{\partial x}{\partial p^T} = \frac{\partial f}{\partial x^T}\frac{\partial x}{\partial p^T} + \frac{\partial f}{\partial p^T} \tag{2.11}$$

$$\frac{\partial y}{\partial p^T} = \frac{\partial h}{\partial x^T}\frac{\partial x}{\partial p^T} + \frac{\partial h}{\partial p^T} \tag{2.12}$$

The normalized sensitivity vector $s_{i,k}$ of response k to parameter i was then calculated as,

$$s_{i,k} = \frac{p_i^0}{y_k^0} \times \left[\frac{\partial y_k(t_1)}{\partial p_i} ..... \frac{\partial y_k(t_{nt})}{\partial p_i}\right]^T \tag{2.13}$$

where t_1,...,t_{nt} represents the time vector t of length n_t, p_i^0 is the nominal value of the parameter and y_k^0 is the nominal value of the response variable. The norm was used as a single metric representing the impact that the parameter p_i has on the combined outputs.

$$||s_{i,combined}|| = \sqrt{\sum_k \sum_j \left(\frac{p_i^0}{y_k^0} \times \frac{\partial y_k(t_j)}{\partial p_i}\right)^2} \tag{2.14}$$

The identifiability of the model was improved through this reduction technique and was validated against experimental data. McLean *et al.* [2012] identified the optimal subset of parameters for a batch reactor model which gives the best predictions of the experimental data. An orthogonalization algorithm combined with a mean squared error (MSE) criterion was used to rank the parameters from the most estimable to the least estimable using a sensitivity matrix. McAuley *et al.* [2010] also applied same technique on a dynamic chemical reactor to obtain the optimal subset of parameters to be estimated.

McLean and McAuley [2012] discussed identifiability (related to model structure) and estimability (related to experimental data) techniques, in order to obtain better model predictions and parameter estimates. Identifiability techniques included Taylor series expansion, linearization and similarity transformation approaches; however, it was mentioned that applying such methods (except linearization) on large nonlinear systems with more than 15 parameters is very difficult. The drawbacks regarding the linearization method is that no confident conclusion can be made about the nonlinear system, if the linearized system was found to be identifiable. Estimability approaches were favored, such as the use of the rank of the Fischer Information Matrix (FIM) or Monte Carlo simulations. Other methods were introduced in case the parameters were inestimable, in order to choose an estimable subset, while fixing the rest of the parameters to their nominal values. Such methods included the use of scalar measures (such as sensitive mean) of FIM, principal component analysis (PCA) and an orthogonalisation approach. Kravaris *et al.* [2013] discussed the ill-conditioning that arises during parameter estimation due to a large number of parameters in a model. Regularization techniques were discussed, which included ridge regression, principal component analysis and parameter selection approaches. The three methods focused on the idea of adding constraints to reduce the feasible space of the estimation problem. Heuristic and optimization methods for parameter selection were discussed, in order to identify the subset of parameters to estimate. A local sensitivity approach was discussed and the norm of the sensitivity vectors was used as a single metric criterion.

Some of these applications were applied on EAFs to determine the effect of the inputs entering the furnace on the output variables. Wendelstorf and Spitzer [2006] performed a sensitivity analysis on an EAF to identify the effect of inputs on the outputs, in order to determine the model requirements for input measurements. This included the initial temperature of the solid scrap, lower shell temperature and weight precision of second charge. A local sensitivity test was used and the effect on the out-

puts, which included the tapping temperature and melt-down status was calculated. A similar case study conducted by Wendelstorf [2008] assumed no chemical energy addition to the system and a local sensitivity test was performed. The idea was to find the effect of the scrap charging strategies and scrap weight precision on two outputs, which are the tap-to-tap-time (TTT) and energy efficiency. MacRosty and Swartz [2005] performed a sensitivity analysis on the EAF model developed, to identify the most sensitive parameters required to be estimated. Design of experiments (DOEs) was used and a resolution IV fractional factorial design was implemented to investigate the main effects of the parameters on the model outputs. A single metric was chosen to be the integral-square-error (ISE) of the predictions from the mean state predictions to summarize the time-dependent predictions for the entire batch in a single value.

2.4 Parameter Estimation

Most complex models involve a large set of parameters to be able to describe the real process. In the previous section, methods for selecting the optimal subset of parameters to estimate were reviewed. Once, this set of parameters to estimate is determined, the parameter values are obtained in the framework of a dynamic optimization problem. The main idea is to minimize the deviation between the model predicted outputs and the actual plant outputs. Biegler *et al.* [1986] discussed the solution of a parameter estimation problem formulated by the DOW Chemical Company, which consisted of a DAE model that described the kinetics of an isothermal batch reactor. The authors discussed how the objective function should incorporate the error structure of the experimental data in order to achieve a best fit of the data, and emphasized the importance of removing unnecessary parameters to improve the conditioning of the optimization problem. The parameters were estimated through

maximizing the likelihood function. Similarly, Kravaris *et al.* [2013] discussed the stages for formulating and solving a parameter estimation problem for a model described by,

$$\dot{x}(t) = f(x(t), u(t), \theta) \tag{2.15}$$

$$y(t) = g(x(t), u(t), \theta) \tag{2.16}$$

where x represents the state vector, y is the output vector, u is the input vector and θ is the parameter vector. The authors showed that the output y could be obtained through model simulations assuming the availability of the initial state x(0), the input profile u(t) and the parameter vector θ. This results in a parameter-output relationship denoted by $y(t, \theta)$ which is time dependent. The next step would be to formulate the regression model through discretizing the output profiles and incorporating the noise information. Therefore, for set of time points $t_1, t_2, ..., t_m$ the output would be sampled as,

$$h(\theta) = \Big[y_1(t_1, \theta), ..., y_1(t_m, \theta), ..., y_n(t_1, \theta), ..., y_n(t_m, \theta)\Big]^T \tag{2.17}$$

The authors discussed the incorporation of noise for the experimental data as,

$$\tilde{y} = h(\theta) + \epsilon \tag{2.18}$$

where $\tilde{y}$ is the experimental data vector, $h(\theta)$ is the model prediction and ϵ is the noise vector. The last step would then to formulate the optimization problem where the maximum likelihood estimation is reduced to a least squares estimation when the noise is represented by Gaussian noise denoted by $\epsilon \sim$ N(0, σ^2I) with a mean of zero and covariance of σ^2I.

$$\hat{\theta} = \arg\min_{\theta} (\tilde{y} - h(\theta))^T (\tilde{y} - h(\theta)) \tag{2.19}$$

In this case, the parameter estimates are obtained through minimizing the deviation of the model predictions from the measured data. In this work (Chapter 4), the maximum likelihood function is reduced to a weighted least squares problem, and will be used to estimate the parameters from plant data.

2.5 State Estimation

In order to apply advanced control strategies such as model predictive control (MPC), etc., plant state knowledge is always necessary. In complex plants, not all system states are observable or could be directly measured. State estimation techniques use state observers and model-based approaches to infer the states of the system using available measurements observed over time. Some of these state observers include the Kalman filter, Luenberger observer and moving horizon estimator (MHE) (Dochain [2003]; Lima *et al.* [2013]). The Kalman filter (KF) was developed to obtain optimal estimates of the states from the observations, when the uncertainties in the measurement and state equations could be modeled as Gaussian white noise processes. The Kalman filter was developed for linear systems, and in order to apply it for nonlinear systems a modified version of the Kalman filter was developed which is the extended Kalman filter (EKF). The EKF uses local linearization to compute the Jacobians at each time step (Prakash *et al.* [2010]). The state covariance propagation is then performed using Taylor series expansion of the nonlinear state transition operator. This work will focus on applying the EKF on the EAF nonlinear model to infer the actual states of the process using plant measurements obtained along the batch.

The extended Kalman filter application has been widely used in semi-batch reactors. Kozub and MacGregor [1992] implemented an extended Kalman filter on semi-batch emulsion copolymerization of styrene/butadiene rubber (SBR). The authors also in-

troduced the application of a reiterative extended Kalman filter, in which two EKFs are used in parallel. EKF1 is used to provide estimates of unknown initial states using a sequence of measurements and then send these estimates to a second regular EKF2. EKF2 is then restarted from time t=0 using the updated estimates provided. The reiterative EKF showed faster convergence than the regular EKF using poor initial guesses, but one of the drawbacks of this application is the computational load required for the reiteration procedure. Non-stationary disturbances were used to prevent bias in the state estimates and provide an integral action. Clarke-Pringle and MacGregor [1997] discussed the temperature control of a semi-batch reactor. An extended Kalman filter was coupled to a nonlinear controller and outperformed the PID controller with feed-forward compensation.

The previous semi-batch reactors, where an EKF was implemented represented ODE systems. In contrast, Becerra *et al.* [2001] implemented the EKF on a DAE model of index one for a chemical batch reactor consisting of six differential states and four algebraic equations. Time varying linearization was applied which converts the DAE system to a system of ODEs. Becerra explored the implementation of an EKF on a DAE model using a square-root-extended Kalman filter algorithm (Park and Kailath [1995]). The square-root EKF ensures that the covariance matrix remains positive definite through propagating the square root of the covariance matrix. LQ factorization was used to implement the predicting and updating steps for the filter.

In most batch processes, some measurements are obtained more frequently than others. Incorporating such delays in the EKF formulation becomes essential. Prasad *et al.* [2002] implemented a multi-rate extended Kalman filter for a styrene polymerization continuous stirred tank reactor, where the authors used the estimates of the molecular weight moments to infer the polymer properties, such as the number average molecular weight (NAMW) and polydispersity (PD) in the presence of limited measurements. The multi-rate algorithm incorporated the different sample times between

fast and discrete measurements, through using different EKF versions. Depending on the measurements available at each time step, a certain EKF version is implemented. Stochastic disturbances were augmented to the system states and a detailed local linear observability analysis was carried out on the augmented system. Different measurement and disturbance combinations were tested on the observability of the system. The multi-rate estimator was coupled with a nonlinear model predictive control algorithm to predict the future control moves.

Lima *et al.* [2013] discussed using a reduced extended Kalman filter (Schmidt-Kalman filter) that eliminates the weakly observable states from the Kalman gain calculations. In addition, they discussed the use of a linear time varying autocovariance least squares (LTV-ALS) technique to estimate the statistics of the covariance matrices.

A limited number of EKF applications on EAF systems exist. Billings *et al.* [1979] applied the extended Kalman filter on the refining stage of the EAF process, however the model was a very simplified model consisting of 4 states only (concentration of carbon in molten bath, concentration of manganese in molten bath, concentration of iron oxide in slag and temperature of molten bath) which misses a lot of information regarding the real EAF system. The authors did not consider the flux additions, which can result in significant changes in the chemical and thermal behaviour of the process. The measurements that were considered are the molten metal temperature and the carbon concentration in the molten bath. At that time, existing instrumentation technologies for the EAF did not exist. Wang *et al.* [2005] used the extended Kalman filter to determine the arc current parameter in order to obtain the electrical properties of the EAF load. The EAF model used, mainly involves the power system of the furnace.

Chapter 3

Mathematical Model

The intent of this chapter is to show the formulation of the model used in this work. A detailed first principles model based largely on the model developed by MacRosty and Swartz [2005] will be presented. Assumptions and major changes that were performed on the model will be highlighted. Some other model details are provided in Appendix A.

3.1 Model Formulation

The model used for the electric arc furnace (EAF) is a first principles model developed in a gPROMS (general Process Modeling Software) platform. This model was initially developed by MacRosty and Swartz [2005] according to the operation of a particular industrial partner (ArcelorMittal Dofasco, Hamilton, Canada). A new industrial partner collaboration (ArcelorMittal Contrecoeur Ouest, Quebec, Canada) required reconfiguring the model to match their furnace configuration and operating strategy. The EAF model is decomposed into four main zones; the solid scrap zone (SS), slag-metal interaction zone (SM), molten metal zone (MM) and gas zone (GS). In each

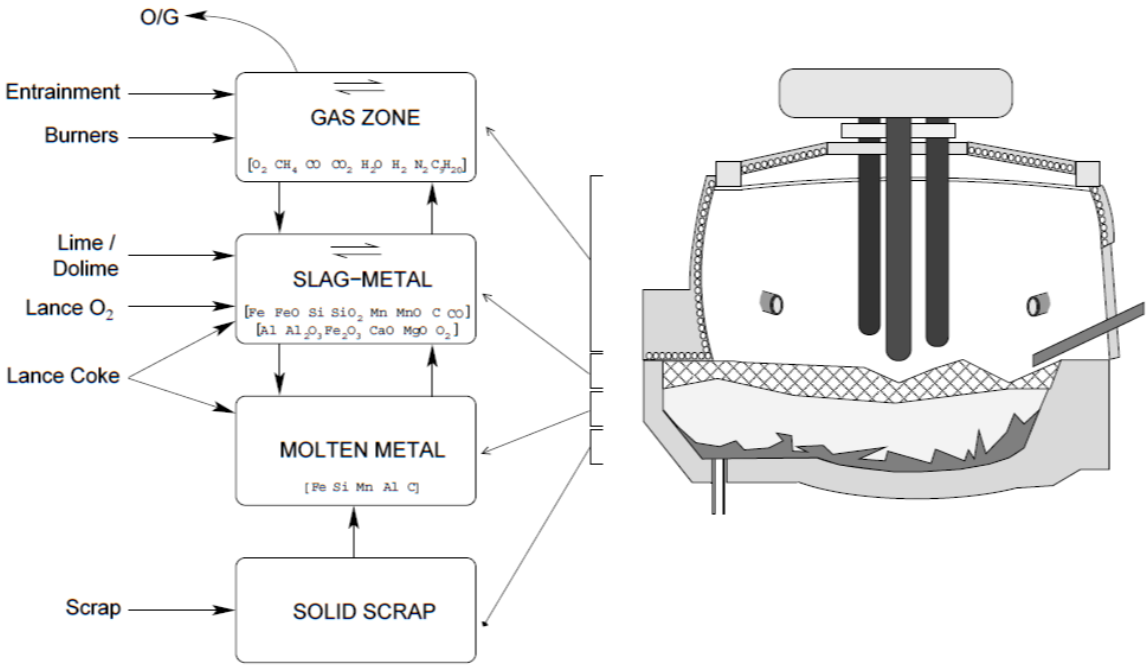

Figure 3.1: Schematic diagram of the EAF model (MacRosty and Swartz [2005])

zone, material balances and heat transfer relationships are considered. Figure 3.1 shows a schematic diagram of the process and how materials are exchanged between the zones. This section will discuss the model that was developed and highlight the changes that were applied during model reconfiguration. The variables from different zones will be differentiated through the use of the subscripts ss, sm, mm, gs for the solid scrap zone, slag-metal interaction zone, molten metal zone and the gas zone respectively.

3.1.1 Solid Zone

The solid scrap zone represents the scrap that is being charged in the furnace. The solid scrap is modeled as a lump surface, which is mainly composed of iron (Fe). The other major components are carbon, silicon, manganese and aluminum. The scrap also usually contains some oil impurities that are modeled in the furnace as a

hydrocarbon component (C_9H_{20}).

Material Balance

Solid scrap absorbs energy and melts to form molten metal. Therefore, the main material exchange is between the solid scrap zone and the molten metal zone. As the amount of solid scrap melted increases, the amount of molten metal increases accordingly. Usually two charges are loaded in a single heat, therefore this scrap charge addition is incorporated while formulating the rate of mass change for the scrap. The rate of mass change of solid scrap is represented by the equations below,

$$\frac{d}{dt}(m_{ss}) = \dot{m}_{in} - \dot{m}_{melt} \tag{3.1}$$

$$\dot{m}_{melt}(\Delta H_{fusion} + C_p(T_{melt} - T_{ss}))k_{dm} = Q_{ss}^{net}\frac{T_{ss}}{T_{melt}} \tag{3.2}$$

$\dot{m}_{in}$ and $\dot{m}_{melt}$ are the rate of addition of scrap and rate of scrap melted respectively. Equation (3.2) represents the rate of melting of the scrap which is determined by dividing the rate of energy available to melt the solid scrap by the energy per unit mass required to melt the scrap at its current temperature (MacRosty and Swartz [2005]). ΔH_{fusion} is the latent heat of fusion of iron, the term $C_p(T_{melt}-T_{ss})$ represents the sensible heat required to raise the solid scrap temperature (T_{ss}) to the melting temperature (T_{melt}), ($\frac{T_{ss}}{T_{melt}}$) represents the fraction of energy that contributes to scrap melting and k_{dm} is an estimated parameter to account for variations in the bulk density and composition in the scrap.

Energy Balance

Solid scrap absorbs net energy (Q_{ss}^{net}) until it reaches its melting point, at which point it then melts to form molten metal. This is shown in the equation below,

$$Q_{ss}^{net} = Q_{power-ss} + Q_{mm-ss} + Q_{gs-ss} - Q_{volatile} - Q_{charge} - q_3^{rad} \tag{3.3}$$

The solid scrap absorbs energy mainly from conductive, convective and radiative heat transfer. $Q_{power-ss}$ is the heat transferred from the arc to the solid scrap and q_3^{rad} is the radiative energy released from the solid scrap in which a negative sign convention implies the gain of radiative energy. The solid scrap zone mainly exchanges heat with the molten metal zone and the gas zone, as well as absorbing energy from the arc electrodes. The heat transfer from the molten metal (Q_{mm-ss}) and gas zones (Q_{gs-ss}) to the solid scrap zone is given by the expressions below.

$$Q_{mm-ss} = \frac{m_{ss}}{(m_{ss}+\gamma)} m_{mm} k_{t1} (T_{mm} - T_{ss}) \tag{3.4}$$

$$Q_{gs-ss} = m_{ss} h_{gs-ss} (T_{gs} - T_{ss}) \tag{3.5}$$

$$h_{gs-ss} = k_{t3} (F_{CH4}^{in} + F_{O2}^{in}) \tag{3.6}$$

in which m_{mm} is the mass of molten metal, m_{ss} is the mass of solid scrap, T_{mm} is the molten metal temperature and T_{gs} is the gas temperature. Equation (3.4) is slightly modified from MacRosty and Swartz [2005], through adding the fraction $m_{ss}/(m_{ss}+\gamma)$ where γ has a magnitude of 5×10^3. This is to ensure that the rate of heat transfer from the molten metal to the solid scrap diminishes as more scrap melts. Both Q_{gs-ss} and Q_{mm-ss} are proportional to the temperature gradient across the zones, as well

as, to the heat transfer coefficients k_{t1} and k_{t3}, which are estimated from plant data. During the beginning of the heat, the heat transfer between the gas zone and the solid zone is very high, and therefore Q_{gs-ss} is assumed to be proportional to the flow rate of burner's materials. This is shown in equation (3.6), where h_{gs-ss} is calculated. Equation (3.6) is slightly simplified from MacRosty and Swartz [2005] in which the bulk density is accounted for in the estimated parameter k_{t3}.

The solid scrap absorbs energy from the arc in terms of conductive heat and radiative heat transfer. According to literature (Guo and Irons [2003]), 18% of the arc power is delivered directly to the steel. A portion of the radiative heat transferred to the walls and roof of the furnace is retained through slag foaming using an efficiency factor (E_f). This will be discussed in more detail later in the following sections. The energy from the arc is partitioned between the solid scrap and the molten metal according to their relative masses as shown in the following equation,

$$Q_{power-ss} = \frac{m_{ss}}{m_{ss} + m_{mm}}(E_f(q_1^{rad} + q_2^{rad}) + 0.18 P_{arc} k_p) \tag{3.7}$$

where k_p is an estimated parameter and P_{arc} is the active power. q_1^{rad} and q_2^{rad} represent the amount of energy radiated to the roof and the walls of the furnace respectively, and this will be discussed later in Section 3.4.

Since the scrap contains a small amount of organic volatile material, it would then lose some energy from the vaporization of this hydrocarbon component ($Q_{volatile}$), in addition to some energy that is lost from the addition of the second charge at room temperature (Q_{charge}) as shown below.

$$Q_{charge} = k_{cool} \frac{m_{charge}}{M_w} C_p (T_{ss} - 298K) \tag{3.8}$$

$$Q_{volatile} = \Delta H_{vap} F_{oil}^{add} \tag{3.9}$$

k_{cool} is an estimated parameter, m_{charge} is the mass of the second scrap charge, M_w is the molecular weight of Fe in this case, ΔH_{vap} is the latent heat of vaporization for C_9H_{20} and F_{oil}^{add} is the rate of volatile component addition.

The solid scrap temperature is calculated as,

$$\frac{d}{dt}(T_{ss})\ k_{dt} = Q_{ss}^{net}\ (1 - \frac{T_{ss}}{T_{melt}}) \tag{3.10}$$

where $\frac{T_{ss}}{T_{melt}}$ represents the fraction of energy available for melting , while the remaining is responsible for sensible heating. This ensures that the scrap temperature will never exceed the melting temperature (Bekker *et al.* [1999]).

3.1.2 Molten Metal Zone

The molten metal zone contains mainly the metals in their liquid state after the scrap has melted. Material enters the molten metal zone mainly from the solid scrap zone as scrap melts and materials exit towards the slag-metal interaction zone. It was assumed that no reactions occur within the molten metal zone due to the absence of oxygen (MacRosty and Swartz [2005]). The molten metal zone contains mainly the components iron (Fe), manganese (Mn), aluminum (Al), carbon (C) and silicon (Si). Materials are transferred to the slag-metal zone through diffusion. The model takes into account the lancing of carbon and tracks how it is transfered to the slag-metal zone, where it reacts with O_2 or FeO to form CO through the decarburization process.

Material Balance

The net molar flow rate of materials into the molten metal zone is represented by the equation below,

$$F_{mm,i}^{net} = (1 - \theta_{L,i})F_{lance,i} + F_{sm-mm,i} + F_{ss-mm,i} \tag{3.11}$$

in which F_{mm}^{net} is the net molar flow of materials into the molten metal zone, θ_L is the lancing fraction, F_{lance} is the flow rate of lanced material which are carbon and oxygen; it was assumed that all the oxygen lancing goes into the slag-metal interaction zone. $F_{sm-mm,i}$ and $F_{ss-mm,i}$ respectively represent the flow of component i from the slag-metal zone and solid scrap zone to the molten metal zone.

The concentration gradient across the EAF zones is the main driving force for the transfer of materials from one zone to the other. For the mass transfer between the slag-metal interaction zone and the molten metal zone, the mass transfer coefficient is expressed as a product of two parameters. The first parameter represents the relative mass transfer coefficient with respect to the other components and this could be obtained from literature sources (Mills and Keene [1987]), and the second parameter is estimated from the plant data and is considered the base mass transfer coefficient that has a constant value for all the components. This is represented by the equation below,

$$F_{mm-sm,i} = \beta_i k_m (y_{mm,i} - y_{sm,i}) \tag{3.12}$$

in which $F_{mm-sm,i}$ is the molar flow rate of material i from the molten metal to the slag-metal, $y_{mm,i}$ and $y_{sm,i}$ are the molar composition of the component i in the molten metal and slag-metal zones respectively. k_m and β_i are the base mass transfer coefficient and relative mass transfer coefficient respectively.

The rate of decarburization is limited through the presence of oxygen either in the form of O_2 or FeO and the rate of mass transport to the reaction interface (MacRosty and Swartz [2005]). The model takes into account the decarburization rate through modeling the transport of carbon from the molten metal to the slag-metal interaction zone. The availability of oxygen is controlled through the lancing rate of oxygen directly into the slag-metal phase or through the presence of FeO. To account for the additional mixing effect of lancing in the carbon and oxygen transport from the molten metal to the slag metal, an additional variable is added (k_{ml}) which is directly proportional to the flow rate of oxygen lancing and the bubble diameter (γ_d). γ_d is an estimated parameter. Those relationships are shown below,

$$F_{mm-sm} = \beta_C k_m (y_{mm,C} - y_{sm,C}) + k_{ml}(y_{mm,C} - y_C^*) \tag{3.13}$$

$$k_{ml} = \gamma_d F_{O2} \tag{3.14}$$

in which y_C^* is the equilibrium concentration of carbon in steel and F_{O2} is the flow rate of oxygen lanced. y_c^* is considered as an estimated parameter and the limits were set based on some literature values (Fruehan [1998]).

Energy Balance

The molten metal exchanges energy with the solid scrap zone as described in Section 3.1.1, in addition to the slag metal and the arc. Therefore, the main heat forms are the conductive, convective and radiative heat transfer. The heat exchange between the molten metal and the gas zone is assumed to be negligible (MacRosty and Swartz [2005]). The net heat flow into the molten metal is represented by,

$$Q_{mm}^{net} = Q_{power-mm} - Q_{mm-sm} - Q_{cool} - Q_{mm-ss} - q_4^{rad} \tag{3.15}$$

where $Q_{power-mm}$ represents the heat transferred from the arc to the molten metal which is partitioned relative to the amount of molten metal and solid scrap present in the furnace, as shown below.

$$Q_{power-mm} = \frac{m_{mm}}{m_{ss} + m_{mm}}(E_f(q_1^{rad} + q_2^{rad}) + 0.18 P_{arc} k_p) \tag{3.16}$$

Q_{mm-ss} represents the heat transferred from the molten metal to the solid scrap and is given by the expression below, where k_{t1} is an estimated parameter.

$$Q_{mm-ss} = k_{t1} m_{mm}(T_{mm} - T_{ss}) \tag{3.17}$$

Q_{mm-sm} is the heat transferred from the molten metal to the slag-metal interaction zone and the relationship is represented below,

$$Q_{mm-sm} = k_{t2} m_{sm}(T_{mm} - T_{sm}) \tag{3.18}$$

Equation (3.18) is slightly modified from MacRosty and Swartz [2005], in which the mass of slag (m_{sm}) is incorporated in the heat transfer equation. In this case the amount of heat transfer between the molten metal and slag-metal interaction zone would be proportional to amount of slag present, and therefore Q_{mm-sm} would diminish as the slag mass approaches zero.

q_4^{rad} is the radiative heat transfer, in which a negative sign convention indicates that energy has been received and vice versa. Q_{cool} (equation A.2) represents the heat absorbed by the cooling water, and k_{t1} and k_{t2} are estimated parameters which represent the heat transfer coefficients.

3.1.3 Gas Zone

The gas zone in the EAF model considers the freeboard volume in the furnace. This is the volume that exists above the scrap metal as it melts. Therefore, the freeboard gas volume increases as melting proceeds. Eight components are being considered in this zone which are carbon monoxide (CO), carbon dioxide (CO_2), oxygen (O_2), hydrogen (H_2), nitrogen (N_2), methane (CH_4), water vapour (H_2O) and the volatile component (C_9H_{20}). This volatile component represents the average composition of organic materials present in the scrap being charged and which vaporizes during the initial operation stage of the furnace. Materials from the burners are added to this zone in terms of (CH_4) and (O_2) to preheat the scrap, before switching the power to the high mode. Another source of materials added to the gas zone are the ingressed air which are mainly (O_2), (N_2) and (H_2O), beside water from the cooling panels. Chemical equilibrium was assumed, which is reasonable considering the high temperature occurring in this zone.

Material Balance

The chemical equilibrium is calculated through minimizing the Gibbs free energy which is formulated as an optimization problem. In order to perform this, an atom tracking balance must be computed as shown below,

$$\frac{d}{dt}(b_{k,z}) = F_{k,z}^{in} - F_{k,z}^{out} \tag{3.19}$$

in which b_k is the molar amount of element k in zone z, $F_{k,z}^{in}$ and $F_{k,z}^{out}$ are the molar flow of element k in and from zone z respectively.

Calculating the chemical equilibrium through the minimization of the Gibbs free energy results in a system of equations that corresponds to the first order necessary

conditions of a constrained minimization of the Gibbs free energy, as shown in the following equations.

$$\sum_i n_i a_{i,k} = b_k \tag{3.20}$$

$$\Delta G^o_{f,i} + RT\ ln\hat{a}_i + \sum_k \lambda_k a_{i,k} = 0 \tag{3.21}$$

The advantage of this method, is that the stoichiometric relationships and equilibrium constants do not need to be considered (Wai and Hutchison [1989]). n_i represents the number of moles of component i at equilibrium in the gas zone, $a_{i,k}$ is the number of atoms of element k in component i in the gas zone and b_k is the elemental molar amount of element k. $\Delta G^o_{f,i}$ is the Gibbs free energy of formation, $\hat{a}_i$ is the activity coefficient of component i and λ_k are the Lagrange multipliers. The activity coefficient is a function of temperature, composition and pressure. An ideal gas is assumed in this case and an activity coefficient of 1 is used. The elemental molar flow could then be related to the compound molar flow rate as shown below.

$$F_{k,z} = \sum_i a_{i,k} F_{i,z} \tag{3.22}$$

The net molar flow rate (F^{net}_{gs}) in the gas zone can be represented as,

$$F^{net}_{gs,i} = F_{burner,i} + F_{sm-gs,i} + F_{volatile,i} - F_{offgas,i} + F_{Pconst,i} \tag{3.23}$$

in which $F_{burner,i}$ represents the flow of component i from the burners into the gas zone, $F_{sm-gs,i}$ represents the flow of component i from the slag-metal zone to the gas zone, $F_{volatile}$ is the flow of volatile material into the gas zone, $F_{offgas,i}$ is the flow of material out of the gas zone and into the offgas system and finally $F_{Pconst,i}$ represents

the materials being ingressed into or expelled from the furnace at constant pressure which will be discussed later.

The materials that flow from the slag-metal zone to the gas zone are CO and O_2, that evolve from the slag as a result of oxygen lancing. Also, the flow of oxygen is limited by the concentration gradient of oxygen across both zones as represented by the equation below.

$$F_{O_2,sm-gs} = k_{PO2}(y_{O_2,sm} - y_{O_2,gs}) \tag{3.24}$$

k_{PO2} is the mass transfer coefficient that is estimated in the model, $y_{O_2,sm}$ is the concentration of oxygen in the slag-metal zone and $y_{O_2,gs}$ is the concentration of oxygen in the gas zone. The offgas (F_{offgas}) is assumed to have the same composition as that in the freeboard gas volume. Also, the gas volume is assumed to be at constant pressure and this is the driving force behind the air being sucked in or pushed out of the furnace. The constant pressure is assumed due to the large openings in the furnace and the constant offgas flow rate that was assumed (MacRosty and Swartz [2005]). Therefore, $F_{Pconst,i}$ could be positive or negative depending on the direction of flow of materials in or out of the furnace. The air being sucked into the gas zone is assumed to have the same composition as the ambient air, while the gas that is being pushed away would have the composition of the gas zone. Equation (3.25) below tracks the materials that are being sucked or pushed away from the furnace.

$$F_{Pconst,i} = x_{freeboard-gas,i} \min(0, F_{net}) + x_{air,i} \max(0, F_{net}) \tag{3.25}$$

F_{net} is computed based on the constant pressure assumed in the freeboard gas volume and the constant offgas flow rate (calculations are provided in Appendix A.2). The min and max functions in equation (3.25) were approximated as shown in Appendix

A.2 to avoid discontinuities in the model and the calculations for the air ingressed and pushed away are also illustrated. The volatile material added to the gas zone was modeled assuming its addition at a constant rate for a short period of time in order to approximate the dynamics of the vaporization of the volatiles as shown below.

$$\frac{dN_{oilgas}}{dt} = (X_{oil}F_{oil}^{in}) - (k_{oil}\frac{T_{ss}}{T_{melt}}N_{oilgas}) \tag{3.26}$$

X_{Oil} represents the fraction of oil in scrap and k_{oil} is the rate of combustion of the volatile component, and both are estimated parameters. $\frac{T_{ss}}{T_{melt}}$ shows the increasing rate of hydrocarbon combustion with increasing solid scrap temperature (Logar *et al.* [2012b]).

Energy Balance

The gas zone exchanges heat with the solid scrap beside the roof and the walls of the furnace through convection. The net heat transfer to the gas zone is represented by the following equation,

$$Q_{gs}^{net} = -Q_{gs-ss} - Q_{gs-wall} - Q_{gs-roof} \tag{3.27}$$

in which Q_{gs-ss} is the heat transfer from the gas zone to the solid scrap, $Q_{gs-wall}$ is the heat transfer from the gas zone to the walls of the furnace and $Q_{gs-roof}$ is the heat transfer from the gas zone to the roof of the furnace.

The heat transfer between the gas zone and the solid scrap is proportional to the temperature gradient across both zones and is calculated the same way shown in equations (3.5) and (3.6). This heat exchange is very significant during the preheat stage, which is the few minutes after the scrap has been charged into the furnace.

The heat transfer relationships between the gas zone and the walls and the roof of the furnace are shown below.

$$Q_{gs-wall} = h_{gs}\frac{A_{wall}}{A_{roof} + A_{wall}}(T_{gs} - T_{wall}) \tag{3.28}$$

$$Q_{gs-roof} = h_{gs}\frac{A_{roof}}{A_{roof} + A_{wall}}(T_{gs} - T_{roof}) \tag{3.29}$$

in which h_{gs} is the heat transfer coefficient, and the heat transfer is proportional to the relative area of the roof and the walls (Logar *et al.* [2012b]), in addition to the temperature gradient across both zones. T_{wall} is the wall temperature and T_{roof} is the roof temperature. This has been slightly modified from MacRosty and Swartz [2005] which considered the area of the wall and the roof independently and not the relative area. This modification avoided some numerical issues during the estimation of the parameter h_{gs}.

The overall energy hold up in the gas zone (E_{gs}) is calculated as shown below,

$$\frac{d}{dt}(E_{gs}) = Q_{gs}^{net} + \sum_{i=1}^{n} F_i H_i \mid_{in} - \sum_{i=1}^{n} F_i H_i \mid_{out} \tag{3.30}$$

in which F_i represents the flow rate of component i and H_i is the corresponding enthalpy.

3.1.4 Roof and Walls

The roof and the walls of the furnace receive energy from radiation, and convective heat transfer from the gas phase. The presence of cooling panels is therefore necessary to ensure that the temperatures of the walls and roof of the furnace do not exceed a

certain limit, which was set to 800 K. The temperature profile calculations for both the roof and the walls are represented by,

$$\frac{d}{dt}T_{wall} = \frac{Q_{gs-wall} - Q_{wall-water} - q_2^{rad}}{m_{wall}C_{p,wall}} \tag{3.31}$$

$$\frac{d}{dt}T_{roof} = \frac{Q_{gs-roof} - Q_{roof-water} - q_1^{rad}}{m_{roof}C_{p,roof}} \tag{3.32}$$

$C_{p,roof}$ and $C_{p,wall}$ are the heat capacities of the furnace roof and walls respectively. Same negative sign convention for q_1^{rad} and q_2^{rad} is used as that for the solid scrap and molten metal discussed previously.

$Q_{wall-water}$ and $Q_{roof-water}$ represent the heat transferred to the cooling water from the walls and the roof of the furnace respectively.

$$Q_{wall-water} = \dot{m}_{H_2O,wall}C_{p,H_2O}(T_{cw,wall}^{out} - T_{cw,wall}^{in}) \tag{3.33}$$

$$Q_{roof-water} = \dot{m}_{H_2O,roof}C_{p,H_2O}(T_{cw,roof}^{out} - T_{cw,roof}^{in}) \tag{3.34}$$

$\dot{m}_{H_2O,roof}$ and $\dot{m}_{H_2O,wall}$ represent the mass flow rate of water to the roof and walls of the furnace respectively. C_{p,H_2O} represents the heat capacity of water. $T_{cw,roof}^{out}$ and $T_{cw,wall}^{out}$ are the outlet cooling water temperatures for the roof and walls of the furnace respectively. Finally, $T_{cw,roof}^{in}$ and $T_{cw,wall}^{in}$ are the inlet cooling water temperatures for the roof and walls of the furnace respectively.

3.2 Slag-Metal Interaction Zone

The slag-metal interaction zone contains all the slag material in addition to a portion of the molten-metal zone which is in contact with the slag-metal zone. The compo-

nents considered in this zone are Fe, FeO, Fe_2O_3, Mn, MnO, Al, Al_2O_3, Mg, MgO, Si, SiO_2, C, CO, CaO, O_2 and N_2. The slag-metal zone mainly constitutes all the oxides as a result of the reactions of the metallic elements with oxygen that is lanced in the furnace. The slag interacts mainly with the molten metal zone and the gas zone.

3.2.1 Material Balance

The net molar flow into the slag-metal zone is given by,

$$F_{sm,i}^{net} = \theta_{L,i} F_{lance,i} + F_{flux,i} + F_{mm-sm,i} + F_{gs-sm,i} \tag{3.35}$$

in which θ_L is the lancing carbon fraction, which is an estimated parameter for lanced carbon, but for the oxygen a value of 1 has been assigned assuming that all the oxygen lanced goes into the slag-metal phase as discussed before. $F_{lance,i}$ is the flow rate of lanced component i, $F_{flux,i}$ represents the addition of flux materials directly through the roof of the furnace such as lime, dolomite and carbon. $F_{mm-sm,i}$ and $F_{gs-sm,i}$ are the molar flow of materials into the slag-metal phase from the molten metal and the gas zones respectively. All the materials flow between the slag-metal zone and the other zones are controlled by the concentration gradient of the components between these zones.

All the oxidation reactions are controlled by the abundance of oxygen in the slag-metal phase. The reactions preference for the metallic elements with oxygen is determined by the reduction potential of the components. Considering the modeling of the flux additions, there are three main additions which are carbon, lime and dolomite charges. When carbon is added through the roof in a bulk form, it initially floats on the top of the slag-metal layer and starts to dissolve in a continuous manner and this can be explained by the equation below,

$$\frac{d}{dt}(m_{C,float}) = F^{in}_{carbon}(1 - X_C) - k_{dc}m_{C,float} \tag{3.36}$$

in which the rate of carbon entering the slag-metal phase is proportional to the amount of carbon floating on the slag-metal. $m_{C,float}$ is the amount of carbon floating on top of the slag-metal layer, F^{in}_{carbon} is the rate of carbon charged into the furnace and X_C is the fraction of impurities in the carbon charge which is assumed to be 15% (metallurgical coke). k_{dc} is an estimated parameter representing the dissolution constant which depends on the type, quality and method of the carbon addition (MacRosty and Swartz [2005]).

The same applies for lime ($m_{CaO,float}$) and dolomite ($m_{dol,float}$).

$$\frac{d}{dt}(m_{CaO,float}) = F^{in}_{CaO}(X_{CaO}) - k_{cao}m_{CaO,float} \tag{3.37}$$

$$\frac{d}{dt}(m_{dol,float}) = F^{in}_{dol}(X_{dol}) - k_{dol}m_{dol,float} \tag{3.38}$$

The dissolution constants for lime (k_{CaO}) and dolomite (k_{dol}) were assumed to be the same magnitude. X_{CaO} and X_{dol} are the purity of lime and dolomite respectively. F^{in}_{Cao} and F^{in}_{dol} are the flow rate of lime and dolomite through the roof of the furnace.

3.2.2 Slag foaming

Slag foaming results from the evolution of CO from the molten metal and is one of the most important factors that steel makers consider during the operation of the furnace. The slag foam that is produced covers the arc of the electrodes and prevents the loss of radiative energy to the walls and the roof, and therefore, enhances energy efficiency. The composition of the slag mainly determines its stability through its

viscosity, density and surface tension. Jiang and Fruehan [1991] derived the foaming index (Σ) that relates the foam height (H_f) to the superficial velocity (V_g^s) and the physical properties of the slag.

$$\Sigma = \frac{115\mu}{\sqrt{\rho\sigma}} = \frac{H_f}{V_g^s} \tag{3.39}$$

The density (ρ) is estimated using the partial molar volumes from data obtained from Mills and Keene [1987], while the viscosity (ρ) is estimated using a model given in Urbain [1987]. The slag surface tension (σ) is estimated using an empirical model obtained from Morales *et al.* [1997]. The superficial gas velocity is calculated using the evolution of CO from the molten metal and using the geometry of the furnace. It should be noted that in most models developed in literature, the slag depth is usually assumed to be sufficient for foaming to occur. If the slag depth is not considered, this would result in large unrealistic foam heights during the initial period of the heat, even if the slag volume is small and not sufficient (MacRosty and Swartz [2005]). Since this model considers the foam height at every time step during the batch, incorporating the slag volume and its effect on the foam height becomes necessary. The equations below explain how the slag depth is related to the foam height through a proportionality coefficient, in which a critical height for the slag depth was set to 20 cm (MacRosty and Swartz [2005]).

$$H_f = \phi(\Sigma V_g^s) \tag{3.40}$$

$$\phi = \frac{1}{2}\tanh(\alpha(h_s) + \beta) + \frac{1}{2} \tag{3.41}$$

If the slag depth (h_s) is equal to or greater than 20 cm, then the coefficient (ϕ) becomes equal to 1. This means that equation (3.40) would be the same as equation (3.39).

On the other hand, if the slag depth is smaller than 20 cm, then the proportionality coefficient would be calculated using equation (3.41), the (α) and (β) are adjustable tuning parameters. The proportionality coefficient approaches zero as the slag depth approaches zero. In this case, the values for α and β were set to 12.95 and -1.289 respectively.

3.2.3 Energy Balance

The slag-metal zone mainly exchanges energy with the molten metal. There is a negligible heat interaction between the slag-metal zone and both the solid zone and the gas zones, and therefore these effects were not considered. Modeling the heat transferred from the arc directly to the slag is very complicated, since this would depend on the volume of the slag and the force of the strike action of the arc which will tend to displace the slag and expose the molten metal below (MacRosty and Swartz [2005]). Therefore, it was assumed that this amount of energy is transferred to the molten metal, and the slag would then indirectly receive it through the heat exchange between the slag-metal zone and the molten metal zone. The net heat transferred to the slag-metal zone is represented by,

$$Q_{sm}^{net} = k_{t2} m_{sm} (T_{mm} - T_{sm}) \tag{3.42}$$

in which k_{t2} is the heat transfer coefficient that is estimated from industrial data, T_{mm} is the molten metal temperature and T_{sm} is the slag-metal temperature.

The energy hold up for the slag-metal zone is calculated using equation (3.43), which has similar notation as that described before in equation (3.30).

$$\frac{d}{dt}(E_{sm}) = Q_{sm}^{net} + \sum_{i=1}^{n} F_i H_i \mid_{in} - \sum_{i=1}^{n} F_i H_i \mid_{out} \tag{3.43}$$

3.3 JetBox Modeling

The plant uses three jetboxes for the injection system. Figure 3.2 shows the components of a jetbox. To identify the partition of the oxygen that enters the gas phase and the slag-metal phase, a switch function was used for each jetbox. When the oxygen is in a subsonic mode, all the oxygen remains in the gas phase and when it turns into supersonic mode, the oxygen penetrates through the slag-metal layer (Lainchbury [2003]). Three switch functions ($O_2^{switchi}$) are developed using a hyperbolic tangent function.

$$O_2^{switch1} = \alpha_3 \tanh(\beta_3 F_{JetBox1}^{in} - \theta_3) + \alpha_3 \tag{3.44}$$

$$O_2^{switch2} = \alpha_4 \tanh(\beta_3 F_{JetBox2}^{in} - \theta_4) + \alpha_4 \tag{3.45}$$

$$O_2^{switch3} = \alpha_5 \tanh(\beta_3 F_{JetBox3}^{in} - \theta_5) + \alpha_5 \tag{3.46}$$

The mode of the jetboxes is therefore modeled as a function of the velocity of the oxygen being injected. As the flow rate of oxygen from the jetboxes ($F_{jetbox_i}^{in}$) increases, the oxygen lancing tends towards a supersonic mode. Here, α_3, α_4, α_5, β_3, β_4, β_5, θ_3, θ_4 and θ_5 are tuning parameters that are estimated using industrial data. It was assumed that α_3=α_4=α_5, β_3=β_4=β_5 and θ_3=θ_4=θ_5. The amount of oxygen that enters the gas and slag zones is then calculated as,

$$JetGas_i = (1 - O_2^{switchi}) F_{JetBox_i}^{in} Bias_{O_2} GS^*, \quad for\ i = 1, ..3. \tag{3.47}$$

$$JetSlag_i = O_2^{switchi} F_{JetBox_i}^{in} Bias_{O_2} SM^*, \quad for\ i = 1, ..3. \tag{3.48}$$

$Bias_{O_2}GS^*$ and $Bias_{O_2}SM^*$ are estimated parameters constrained to be less than or equal to 1 to account for O_2 losses.

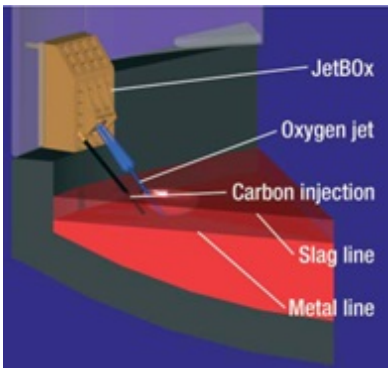

Figure 3.2: JetBox Diagram (Brhel [2002])

3.4 Radiation Model

One of the most important heat transfer mechanisms that occur in the EAF is the radiative heat transfer. The radiative heat transfer would depend on the surface geometry, emissivity and surface area. One of the most challenging dynamics while modeling the radiation part is the melting geometry of the scrap. Due to the high temperature nature in the EAF, identifying the exact geometry for the scrap melting is practically difficult. An approach proposed by MacRosty and Swartz [2005] considered an initial cone-frustum shaped void melted into the scrap by the electrodes, which increases in volume as more scrap is melted. This approach was modified and it was shown that the overall effect on the corresponding EAF trajectories were close.

The reader is referred to MacRosty and Swartz [2005] for the details of the cone-frustum geometry calculations. In the present model, the solid scrap is assumed as a flat surface as shown in Figure 3.3 that decreases in volume, as more scrap melts. The roof was assumed as a disk surface. The solid scrap and molten metal bath have been

assumed as coaxial disk like surfaces, while the wall of the furnace as a right circular cylinder. The arc surface was assumed to be cylindrical. These assumptions made the system much simpler than considering the melting geometry of the scrap as a cone-frustum. Initially the roof of the furnace is shielded from radiation by the initial scrap charge present. As the scrap melts, the furnace's roof and walls get successively exposed to radiation. While the scrap melts down, the arc, roof and the wall do not perceive the molten metal until a certain amount of time, where the amount of scrap present becomes relatively small. Therefore a switch function ($Switch^{rad}$) was added to determine when the molten bath perceives the wall and the roof, in order to calculate the view factors involved. h_{scrap} in the equation below represents the height of the scrap in the furnace.

$$Switch^{rad} = \frac{1}{2}\left[\tanh(80(h_{scrap} - \tfrac{1}{2})) + 1\right] \tag{3.49}$$

As the scrap melts down, a void volume is formed where offgases are present. The volume of the EAF surfaces will change over time as scrap melting proceeds. Through the bulk density and the mass of the solid scrap present over time, the dynamic change in the scrap volume is calculated. The last surface that has been considered in this model is the arc surface, which represents the electrodes that transfer radiative heat to all the other four surfaces. The area of the arc surface has been assumed to be 1 m^2 (MacRosty and Swartz [2005]).

View factors (F_{ij}) show the fraction of energy that is transferred between different surfaces to one another. In the model, the four surfaces have been considered as gray bodies, which means that not all of the energy that is transferred to one surface is totally absorbed, but a part of this energy is reflected. Conversely, the arc surface is considered as a black body and this implies that it is perfectly transparent in receiving energy. This means that it allows any energy to pass through without absorbing any

portion of it. As a result, it was assumed that no energy is transferred from any of the surfaces to the arc surface. The amount of radiative heat transferred from each surface in the system is calculated as shown below.

$$q_i^{rad} = \frac{E_{bi} - J_i}{(1-\epsilon_i)/\epsilon_i A_i} \tag{3.50}$$

$$E_{bi} = \sigma T_i^4 \tag{3.51}$$

$$q_i^{rad} = \sum_{j=1}^{N} A_i F_{ij}(J_i - J_j) \tag{3.52}$$

The term J represents radiosity, which is the total radiation leaving a surface per unit area per unit time and ϵ is the emissive power of each surface. E_b is the black body emissive power which is calculated from the Boltzman law as shown in equation (3.51), where $\sigma = 6.676 \times 10^{-8} \frac{\mathrm{W}}{\mathrm{m^2.K^4}}$, A_i is the surface area of surface i and T_i is the temperature of surface i.

The view factor calculations for gray body structures are shown in Siegel and Howell [2001]. These calculations consider the geometry of each surface. View factors have some properties that have been used in this model. First property is the enclosure constraint, described as,

$$\sum_{i=1}^{N} F_{i,j} = 1 \tag{3.53}$$

The other property is the reciprocity relationship as shown below.

$$A_i F_{ij} = A_j F_{ji} \tag{3.54}$$

After the view factors for each surface have been calculated. The total or net energy from each surface is calculated. A negative sign would mean that energy is being gained by the surface rather than being lost. According to Guo and Irons [2003], it

was assumed that 18% of the energy from the arc is directly transferred to the steel, 2% is transferred to the electrode and finally 80% is being delivered through radiative heat transfer.

$$q_5^{rad} = 0.8 Q_{arc} \tag{3.55}$$

in which q_5^{rad} is the net radiative heat transfer delivered by the arc and Q_{arc} is the total amount of heat delivered by the arc which is proportional to a power factor and the active power as shown below.

$$Q_{arc} = k_p P_{arc} \tag{3.56}$$

The portion of heat transferred from the arc to each surface is approximated by,

$$Q_{5-i}^{arc} = F(5,i)\ q_5^{rad} \tag{3.57}$$

where $F(5,i)$ is the fraction of energy being transferred from the arc to surface i. The detailed view factor calculations are shown in Appendix A.5, where the 5 surfaces in the EAF were considered (1-roof, 2-wall, 3-solid scrap, 4-molten metal, 5-arc).

3.4.1 Effect of slag foaming

As discussed in Section 3.2, slag foaming does have a great contribution in terms of the energy efficiency in the EAF. This efficiency can increase from 40% to 90% as proposed by Fruehan [1998]. As the foam covers the arc, less energy would be lost to the furnace roof and walls and to capture this effect in the radiation model,

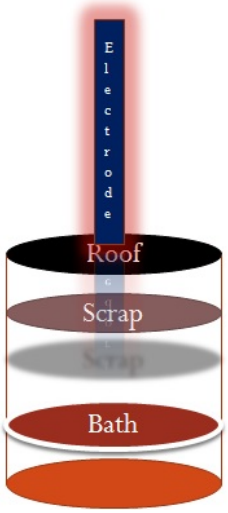

Figure 3.3: EAF surfaces

the following method was adopted. This was modeled using an efficiency factor (E_f) which is the product of two parameters E_1 and E_2.

$$E_f = E_1 E_2 \tag{3.58}$$

E_1 relates the fraction of the arc covered by the foam to the fraction of radiation that is shielded from the wall and rather being transferred directly to the steel. MacRosty and Swartz [2005] assumed that a maximum value of 70% efficiency is achieved when the arc is fully covered by the arc and a constant arc length of 0.5 m was also assumed. E_1 is related to the foam height as shown in the hyperbolic tangent relationship below.

$$E_1 = 0.7\ (\frac{1}{2}\tanh(\alpha_1 H_f + \beta_1) + \frac{1}{2}) \tag{3.59}$$

in which α_1 and β_1 are tuning parameters and are set to 5 and -1.25 respectively. E_2 relates the slag foaming efficiency to the amount of scrap present in the furnace. This is to ensure that as more scrap is present, the amount of slag foaming will be

diminished accordingly. The more solid scrap present in the furnace, the higher the probability that the slag foaming would form in the void spaces of the scrap and the harder it would reach the arc (MacRosty and Swartz [2005]). It was assumed that when the solid scrap decreases to less than 20% of the initial charge mass, the value of E_2 will approach unity as represented by the hyperbolic tangent relationship,

$$E_2 = \frac{1}{2}\tanh(\alpha_2(1 - \frac{\text{current scrap mass}}{\text{initial scrap mass}}) + \beta_2) + \frac{1}{2} \tag{3.60}$$

Same as in equation (3.59), α_2 and β_2 are tuning parameters for the hyperbolic tangent function and are set to 3.2 and -1.29 respectively.

3.5 Assumption regarding the melt rate

In equation (3.2), the melt rate was a function of both the latent heat of fusion and the sensible heating. It was found that such formulation caused several numerical issues during the model integration and the linearization phase, as will be discussed in chapter 5. The removal of the term $C_p(T_{melt} - T_{ss})$ was investigated which results in the following modified expression for the melt rate of solid scrap.

$$\dot{m}_{melt}\Delta H_{fusion}k_{dm} = Q_{ss}^{net}\frac{T_{ss}}{T_{melt}} \tag{3.61}$$

Through inspecting the profiles of ($[\Delta H_{fusion}\frac{T_{melt}}{T_{ss}}]$) and ($[\Delta H_{fusion} + C_p(T_{melt} - T_{ss}]\frac{T_{melt}}{T_{ss}}$) in the rearranged form of equation (3.2) as shown below,

$$\dot{m}_{melt}(\Delta H_{fusion} + C_p(T_{melt} - T_{ss}))k_{dm}\frac{T_{melt}}{T_{ss}} = Q_{ss}^{net} \tag{3.62}$$

it was found that both terms have similar dynamics using the same k_{dm} value as

shown in Figure 3.4 below.

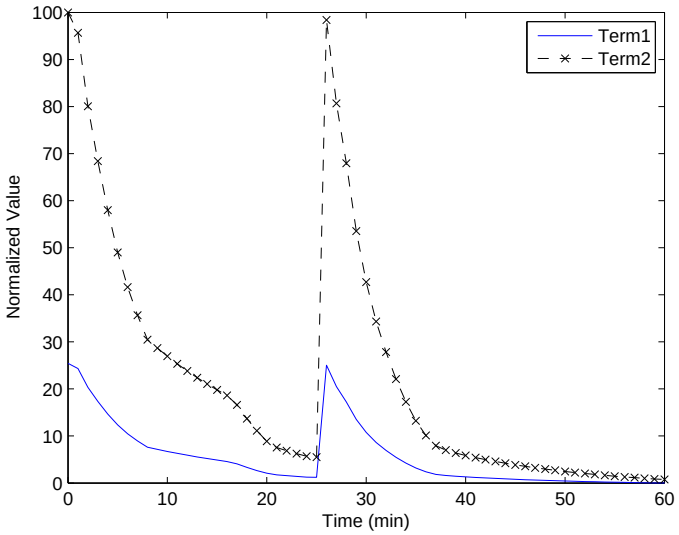

Figure 3.4: Comparing the trajectories for term1 representing $[\Delta H_{fusion}\frac{T_{melt}}{T_{ss}}]$ and term2 representing $([\Delta H_{fusion} + C_p(T_{melt} - T_{ss}]\frac{T_{melt}}{T_{ss}})$

It could be observed that the parameter k_{dm} can be used to compensate for neglecting the sensible heat from the melting rate equation and approximate it using equation (3.61).

This assumption is very reasonable, since the melt rate in all literature is fairly uncertain due to the lack of measurements that would validate the speed of scrap melting in the real furnace. Figures 3.5 and 3.6 show the mass of solid scrap and the melt rate of scrap for both scenarios. It could be shown that the approximation made is fairly accurate and both formulations give similar performance using different values for the melting rate parameter k_{dm}. All the profiles have been normalized between 0 and 100 based on the normalization procedure given in Appendix A.6.

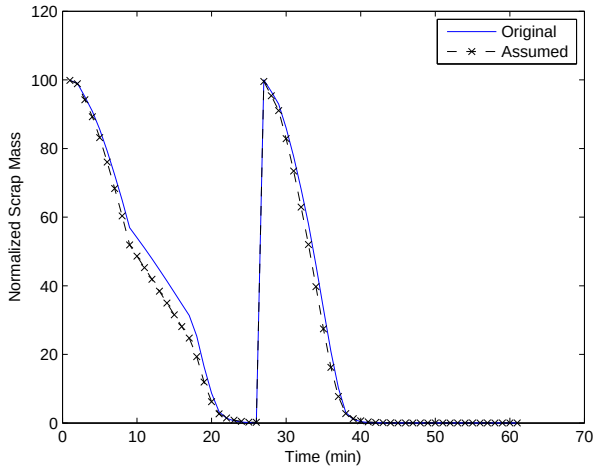

Figure 3.5: Mass of solid scrap in the furnace

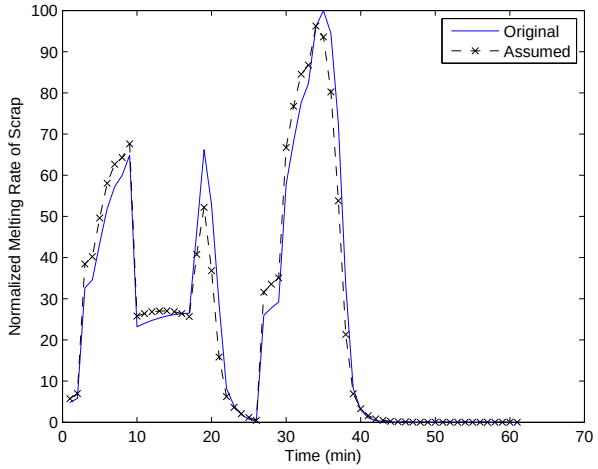

Figure 3.6: Melting rate of scrap

3.6 Comparing different melting scrap geometry

As has been discussed previously, two approaches were considered through modeling the radiation part and specifically the geometry of the solid scrap melting. MacRosty and Swartz [2005] considered the solid scrap melting geometry as a cone-frustum and the other approach used in this work did consider it as a flat surface. The benefits gained from considering the scrap melting geometry as a flat surface, includes simpler dynamics in terms that the solid scrap does not emit radiation to itself, beside the simplicity of the dynamic surface area calculations for a disk rather than a cone where the angle of repose keeps changing. However, before finalizing the use of this approach a case study was conducted to see the overall effect on important variables most affected by the radiation part, such as the gas temperature in the freeboard gas volume, the dynamics of scrap melting, the roof temperature and the wall temperature. Figures 3.7 to 3.10 show the trajectories of the corresponding variables for the two scrap geometries. A similar gas temperature profile was obtained for both cases as shown in Figure 3.7. The same applies to the wall temperature and mass of solid scrap as shown in Figures 3.8 and 3.10. A similar trend can be observed in Figure 3.9 for the roof temperature for both cases; however some offset occurs. In terms of actual temperature, the offset is less than 8 K. The normalization was carried out as discussed in Appendix A.6. Those results were obtained using the same set of parameters for the whole model. Adjusting some parameters could likely lead to closer matching profiles. The motivation of such an assumption, is that no one really knows if the scrap melts as a flat surface, cone or other geometrical form due to the complexity of the process. Therefore the simplest configuration that would facilitate the modeling of the process and enhance different algorithms (such as linearization, etc.) without undue loss of accuracy, is preferable.

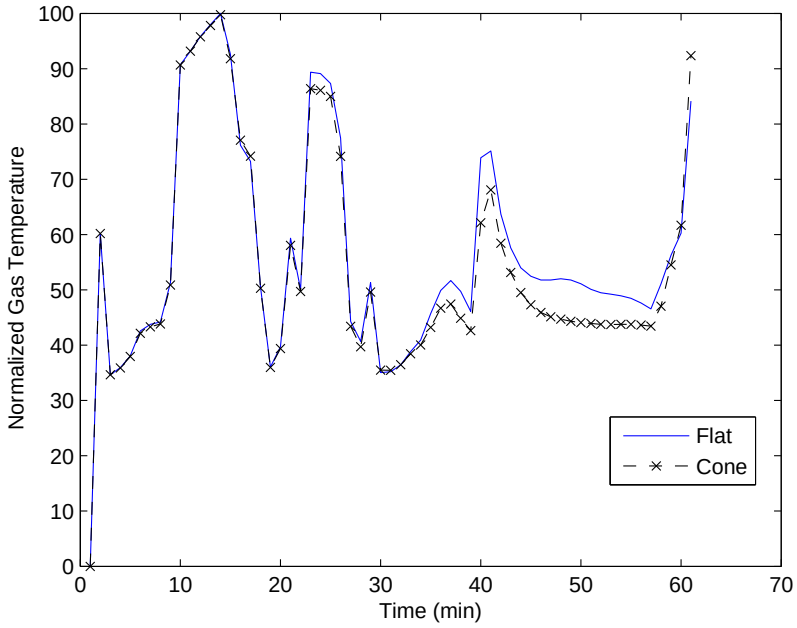

Figure 3.7: Temperature of the gas zone

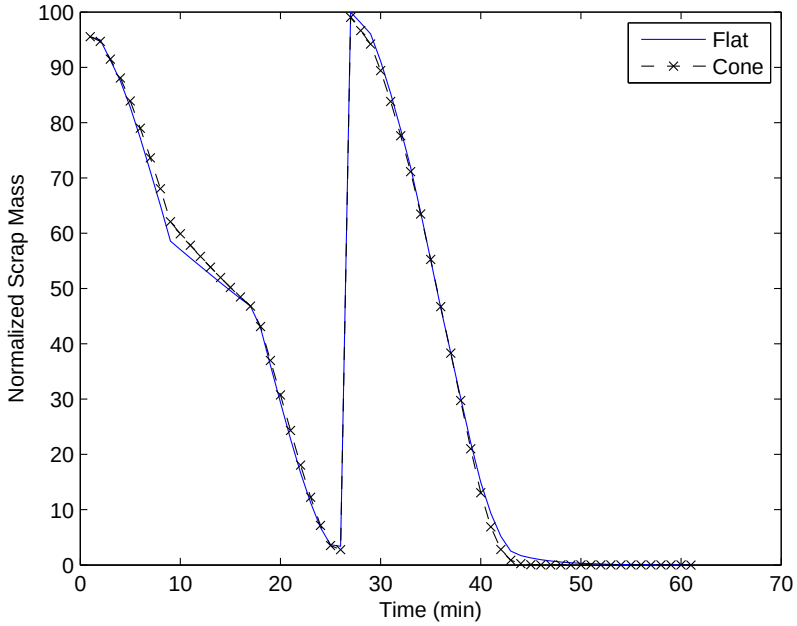

Figure 3.8: Mass of solid scrap in the furnace

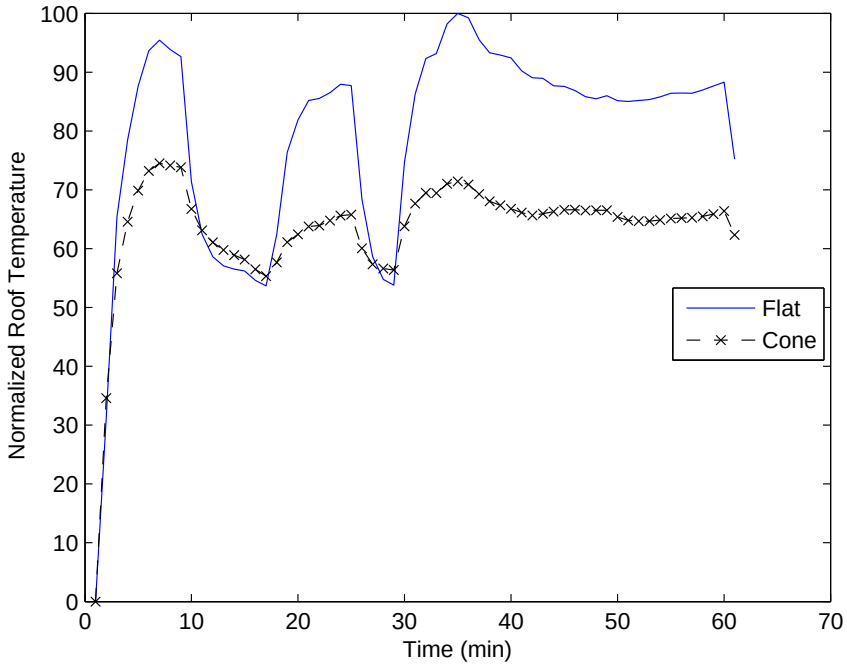

Figure 3.9: Temperature of the roof of the furnace

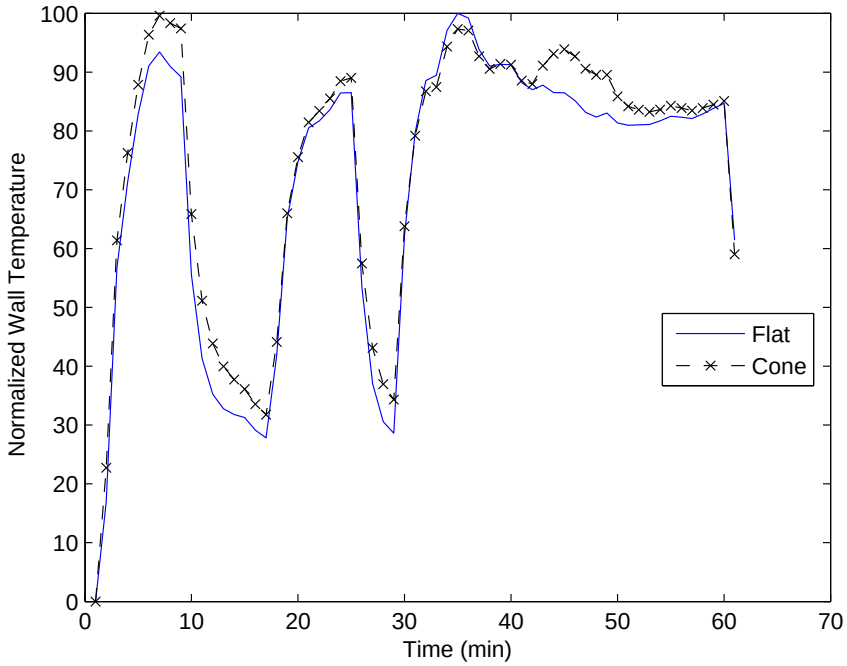

Figure 3.10: Temperature of the wall of the furnace

3.7 Simulation Studies

In this section, a base case study for the nominal operation of the furnace is shown. Some of the trajectories could not be validated, as result of the lack of their measurements from the plant. However, to ensure the reliability of the trajectories, some insight based on feedback from steel makers was taken into account in addition to what has been discussed in the literature. All the profiles have been normalized as discussed in Appendix A.6. The power profile is shown in Figure 3.11, where it can be noticed that after adding the first charge the power is turned to minimum and rather the burners are used to enhance the preheating of the scrap. Then, the power is turned on, and at t=25 min the power is turned off at which point the roof is swung open and the second charge is added. Then the power is turned back on until the end of the batch.

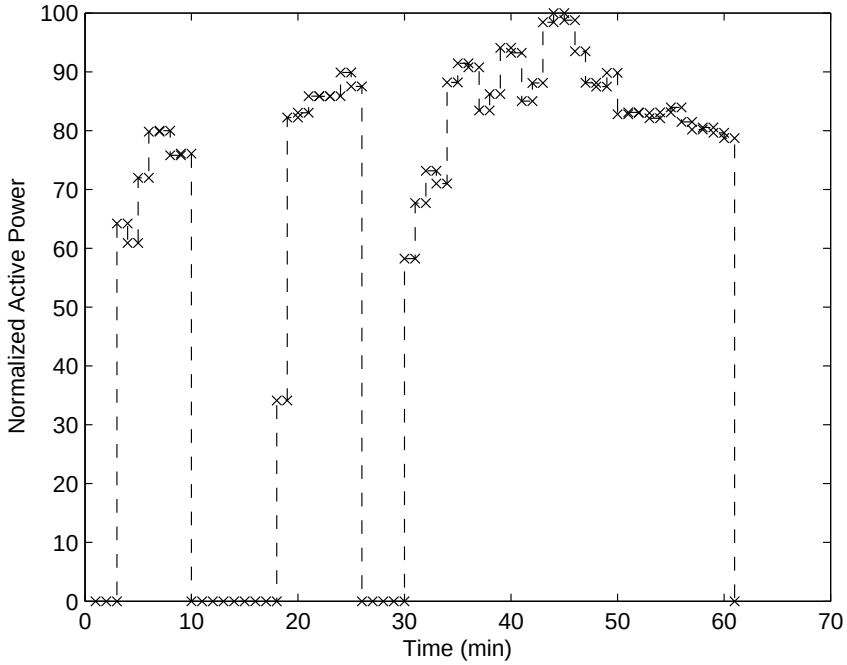

Figure 3.11: Active power trajectory

The jetbox profiles are shown in Figure 3.12. The switch function is then used to split the amount of oxygen injected between the gas zone and the slag zone. On the other hand, the methane profile is shown in Figure 3.13, and the high flow during the initial stages of scrap addition to enhance the preheating of the scrap can be observed. Figure 3.14 shows the temperature profiles for the molten metal, solid scrap and gas

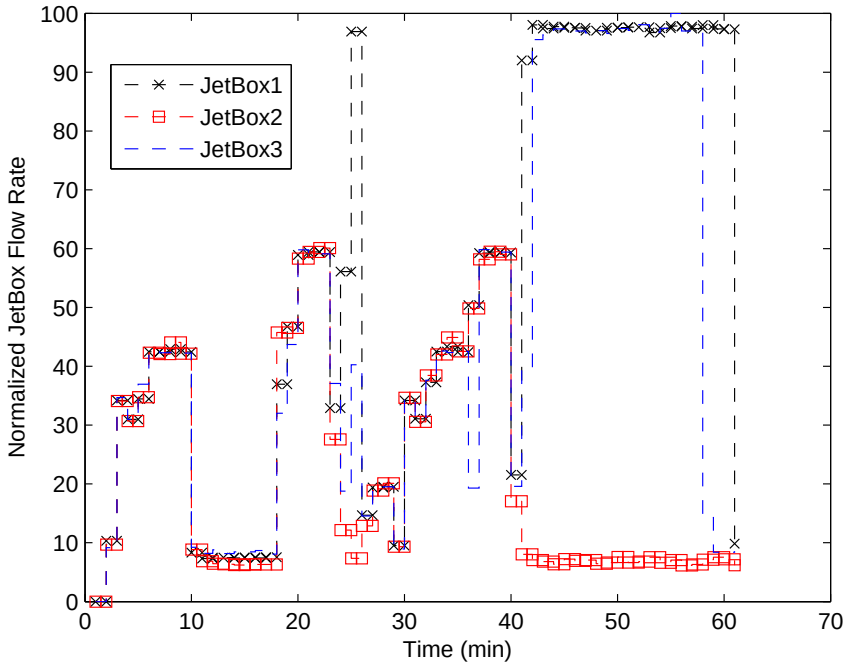

Figure 3.12: JetBox trajectories

zones. The drop in the molten metal temperature from t=0 min to t=18 min is mainly due to the heat lost to the scrap to enhance the melting process. Then it starts to increase as a result of power from the arc, and then at t=25 min it starts dropping again due to the addition of the second charge before it increases again until the end of the batch. The gas zone temperature keeps fluctuating, as result of the burner additions that increase the temperature of the gas zone and the water sprays that cool down the gas zone, in addition to energy lost to the scrap at the initial minutes of scrap addition.

The scrap zone temperature starts at ambient temperature and continue to increase, until the addition of the second charge where it drops back to ambient temperature. Then the scrap temperature keeps increasing but never exceeds the melting temperature.

The mass of scrap and molten metal profiles are shown in Figure 3.15. The mass of solid scrap starts with the first charge which keeps melting until sufficient space is available within the furnace, and then the second charge is added and the melting procedure continues until all the scrap is melted. The molten metal mass starts with the heel present from a previous batch and continues to increase until it reaches a plateau, which represents the flat bath conditions where all the scrap has melted. The offgas composition is shown in Figure 3.16, while the roof and wall temperatures are shown in Figure 3.17. The slag foam height is shown in Figure 3.18, where it can be seen to reach the highest level when the flat bath conditions have been reached.

The simulation time in gPROMS using a quad-core i7-intel 3.5 GHz processor is approximately 4-5 CPU seconds.

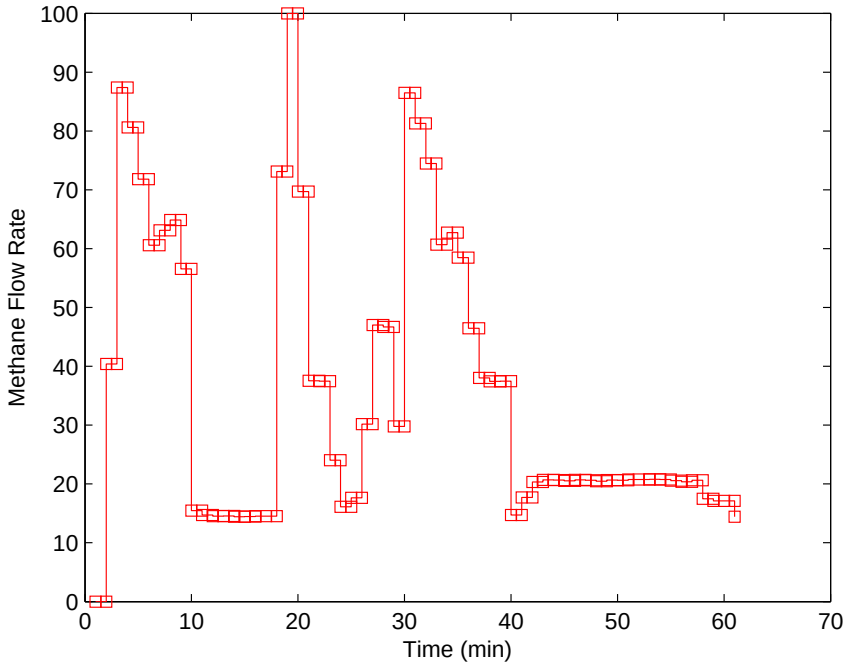

Figure 3.13: Natural gas trajectory

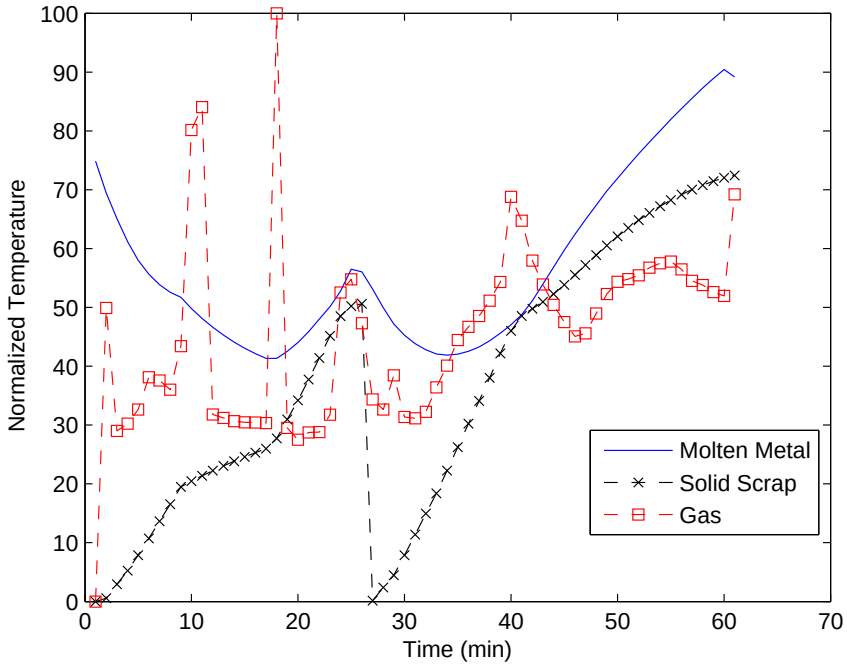

Figure 3.14: Temperature trajectories

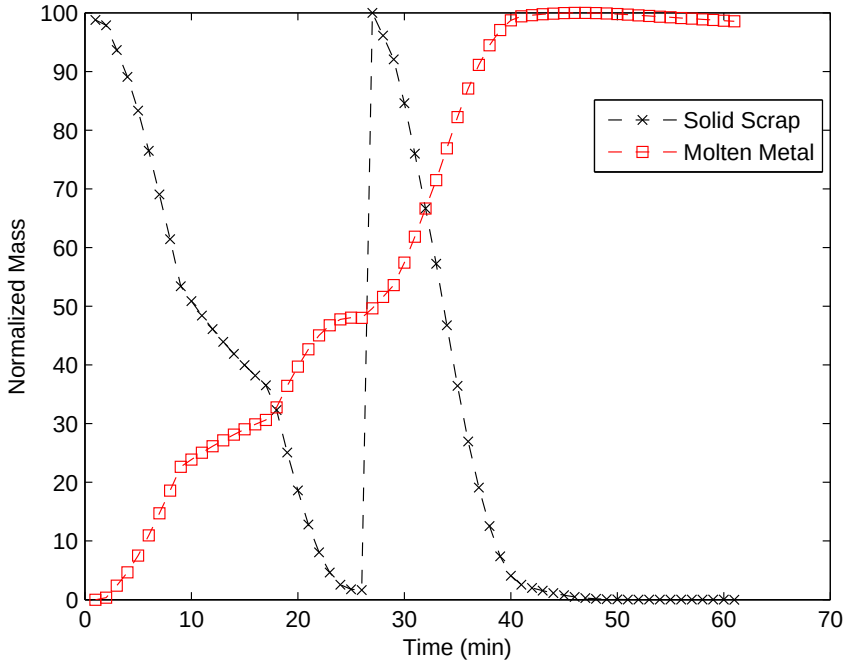

Figure 3.15: Mass of Scrap and Molten Metal trajectories

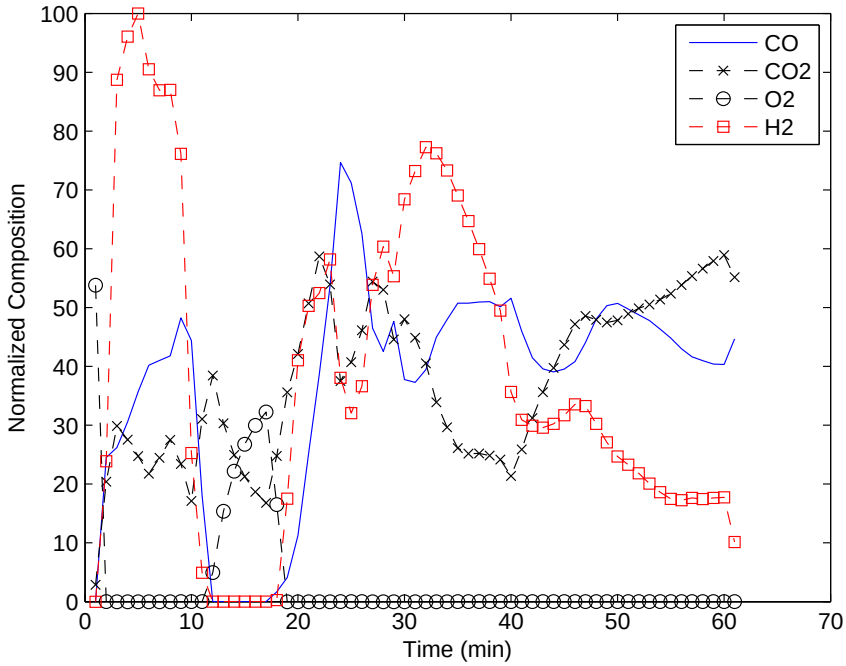

Figure 3.16: Offgas composition trajectories

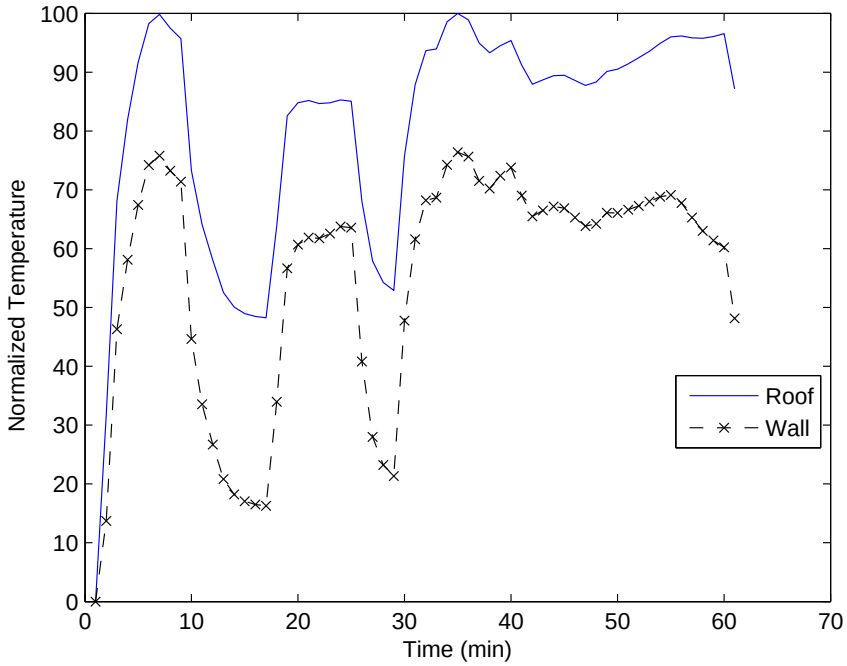

Figure 3.17: Roof and Wall temperature trajectories

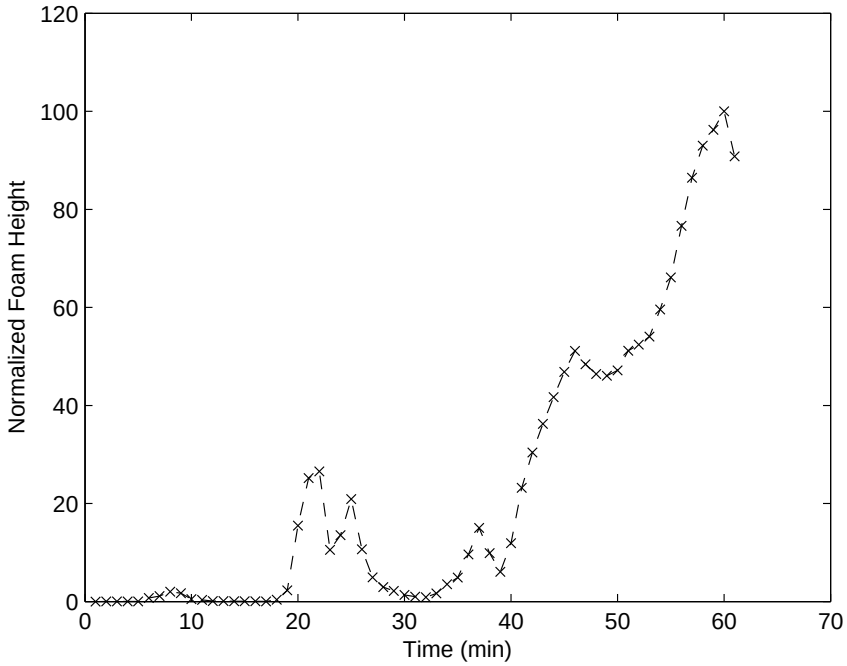

Figure 3.18: Foam height trajectory

Chapter 4

Parameter Estimation, Sensitivity Analysis and Economic Optimization

The intent of this chapter is to show how the model is validated using plant data as will be shown in section 4.1. Sensitivity analyses will be used to determine the effect of the solid scrap components and flux materials on the EAF operation. Then, the economic optimal performance of the furnace will be investigated through formulating an optimization problem in section 4.4.

4.1 Parameter Estimation and Model Validation

The next stage after developing the model as discussed in Chapter 3, is to validate it using industrial data obtained from the plant. This stage of the model validation is considered very challenging due to the complexity of the model and due to the lack of continuous measurements. The model contains 28 parameters to be estimated

and the only continuous measurements that exist, are the CO, CO_2, O_2 and H_2 offgas compositions. Some discrete measurements exist which are the molten metal temperature, slag composition and end-point carbon content in the molten bath. The 28 parameters are shown in Table 4.1, which describes the role of each parameter in the model formulation. It is unlikely that all the parameters can be accurately and uniquely estimated, and therefore a sensitivity analysis is required to identify the most sensitive parameters. This will minimize the number of parameters that are required to be estimated and reduce the complexity of the estimation problem.

4.1.1 Sensitivity Analysis

The first stage of parameter estimation is to identify an initial good set of parameters. Through using a brute force method, every parameter is perturbed above and below a nominal value and the mean of square prediction error (MSPE) is calculated for the response variables representing the measurements.

$$\text{MSPE} = \frac{1}{N}\sum_{i}^{N}\left(y_i^{predicted} - y_i^{measured}\right)^2 \tag{4.1}$$

The set of parameters values with the least MSPE is selected to be a good set to proceed with. The initial set of parameters used before performing the brute force method was obtained from literature values (MacRosty and Swartz [2005]).

The sensitivity analysis is performed using local differential analysis ($\frac{\partial y_k}{\partial p_i}$), where it is approximated using forward finite difference method as shown below,

$$\frac{dx}{dt} = f(x, p, u) \tag{4.2}$$

$$y = h(x, p, u) \tag{4.3}$$

Table 4.1: Roles of parameters in the model

No.	Parameter	Equation	Role in Model
1	k_{cool}	(3.8)	Heat transfer coefficient for scrap cooling from second charge
2	k_{dm}	(3.2)	Accounts for bulk density and composition variation in scrap melting
3	k_{dt}	(3.10)	Accounts for bulk density and composition variation in temperature profile of scrap
4	k_p	(3.7, 3.16, 3.56)	Power factor
5	k_{t1}	(3.4, 3.17)	Heat transfer coefficient between the solid scrap and the molten metal zones
6	k_{t3}	(3.6)	Heat transfer coefficient between the solid scrap and the gas zones
7	k_m	(3.12)	Mass transfer coefficient between molten metal and slag-metal zones
8	k_{mcool}	(A.2)	Heat transfer coefficient for the cooling of molten metal due to water sprays
9	k_{t2}	(3.18, 3.42)	Heat transfer coefficient between the slag metal and the molten metal zones
10	sub	(A.1)	Accounts for composition variation in molten metal temperature profile
11	θ_L	(3.11, 3.35)	Lancing split fraction between the slag and molten metal zones
12	y_C^*	(3.13)	Equilibrium carbon concentration
13	γ_d	(3.14)	Bubble diameter
14	α_3	(3.44)	Tuning parameter for jetbox switch function
15	β_3	(3.44)	Tuning parameter for jetbox switch function
16	$Bias_{O_2}GS^\star$	(3.47)	To account for uncertainty in the oxygen flow into gas zone
17	EA_1	(A.6)	Parameter for estimating the offgas flow rate
18	EA_3	(A.7)	Parameter for estimating ingressed air
19	$Fstar_{H2O}$	(A.10)	Estimated parameter for water sprays
20	k_{oil}	(3.26)	Estimates the rate of combustion of volatile component
21	k_{PO2}	(3.24)	Mass transfer coefficient for oxygen diffusion between the slag and gas zones
22	θ_3	(3.44)	Tuning parameter for jetbox switch function
23	X_{oil}	(3.26)	To estimate the volatile organic component in scrap
24	$Bias_{O_2}SM^\star$	(3.48)	To account for uncertainty in the oxygen flow into slag-metal zone
25	k_c	(A.9)	Estimates the fraction of carbon that reacts
26	k_{cao}	(3.37)	Dissolution constant for lime/dolomite
27	k_{dc}	(3.36)	Dissolution constant for carbon
28	h_{gs}	(3.28, 3.29)	Heat transfer coefficient for gas cooling

$$\frac{\partial y_k}{\partial p_i} = \frac{y_k(p_i + \Delta p_i) - y_k(p_i)}{\Delta p_i} \tag{4.4}$$

in which Δp is the magnitude of the change in the parameter and the numerator represents the change in the response variable. Rigorous differential sensitivity analysis could not be applied due to the lack of Jacobian information in gPROMS and due to the complexity of the model, if it was to be calculated without the aid of a software. Each parameter was perturbed by 5%. The simulation is carried out in gPROMS, which takes care of the relationships between the output variables, state variables and the parameters. The sensitivity analysis was performed on 13 response variables. The gas zone response variables are the carbon monoxide (CO), carbon dioxide (CO_2), oxygen (O_2) and hydrogen (H_2) compositions in the offgas system, in addition to the gas temperature. The slag zone response variables are the composition of iron II oxide (FeO), silicon dioxide (SiO_2), magnesium oxide (MgO), aluminum oxide (Al_2O_3) and calcium oxide (CaO). The molten metal zone response variables are the molten metal temperature and the carbon fraction in the molten bath. Finally, the solid scrap temperature is also included. It could be noticed that some of the response variables do not exist in the real plant measurements; however including such variables is very important in the parameter sensitivity analysis in order to capture the dynamic behaviour of the those variables in the EAF operation.

The sensitivity is calculated along the batch trajectory forming a vector. In order to normalize with respect to the magnitude of both the parameters and the response variables, the sensitivity vector is multiplied by a ratio of the nominal values of the parameters and the response variables, as shown below,

$$s_{i,k} = \frac{p_i^0}{y_k^0} \times \left[\frac{\partial y_k(t_1)}{\partial p_i} ..... \frac{\partial y_k(t_{nt})}{\partial p_i}\right]^T \tag{4.5}$$

where $s_{i,k}$ represents the normalized sensitivity of response y_k to parameter p_i. The nominal value of the response variable was considered the mean of the base case

trajectory and the nominal value of the parameter is the initial value of the parameter. In order to obtain a single metric for the sensitivity vector, the euclidean norm is used.

$$||s_{i,k}|| = \sqrt{\sum_j \left(\frac{p_i^0}{y_k^0} \times \frac{\partial y_k(t_j)}{\partial p_i}\right)^2} \tag{4.6}$$

The overall effect of each parameter using the combination of all measurements would be calculated as,

$$||s_{i,\text{combined}}|| = \sqrt{\sum_k \sum_j \left(\frac{p_i^0}{y_k^0} \times \frac{\partial y_k(t_j)}{\partial p_i}\right)^2} \tag{4.7}$$

Figures 4.1 to 4.4 show the effect of the parameters on all the response variables being considered in the sensitivity analysis process.

As shown in Figure 4.1, the molten metal carbon content was found to be highly affected by θ_L, which is the lancing split fraction. The molten metal temperature is highly affected by the parameters k_{dm} and k_p.

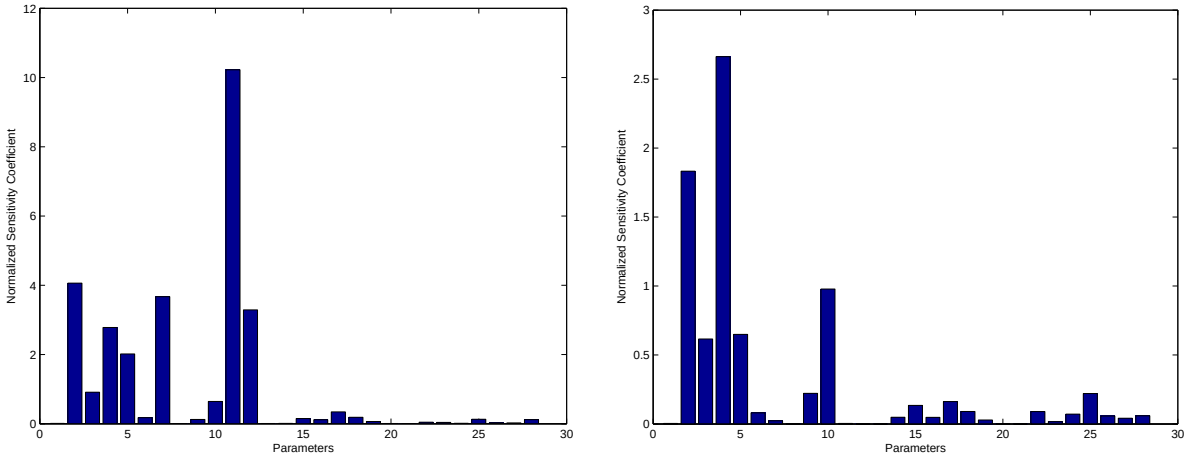

(a) Sensitivity analysis on the molten metal carbon content

(b) Sensitivity analysis on the molten metal temperature

Figure 4.1: Sensitivity analysis on the molten metal zone

In Figure 4.2, it can be seen that β_3, EA_1 and EA_3 are the major parameters that affect the CO, CO_2 and H_2 offgas compositions. EA_1 has the highest influence on the oxygen concentration in the offgas. h_{gs} shows a strong effect on the CO_2 composition, while α_3 shows a strong effect on the H_2 composition.

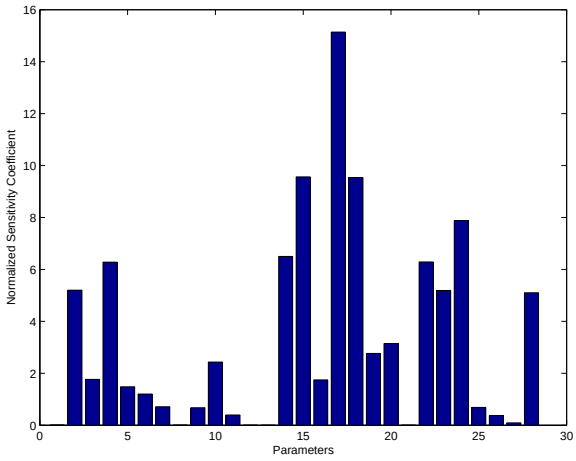

(a) Sensitivity analysis on the offgas carbon monoxide composition

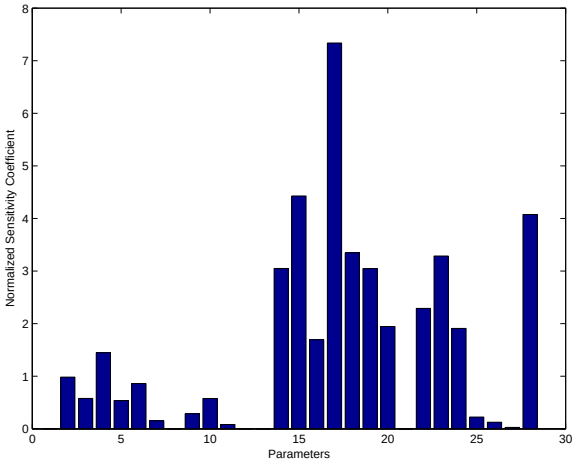

(b) Sensitivity analysis on the offgas carbon dioxide composition

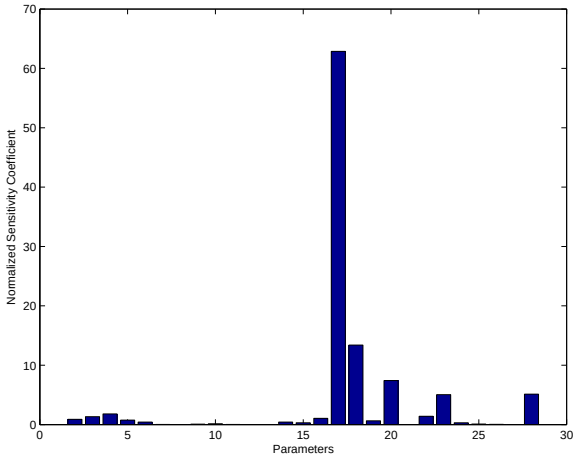

(c) Sensitivity analysis on the offgas oxygen composition

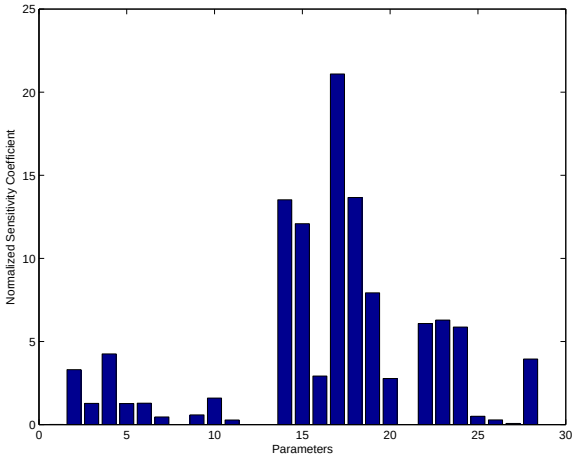

(d) Sensitivity analysis on the offgas hydrogen composition

Figure 4.2: Sensitivity analysis on the offgas composition

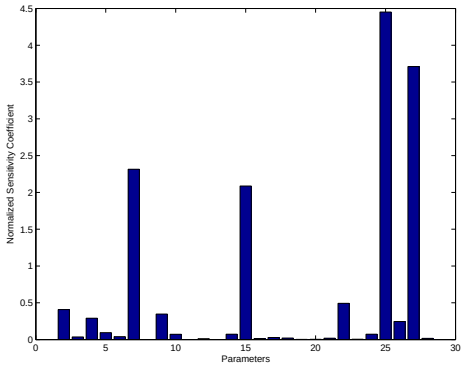

(a) Sensitivity analysis on the slag FeO composition

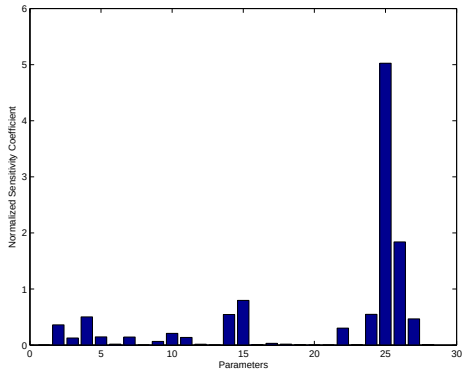

(b) Sensitivity analysis on the slag MgO composition

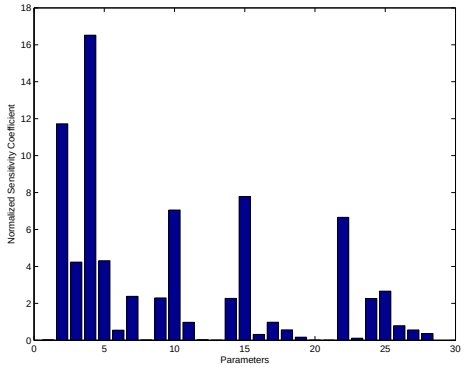

(c) Sensitivity analysis on the slag SiO_2 composition

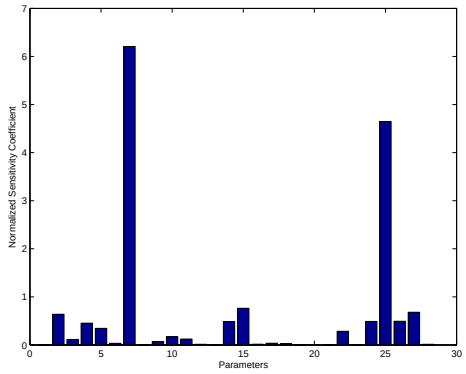

(d) Sensitivity analysis on the slag Al_2O_3 composition

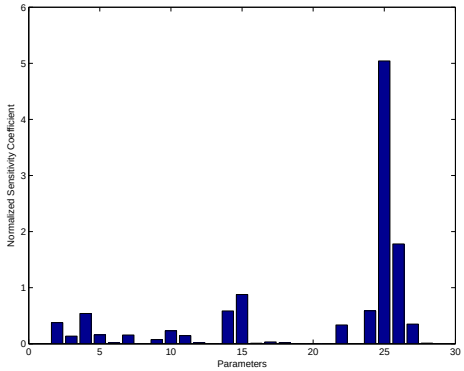

(e) Sensitivity analysis on the slag CaO composition

Figure 4.3: Sensitivity analysis on the slag-metal zone

Figure 4.3 shows the sensitivity results of the parameters on the slag composition, it can be seen that k_c and k_{dc} have the highest effect on the FeO concentration.

Also, k_c has a dominant influence on the MgO and CaO concentration in the slag phase. k_m and k_c show the highest influence on the Al_2O_3 concentration. Finally, the parameters k_{dm} and k_p show the greatest effect on the SiO_2 content in the slag.

In Figure 4.4, the effect of the parameters on the solid scrap and gas temperatures is represented. The parameters k_{dm}, k_{dt}, k_p and k_{t1} have the highest influence on the scrap temperature. On the other hand, the parameters α_3, β_3, EA_1, EA_3 and h_{gs} have the highest effect on the gas temperature.

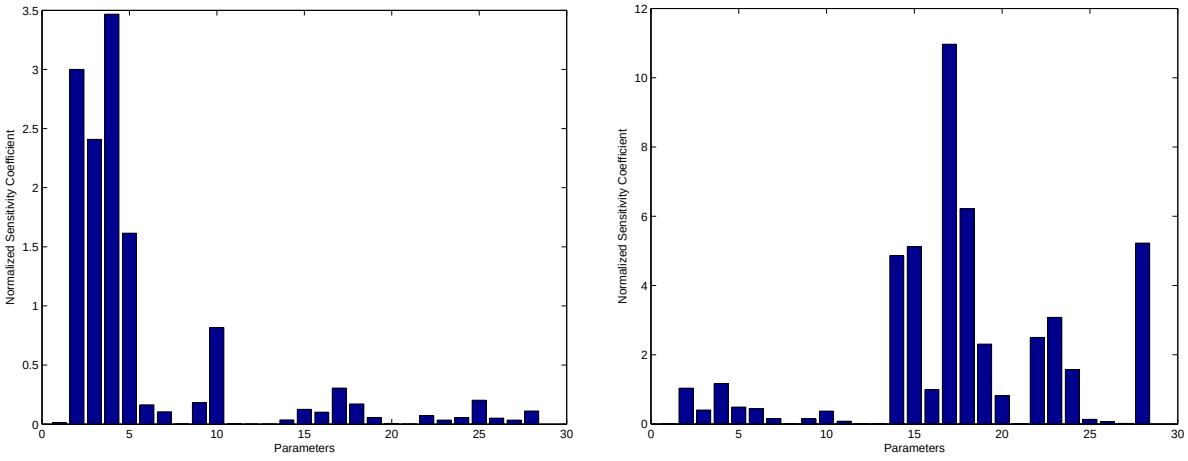

(a) Sensitivity analysis on the solid scrap temperature

(b) Sensitivity analysis on the gas temperature

Figure 4.4: Sensitivity analysis on the gas and scrap temperatures

Figure 4.5 shows the summary of the overall effect of the parameters on all the measurements combined. The parameters k_{dm}, k_p, α_3, β_3, EA_1 and EA_3 are the most sensitive in the model.

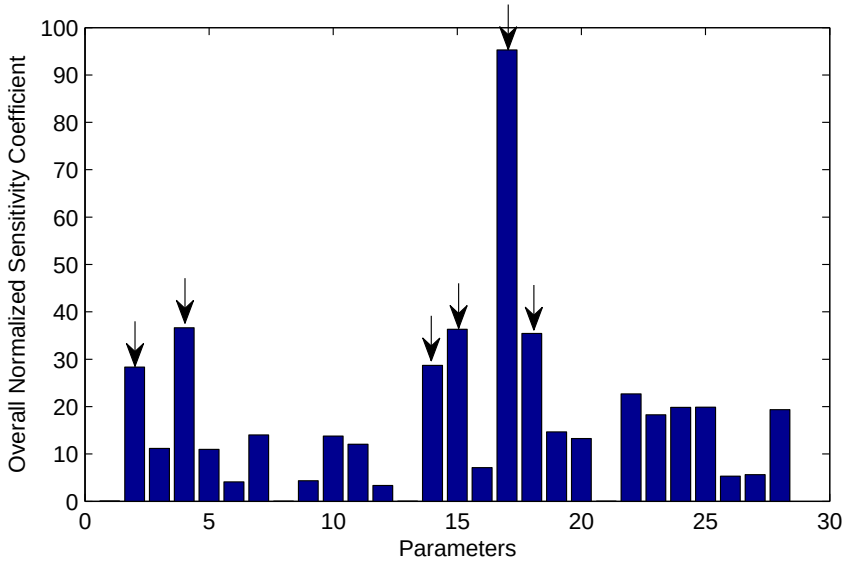

Figure 4.5: Sensitivity analysis on combined measurements

4.2 Parameter Estimation

The most sensitive parameters k_{dm}, k_p, α_3, β_3, EA_1 and EA_3 were estimated using gEST/gPROMS, following the procedure described below.

Measurements

Ouputs: The available continuous measurements from the plant are the offgas composition of oxygen, hydrogen, carbon monoxide and carbon dioxide. Discrete measurements are the slag composition (FeO, MgO, Al_2O_3, SiO_2 and CaO), as well as the molten metal temperature and the end-point carbon content in the molten metal.

Inputs: The inputs measured and used in parameter estimation are the active power, the amount of scrap charged, carbon, lime and dolomite additions, as well as materials being injected which are oxygen, methane and carbon and finally the water from the sprays.

Challenges

Estimating the parameters is challenging due to the limited measurements that are obtained and accessible from the plant. The more continuous measurements available, the more accurate the estimation of the data will be for the entire batch. The only continuous measurements available are the offgas compositions and these still have some uncertainty due to the nature of the furnace operation. This is mainly due to the water leaks that might occur, as well as the roof opening routine which allows some components to enter or exit the furnace. The absence of offgas flow rate and offgas temperature measurements makes the validation of the energy balance in the model very hard. This is due to the inability to validate the gas temperature trajectory and the offgas flow rate, and both variables would greatly affect the offgas composition. Only one measurement is available for the slag composition, which represents a single time point measurement. The availability of continuous slag measurements is likely to improve the estimation of the slag zone properties. One or two sample measurements usually exist for the molten bath temperature. The molten metal temperature is important, because it decides when the molten metal will be tapped out of the furnace, when it reaches a certain temperature (tap temperature). Due to the lack of continuous molten metal temperature measurements, the profile of the molten metal temperature between the sample measurements that were obtained is usually unknown. Due to this shortage of measurements, a lot of model assumptions (such as constant offgas flow rate, no direct heat transfer from the arc to the slag and the rest was discussed in Chapter 3) are usually required. If those measurements are available in the future, more complexity (such as dynamic offgas flow rate, etc.) could be added and validated in the model.

4.2.1 Raw Data

The raw data provided by the plant is obtained from the EFSOP system that is used by the industrial partner. The slag composition is obtained using a slag analyzer. The molten metal carbon content and molten metal temperature were obtained from laboratory analysis. Data refining is critical in this work, since some overlapping between the batches requires an insight of all the variables to decide when the batch starts and ends. Some of the batches were missing some of the heat logs, which could show if any problems occurred during the plant operation, such as the breakage of electrodes, etc. High precision predictions do not exist in the literature due to the above.

4.2.2 Maximum Likelihood Function

The parameter estimation is formulated as a dynamic optimization problem, where the parameters are treated as decision variables. The objective is to minimize the deviation of the model predictions from the plant data. Partial discretization was used, in which the control variables were discretized with a sample time of one minute and the states were treated as continuous variables. The estimation problem was then solved using the gEST/gPROMS software package. The maximum likelihood function is shown below,

$$\phi = \frac{N}{2} ln(2\pi) + \frac{1}{2} \min_{\theta} \sum_{i=1}^{NE} \sum_{j=1}^{NV_i} \sum_{k=1}^{NM_{ij}} \left(ln(\sigma_{ijk}^2) + \frac{(\tilde{z}_{ijk} - z_{ijk})^2}{\sigma_{ijk}^2} \right) \tag{4.8}$$

in which N is the total number of measurements for all the experiments, NE is the number of experiments performed, θ is the set of model parameters to be estimated, NV_i is the number of variables measured in the i^{th} experiment, NM_{ij} is the number of measurements of the j^{th} variable in the i^{th} experiment, $\tilde{z}_{ijk}$ is the k^{th} measured

value of variable j in experiment i, z_{ijk} is the k^{th} model predicted value of variable j in experiment i and σ_{ijk} is the standard deviation of the k^{th} measurement of variable j in experiment i. This formulation is flexible regarding the definition of the variance model. Choosing a defined variance model would reduce the above formulation to a weighted least squares problem, since in this case σ_{ijk} would be fixed (Process Systems Enterprise Ltd. [2004]).

During the estimation problem, the parameters were scaled in gPROMS as shown in the equation below, in which θ_i^0 is the initial guess of the parameter and ϵ is set at 10^{-8} (Process Systems Enterprise Ltd. [2004]).

$$\theta = \frac{\theta_i}{d_i}$$
$$d_i = \begin{cases} \theta_i^0, if \quad |\theta_i^0| > \epsilon \\ \frac{1}{2}(\theta_i^{max} - \theta_i^{min}), \ otherwise \end{cases} \tag{4.9}$$

Table 4.2: Most Sensitive Estimated Parameters

Parameter	**Estimate**
k_p	8×10^{-1}
k_{dm}	4.5×10^{-1}
α_3	3.7×10^{-1}
β_3	1.11×10^{-2}
EA_1	1.3×10^{-1}
EA_3	1.3

The values for the estimated parameters are shown in Table 4.2. The parameters estimated in gEST/gPROMS are shown here, while the values for the rest of the parameters are attached in Appendix B. 3-5 batches were used for the parameter

estimation as training data and one was used as a testing data set. The small number of data used for the estimation is due to shortage of accurate data sets that could be obtained from the plant.

4.2.3 Model Estimation Results

The model predictions for one data set that was used in parameter estimation will be presented. The model predictions for the offgas composition are shown in Figure 4.6 along with measured data from one of the data sets, in which it can be seen how the predictions reasonably follow the plant data. The mean squared prediction error for the selected heat and the average of the MSPE for the 4 batches are shown in Table 4.3. It can be observed that the MSPE for the selected heat is comparable to that of the average MSPE for all the data sets used for the parameter estimation.

The slag composition and molten metal temperature predictions are shown in Figures 4.7 and 4.8 respectively. The predictions are very close to the plant measurements which shows the accuracy of the model. It could be noticed how the model predicts the slag composition fairly well based on only a single data point.

Table 4.3: Mean Squared Prediction Errors

	Selected Heat MSPE	**Average Heat MSPE**
CO	5.7×10^{-3}	6.33×10^{-3}
CO_2	2.8×10^{-3}	5.27×10^{-3}
O_2	4.7×10^{-3}	3.13×10^{-3}
H_2	7.2×10^{-3}	1×10^{-2}

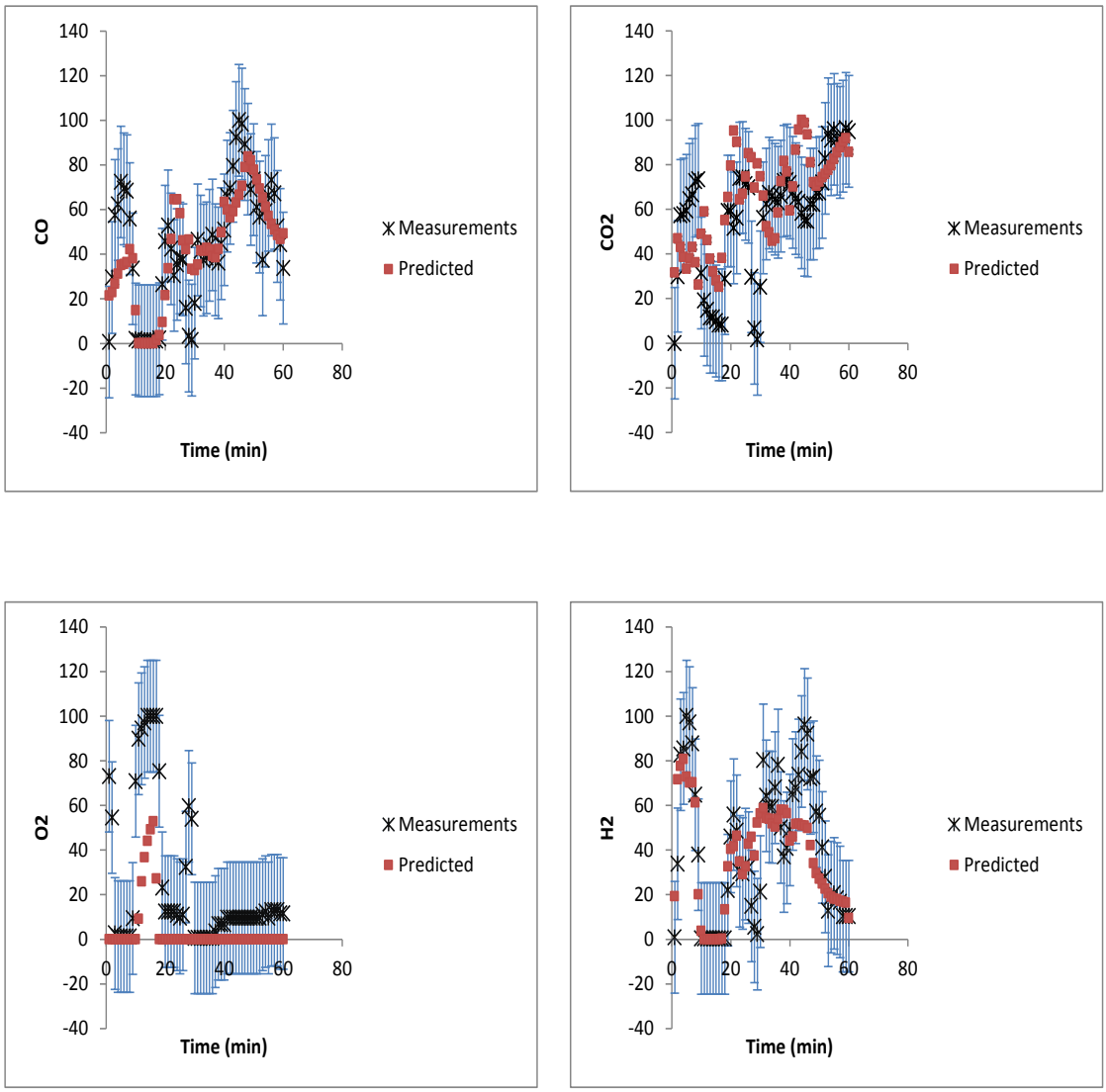

Figure 4.6: Normalized Offgas Chemistry Predictions

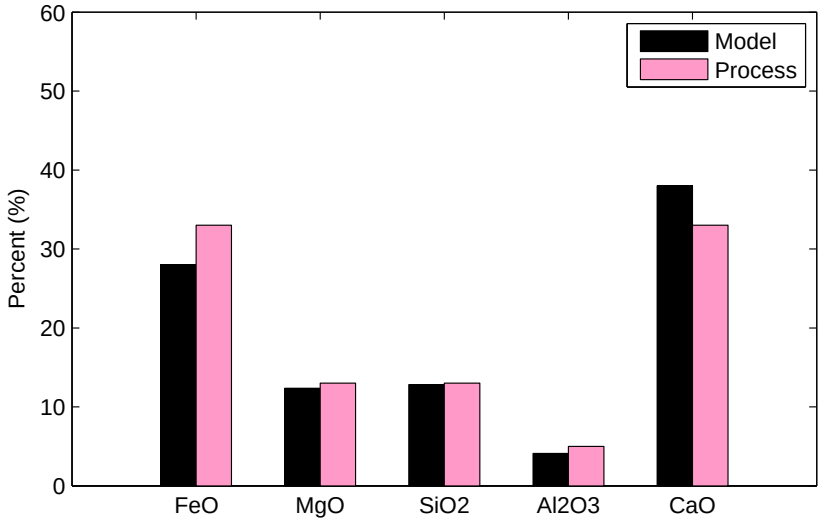

Figure 4.7: Slag Composition Predictions

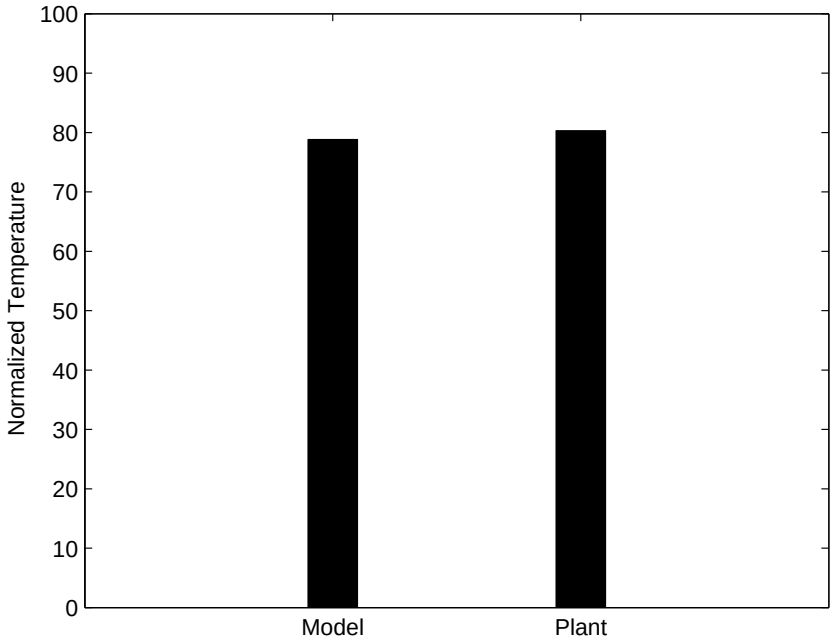

Figure 4.8: Molten Metal Temperature Prediction

4.3 Sensitivity Analysis on Scrap Composition

The electric arc furnace (EAF) uses different types of scrap grades and converts them to ferro-metal alloys. These scrap grades such as pig iron, red brass, etc. differ in metal composition, which has a direct effect on the composition of the slag, molten metal and zone temperatures within the furnace. Therefore, it would be interesting to investigate the effect of some of these scrap constituents, as well as flux additions, on the main outputs of the EAF. The metals that were considered in this case are iron (Fe), silicon (Si), aluminum (Al), carbon(C) and manganese (Mn). Also, oil content was considered since it is one of the volatile impurities that have an effect inside the furnace. The last two components that were considered are the purities of lime and dolomite to determine the effect of the fluxes on the operation of the furnace. Two types of oxides are formed during the EAF operation; fluxing oxides and refractory oxides. Fluxing oxides are the ones formed from the metallic elements Si, Al, Fe and Mn present in the scrap. Refractory oxides are CaO and MgO that prevent the damage of the refractory linings of the furnace from the acidity of the fluxing oxides formed. The idea is to maintain a balance between both oxides, in order to obtain a slag that has the appropriate physical properties for foaming (Pretorius and Carlisle [1998])

The sensitivity analysis was performed using the local differential method that was described in Section 4.1.1. Each parameter was perturbed by (5%) one at a time and the change in the response variables was recorded. 13 response variables were investigated, which are the molten metal temperature, molten metal carbon content, iron II oxide (FeO) slag composition, aluminum oxide (Al_2O_3) slag composition, silicon dioxide (SiO_2) slag composition, magnesium oxide (MgO) slag composition, calcium Oxide (CaO) slag composition, carbon monoxide (CO) gas composition, carbon dioxide (CO_2) gas composition, hydrogen (H_2) gas composition, oxygen (O_2) gas composition, solid scrap temperature and finally the gas temperature.

The objective is to find the most important scrap parameters that affect each response variable, as well as finding the overall effect of each parameter on all the variables combined. The sensitivity profiles were normalized and calculated in the same manner as has been discussed in Section 4.1.1. The sensitivity analysis algorithm was implemented in *Matlab*® and simulation results from gPROMS were transferred using the gO:MATLAB tool (Process Systems Enterprise Ltd. [2004]). The idea of this sensitivity analysis is that it will give insight into the effect of different scrap types that differ in metal composition within the furnace and help us better understand the effect of scrap composition on the EAF operation.

4.3.1 Effect of scrap composition on offgas chemistry

The results of the sensitivity analysis of the scrap components and flux additions on the offgas composition are shown in Figure 4.9. It could be noticed that the Fe, Si, C, Oil and CaO greatly affect the CO, CO_2, H_2 and O_2 content in the offgas system. Most metallic elements react with oxygen before carbon (Jones *et al.* [1998]) and a competition exists between the metals towards oxygen. Fe also plays a role, in which FeO has a great effect on the availability of oxygen, which influences the decarburization rate. Oil mainly exists in the gas zone and contains high number of atoms of carbon and oxygen and therefore, it is normal to observe its high effect on the offgas composition and specifically oxygen, since it requires large number of oxygen moles for combustion. Lime and dolomite also have an effect on the offgas composition. The basicity of the system affected by lime and dolomite is usually maintained at a certain level and therefore would affect the amount of fluxing oxides in the system. The fluxing oxides would in turn affect the offgas composition as a result of affecting the oxygen concentration in the EAF and as a result the decarburization rate. Calcination of lime also affects the offgas composition (Pretorius and Carlisle [1998]). Manganese was found to have the least effect on the offgas composition in

the furnace. Carbon is shown not to have a high effect on the oxygen concentration in the offgas system and this could be mainly due to the poor affinity it has for oxygen compared to the rest of the components.

The change of CO sensitivity with time due to Fe and C is shown in Figure 4.10. It could be noticed that from time t=39 min onwards, C starts to show a strong positive effect on the CO composition. Conversely, Fe shows a negative effect from time t=39 min until t= 58 min. A positive peak at t=30 min is observed for the CO sensitivity due to Fe, and this could be due to the reduction of FeO to form CO as has been discussed in Chapter 3.

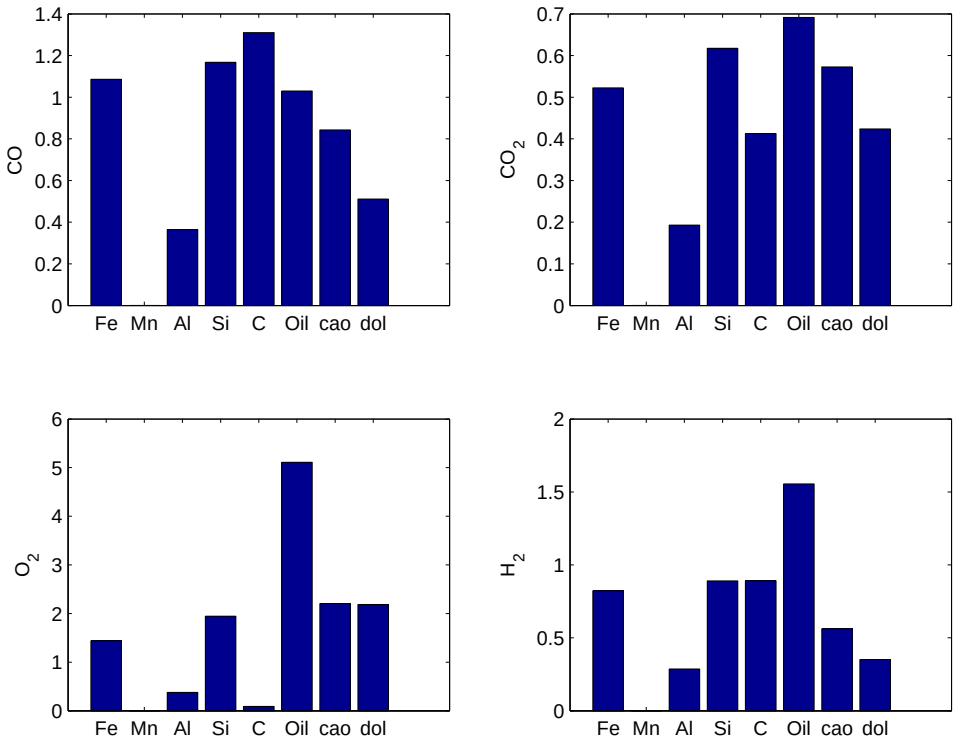

Figure 4.9: Effect of scrap composition and fluxes on offgas chemistry

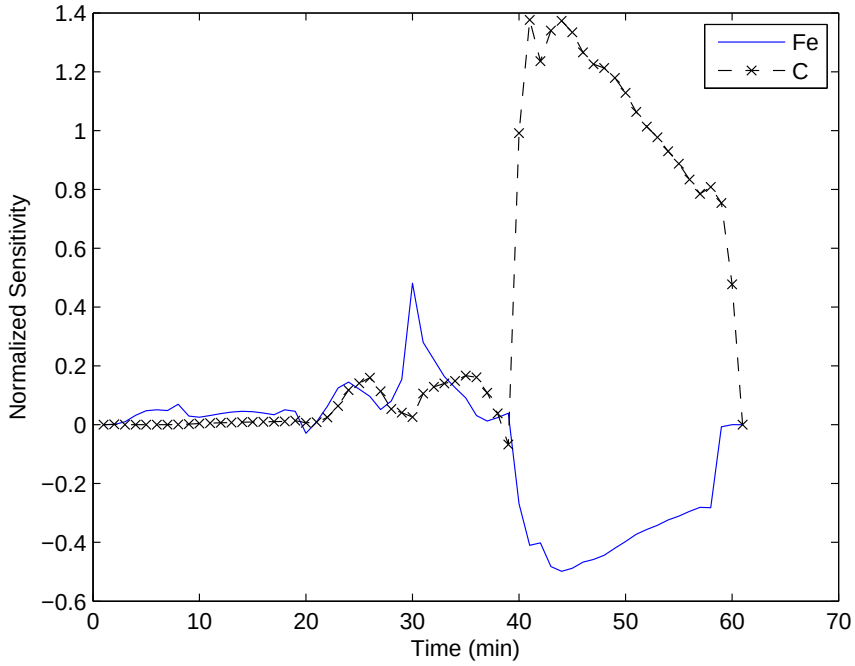

Figure 4.10: Effect of Scrap components on CO offgas composition

4.3.2 Effect of scrap composition on slag composition

The effect of the scrap components on the slag composition is shown in Figure 4.11. It can be noticed that unlike the case for the offgas composition, oil has a negligible effect on the slag composition. This is expected, since oil does not enter the slag phase and remain in the gas phase. Each compound would naturally be affected by its main metallic constituent, for example FeO is mainly affected by Fe, SiO_2 by Si, etc. Lime and dolomite play a role in maintaining the physical properties of the slag such as the viscosity, etc. It could be noticed that lime and dolomite have the largest influence on the MgO slag composition. This is mainly due to the maintenance of the physical properties of the slag to find the good combination between lime and dolomite along with the other oxides. The competition between Si, Al and Fe for oxygen affects their oxide formation and since all these elements react with oxygen

before carbon, carbon does not have a great effect on them. For the CaO formation, silicon is found to have an effect and this could be due to the basicity ratio (B_3), which is the ratio between CaO and Si that the steel industry always tries to keep at a constant desired limit.

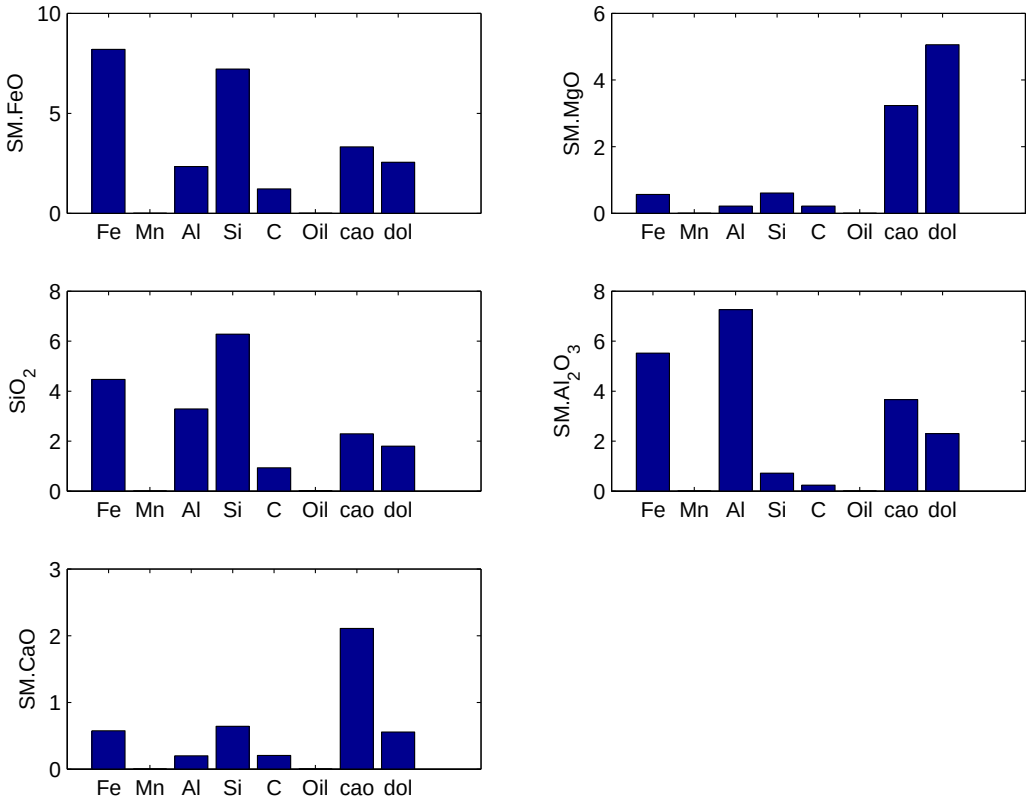

Figure 4.11: Effect of scrap composition and fluxes on Slag chemistry

Figure 4.12 shows the sensitivity change of FeO slag composition over time for both Fe and Si in the scrap. It could be observed that at time t=41 min until the end of the batch, Fe shows a strong positive effect and Si shows a comparable negative effect. This would be expected due to the competition between Fe and Si towards oxygen.

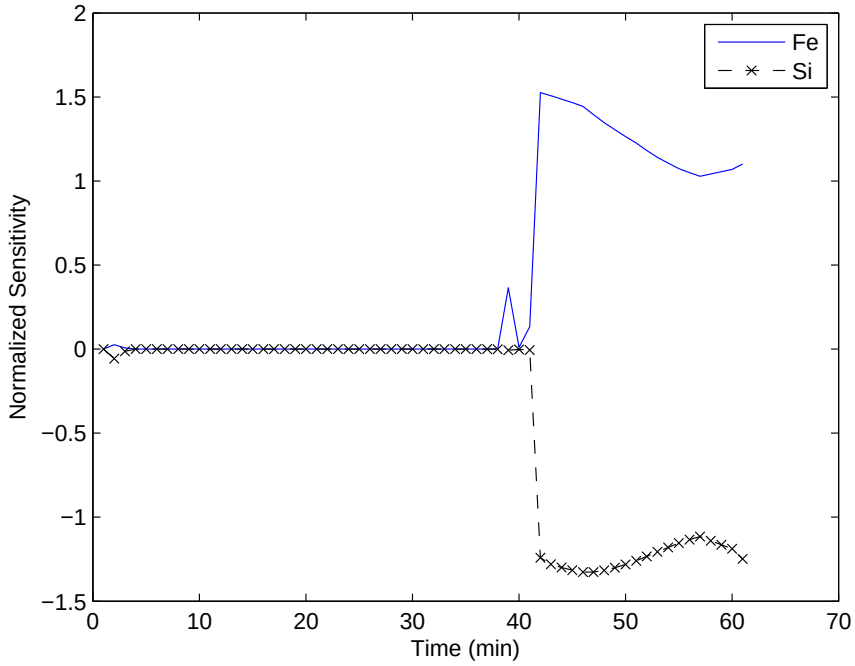

Figure 4.12: Effect of scrap components on FeO slag composition

4.3.3 Effect of scrap composition on zone temperatures and molten metal carbon content

Figure 4.13 shows the sensitivity results for the effect of scrap constituents and fluxes on the EAF zone temperatures and molten metal carbon content. It could be observed that Fe mainly influences the molten metal and scrap temperatures. This should be expected, since Fe is the main constituent in the scrap and the only reaction that occurs during the melting of the scrap is the conversion of iron from a solid state to a molten metal state. Fe also affects the molten metal carbon content through influencing the decarburization rate, which depends on FeO and would also be affected by the amount of carbon initially present in the scrap being charged. Fe also affects the zone temperatures, since it affects the slag foaming through affecting the decarburization rate. It is interesting to see that the rest of the fluxing oxides do not have a strong

effect on the solid scrap and molten metal temperatures; however they influence the gas temperature. This is mainly due to the assumption that the no reactions occur in the molten metal zone and the solid scrap zone except the state of change for iron. On the other hand, oxidation reactions occur in the gas and slag-metal zones and as a result all metals contributing to these reactions would affect the gas temperature. Oil could also be noticed to affect the gas temperature and this due its existence mainly in the gas phase. CaO and dolomite affect the zone temperatures through influencing the slag foaming and as a result the energy efficiency of the system.

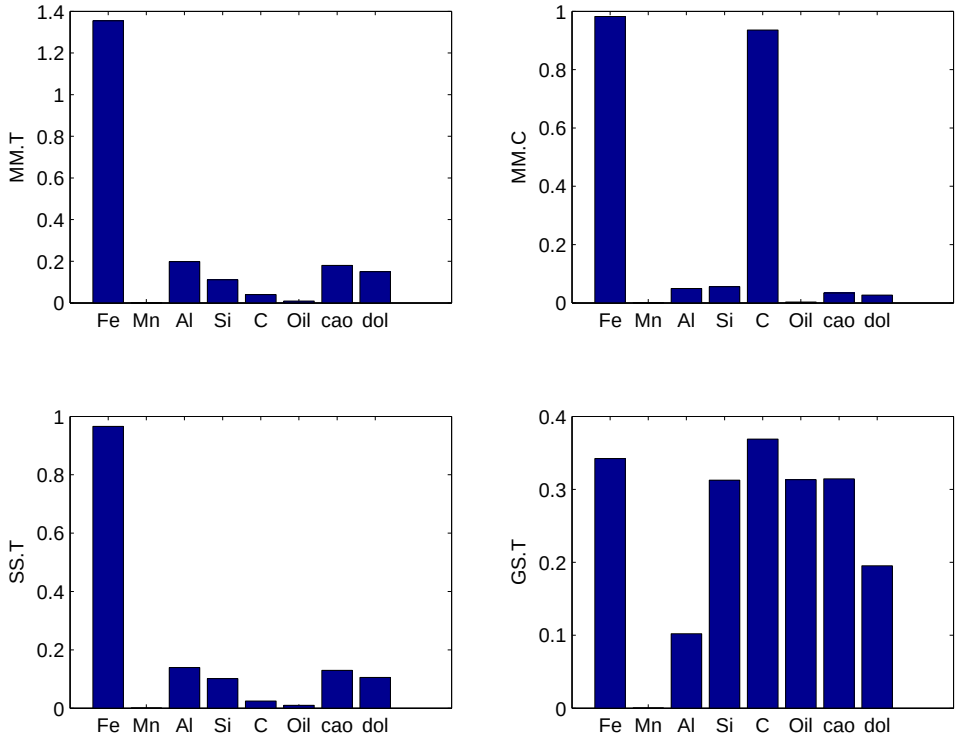

Figure 4.13: Effect of scrap composition on the zones temperatures and molten metal carbon content

The sensitivity profile of solid scrap temperature over time due to Fe is shown in Figure 4.14. The sharp decrease at t=18 min and t=35 min is due to the negligible amount of scrap present in the furnace at these time instants, since all the scrap has melted. The sharp increase at t=27 min represents the time after adding the second

scrap charge in the furnace.

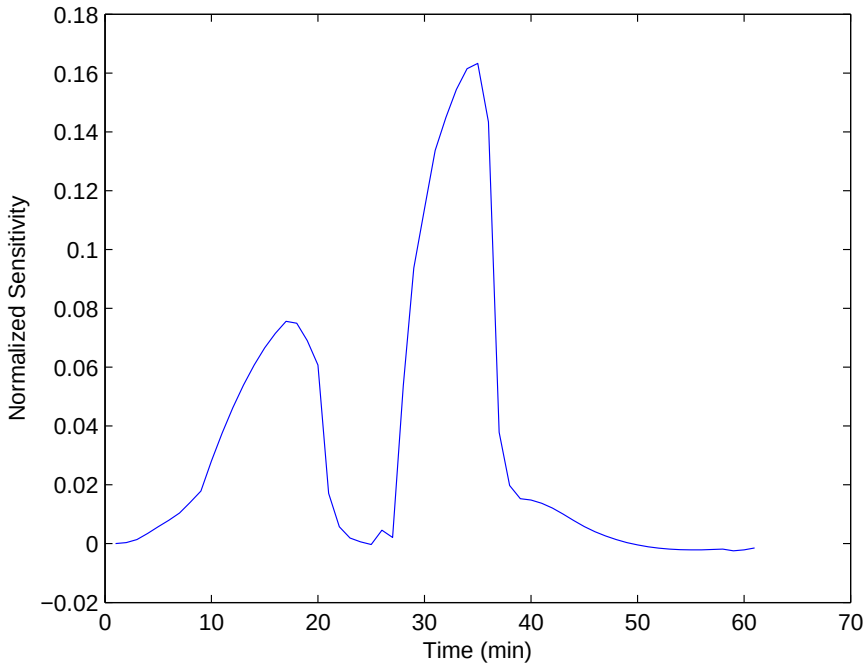

Figure 4.14: Effect of Fe in scrap on the solid scrap zone temperature

The sensitivity change of molten metal carbon with time due to Fe and C is presented in Figure 4.15. It makes sense that C has a positive effect on the amount of carbon present in the molten metal. Fe shows a negative effect on the molten metal carbon content which would be expected as a result of the decarburization reactions that removes carbon from the molten metal. From t=47 min until the end of the batch, it is observed that carbon does not have an effect on the molten metal carbon content and only Fe shows a small interchanging positive and negative effects. This is interesting since this the time when slag foaming occurs intensively due to decarburization which is highly influenced by FeO.

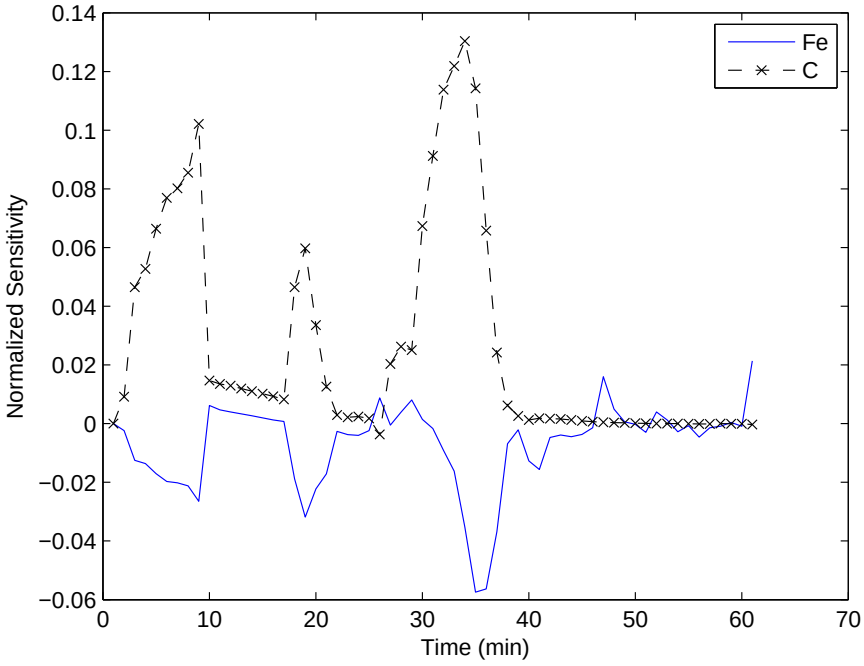

Figure 4.15: Effect of scrap components on the molten metal carbon content

The overall effect of the scrap and flux composition is shown in Figure 4.16, which summarizes the performance that was discussed in detail in the previous subsections. It can be noticed that manganese has the least effect on the EAF. Conversely, Fe has the highest influence on the EAF operation, followed by Si, CaO, dolomite and Al. This is consistent with the literature (Pretorius and Carlisle [1998]), in which Fe, Si, Al and lime have a great effect on the slag chemistry.

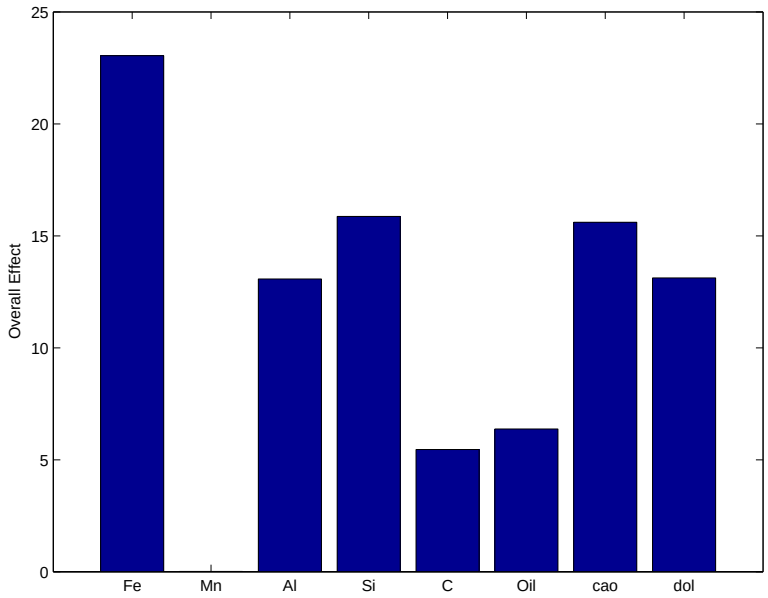

Figure 4.16: Overall effect of scrap composition on the EAF operation

4.4 Dynamic Optimization

This section will focus on finding the optimal operation of the furnace based on an economic objective function. Such optimal operation has the potential for generating significant savings in the steel industry. Some case studies will be investigated and the performance obtained will be discussed.

4.4.1 Formulation

An economic objective function is used in which the total profit (Z) of the process is maximized. The objective function is shown in the equation below.

$$\begin{aligned} Z =& c_0 M_{steel}(t_f) - c_1 \int_0^{t_f} P dt - c_2 \int_0^{t_f} (F_{O_2,burner} + F_{O_2,lance}) dt - c_3 \int_0^{t_f} F_{CH_4,burner} dt \\ & - c_4 \int_0^{t_f} F_{C,inj} dt - c_5 \int_0^{t_f} F_{C,charge} dt - c_6 \int_0^{t_f} F_{flux} dt - c_7 \int_0^{t_f} F_{scrap} dt \end{aligned} \tag{4.10}$$

The first term in the objective function represents the revenue of the process which is proportional to the amount of molten steel produced (M_{steel}) and the rest of the terms represent the costs of materials used during the operation of the furnace. P is the active power, $F_{O_2,burner}$ is the flow of oxygen from the burners, $F_{O_2,lance}$ is the oxygen being lanced, $F_{CH_4,burner}$ is the natural gas from the burners, $F_{C,inj}$ is the carbon being lanced, $F_{C,charge}$ is the charged carbon, F_{flux} is the addition of lime/dolomite, F_{scrap} represents the addition of second charge and t_f is the final time of the heat. Different types of constraints were enforced such as the model equations, input constraints, path constraints and end-point constraints, as shown below.

Model equations:

$$h(\dot{x}(t), x(t), u(t), y(t), t) = 0 \tag{4.11}$$

Input Constraints:

$$P_i^{min}(t) \leqslant P_i(t) \leqslant P_i^{max}(t) \tag{4.12}$$

$$F_i^{min}(t) \leqslant F_i(t) \leqslant F_i^{max}(t) \tag{4.13}$$

End-point Constraints:

$$m_{solid}(t_f) \leqslant \epsilon \tag{4.14}$$

$$y_c(t_f) \leqslant Y_c^{max} \tag{4.15}$$

Path Constraints:

$$T_{wall} \leqslant T^{max} \tag{4.16}$$

$$V_{steel} \leqslant V_{furnace} \tag{4.17}$$

The optimization problem was solved using a sequential approach in which gOPT/gPROMS was used to solve the problem. The control variables were discretized using a one minute sample time with piecewise constant functions. The control input trajectories were constrained to within 10% of the plant nominal values to ensure reliable trajectories. The batch duration is fixed and the state trajectories are continuous variables. The computation time for optimization was between 8 to 14 CPU minutes using a quad-core i7-intel 3.5 GHz processor.

4.4.2 Case Studies

Three case studies were investigated in which the price of electricity, methane and oxygen were varied to see how the optimizer would perform in finding the trade-off between chemical and electrical energy. Initially the nominal operation of the plant is optimized and is considered as an optimized base case to which the different scenarios will be compared.

Scenario 1: Increasing the price of electricity to 0.35$/kWh.
Scenario2: Decreasing the price of electricity 0.015$/kWh.
Scenario3: Increasing the price of chemicals (methane and oxygen) by a factor of 1.5.

It is expected that as the price of electricity increases, the optimizer would use more chemical energy to melt the scrap and use less electrical energy. On the other hand, if the price of chemicals increases or the price of electricity decreases, the optimizer is expected to use more electrical energy and less chemical energy in order to increase the profit from the process.

4.4.3 Results

The results are shown in Figures 4.17-4.21. In the power arc profile it could be noticed that the optimizer uses more power when the electricity price is low followed by when the chemicals price is high and uses the least amount of electrical energy when the electricity price is high. This is shown in Figure 4.17 below.

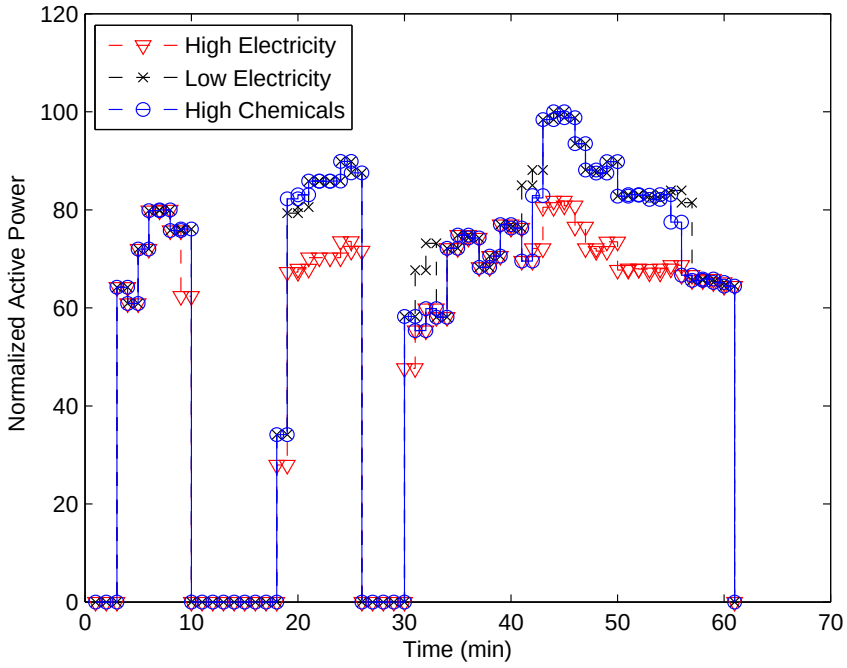

Figure 4.17: Active Power Optimized Trajectories

Looking at the methane profile, it is observed that more methane is injected through the burners when the electricity price is high, and less methane is used when the electricity price is low or the chemicals price is high. It is interesting to observe, that the optimizer managed to capture the effect of preheating which can be seen in Figure 4.18. More methane is used at the time when the first scrap basket is charged. This is the period when the heat transfer between the gas zone and the scrap zone is highly efficient.

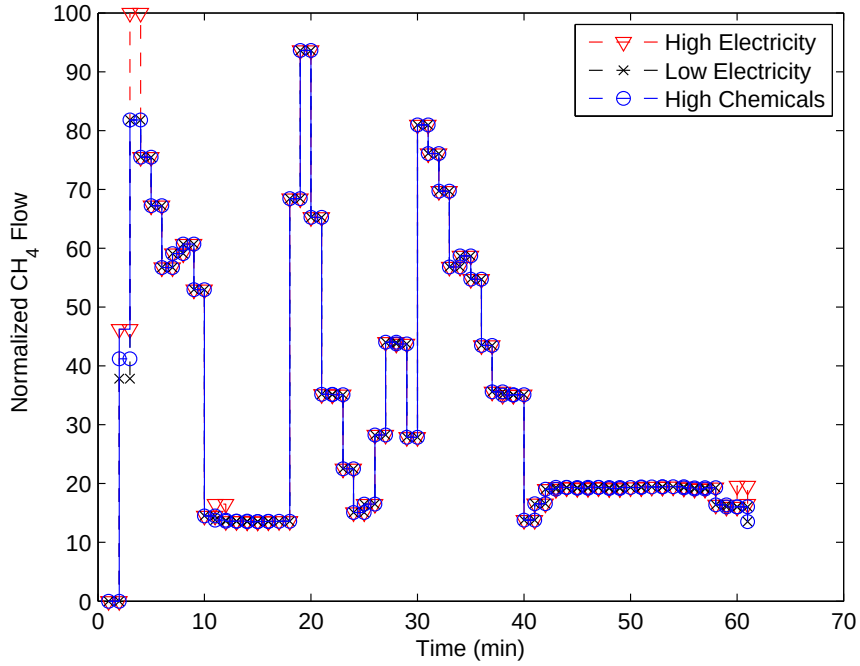

Figure 4.18: Methane Optimized Trajectories

Finally, the flow of oxygen from the three jetboxes as shown in Figures 4.19-4.21 shows similar performance. The highest flow of oxygen occurs when the electricity price is high and less oxygen is used when the electricity price is low followed by when the chemicals price is high. As shown in the results, the change in the control profiles is not highly significant, and this is mainly due to constraining the control input trajectories to within 10% of the nominal operation of the plant. Therefore, the optimizer is constrained to adjust the control inputs only within this range. This was meant to ensure reliable estimates. Through further feedback from the plant, some of the constraints could be relaxed. Table 4.4 shows a summary of the results for the three scenarios, where the total usage of each component is represented for each case.

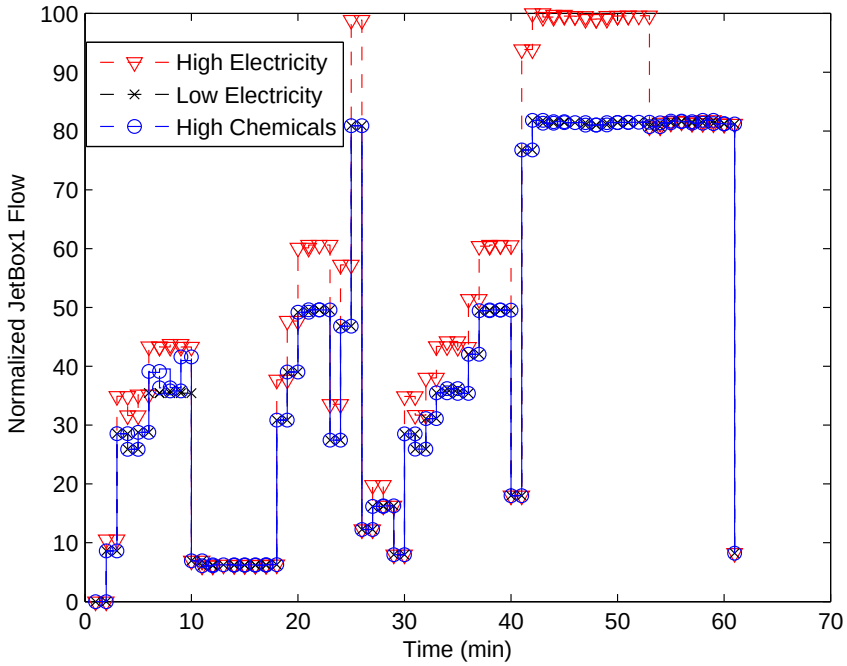

Figure 4.19: JetBox1 Optimized Trajectory

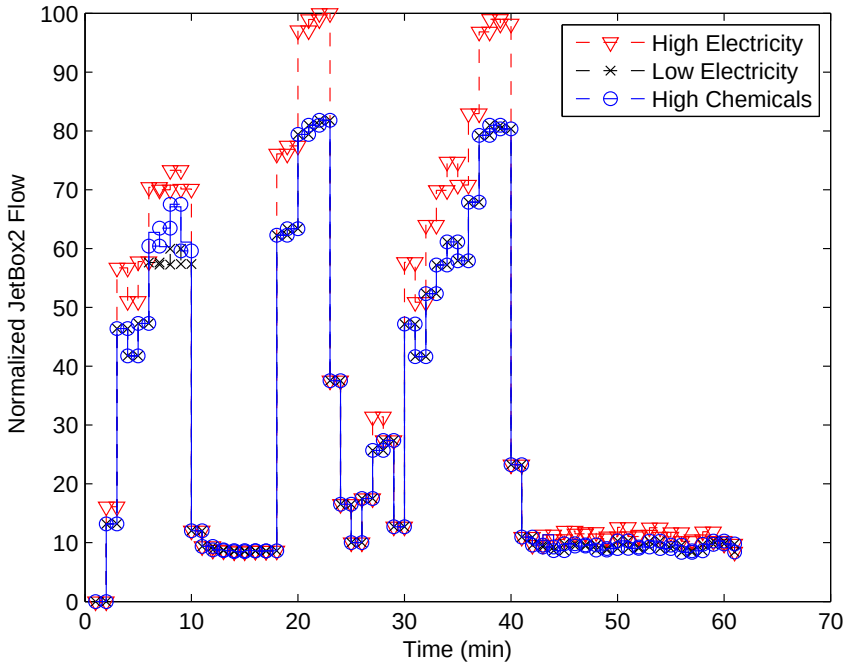

Figure 4.20: JetBox2 Optimized Trajectory

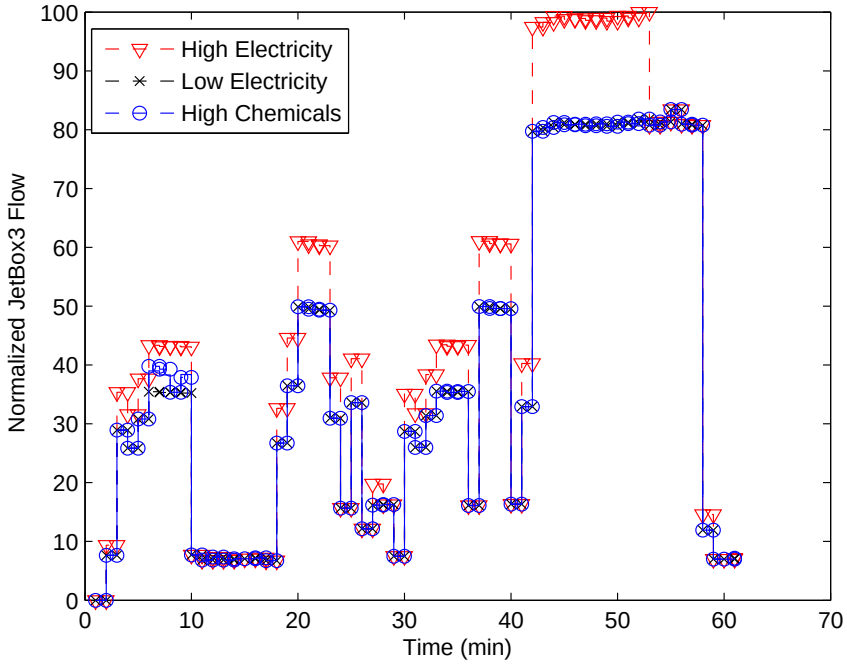

Figure 4.21: JetBox3 Optimized Trajectory

Table 4.4: Optimization summary for the 3 scenarios

Batch	**Base**	**Base Optimized**	**High Electricity**	**Low Electricity**	**High Chemicals**
Active Power$(MW)[\int P]$	48.32	49.59	44.6	50.47	49.59
Methane Flow$(m^3/h)[\int CH_4]$	459.51	415.26	420.81	413.56	414.24
Oxygen Flow$(m^3/h)[\int O_2]$	2493.74	2257.46	2623.24	2244.37	2256.33

Chapter 5

State Estimation

The intent of this chapter is to show how the internal states of the EAF system could be estimated using a state observer. This is required for real-time applications which require state knowledge.

The motivation behind state estimation in EAFs is the limited number of measurements it involves and most of the measurements are not the states themselves. The EAF process is a highly energy intensive process and high fluctuations occur during the batch cycle, due to additions and removal of materials to and from the furnace. The ability to estimate most of the states accurately, would enable the operator to implement effective control and optimization strategies during the batch or within a batch-to-batch framework. Such strategies could potentially save significant amount of money for the steel sector and could enhance sustainable operability in terms of emissions control. In this work, a novel application of a constrained multi-rate extended Kalman filter (EKF) on the EAF process is introduced and implemented.

5.1 State Estimation

5.1.1 Kalman Filter

The Kalman filter determines estimates of the states of a process that is governed by a linear model and an observation model as shown in the equations below for a discrete-time framework:

$$x_k = Ax_{k-1} + Bu_{k-1} + w_{k-1} \tag{5.1}$$

$$y_k = Hx_k + v_k \tag{5.2}$$

w_{k-1} and v_k are random variables that represent the process and measurement noise respectively. These random variables are white noise (independent of each other) and have normal probability distributions $w \in N \sim (0, Q)$, and $v \in N \sim (0, R)$. Q and R represent the covariance of the process and measurement noise respectively. The A matrix relates the state at the current time step (k) to the previous time step ($k-1$).

The Kalman filter equations are given below (Simon [2006]):

$$e_k^- \equiv x_k - \hat{x}_k^- \tag{5.3}$$

$$e_k^+ \equiv x_k - \hat{x}_k^+ \tag{5.4}$$

$$P_k^- = E[e_k^- e_k^{-T}] \tag{5.5}$$

$$P_k^+ = E[e_k^+ e_k^{+T}] \tag{5.6}$$

$$\hat{x}_k^+ = \hat{x}_k^- + K_k(y_k - H\hat{x}_k^-) \tag{5.7}$$

$$\frac{\partial \mathrm{tr}(P_k^+)}{\partial K_k} = 0 \tag{5.8}$$

$$K_k = P_k^- H^T (H P_k^- H^T + R_k)^{-1} \tag{5.9}$$

The *a priori* estimate indicated by a (-ve superscript) $\hat{x}^-$ shows the prediction of the state given knowledge of the process prior to time $(k-1)$ (alternative notation is $\hat{x}(k|k\text{-}1)$). The *a posteriori* estimate indicated by a (+ve superscript) $(\hat{x}_k^+)$ shows the estimated state at time k, when measurement z was taken (alternative notation $\hat{x}\ (k|k)$). The error (e_k) indicates the residual between the predicted estimate and the real value of the process. The aim of the Kalman filter is to find an equation that computes the *a posteriori* estimate $(\hat{x}_k^+\ )$ as a linear combination of the *a priori* estimate $(\hat{x}_k^-)$ and weighted difference between the measurement prediction and the actual measurement $(y_k - H\hat{x}_k^-)$. The Kalman gain (K) is the decision variable for minimizing the trace of the *a posteriori* estimate covariance as shown in equations (5.8) to (5.9).

5.1.2 Extended Kalman Filter (EKF)

The Kalman filter (KF) was developed for linear systems, which do not apply to nonlinear systems represented by:

$$x_k = f(x_{k-1}, u_{k-1}) + w_{k-1} \tag{5.10}$$

$$y_k = g(x_k) + v_k \tag{5.11}$$

The extended Kalman filter (EKF) is a nonlinear version of the KF, in which linearization about the current state is applied, as shown in the equations below (Simon [2006]):

$$\hat{x}_k^- = f(\hat{x}_{k-1}^+, u_{k-1}) \tag{5.12}$$

$$A_{k-1} = \frac{\partial f}{\partial x}|_{\hat{x}^+_{k-1}, u_{k-1}} \tag{5.13}$$

$$H_k = \frac{\partial g}{\partial x}|_{\hat{x}^-_k} \tag{5.14}$$

This is the main step that differentiates the Kalman filter from the extended Kalman filter. The nonlinear model is used to provide an *a priori* estimate, while the linearized model would be used to give an *a posteriori* estimate as in the case of the KF. The EKF is widely used in nonlinear state estimation, since its implementation is straightforward.

The EAF model is nonlinear and therefore this work will focus on the extended Kalman filter (EKF) as a state estimator. The algorithm for implementing the extended Kalman filter is given below, which consists of state model, observation model, prediction stage and an update stage (Simon [2006]).

State Model:

$$\frac{dx}{dt} = Ax + Bu + w \tag{5.15}$$

Observation Model:

$$z = Hx + Du + v \tag{5.16}$$

Prediction Stage:

$$\hat{x}^-_{k+1} = f(\hat{x}^+_k, u_k) \tag{5.17}$$

$$P^-_{k+1} = A_k P^+_k A^T_k + Q_k \tag{5.18}$$

Update Stage:

$$\tilde{y}_{k+1} = z_{k+1} - H_{k+1}\hat{x}^-_{k+1} \tag{5.19}$$

$$S_{k+1} = H_{k+1} P^-_{k+1} H^T_{k+1} + R_{k+1} \tag{5.20}$$

$$K_{k+1} = P^-_{k+1} H^T_{k+1} S^{-1}_{k+1} \tag{5.21}$$

$$\hat{x}^+_{k+1} = \hat{x}^-_{k+1} + K_{k+1} \tilde{y}_{k+1} \tag{5.22}$$

$$P^+_{k+1} = (I - K_{k+1} H_{k+1}) P^-_{k+1} \tag{5.23}$$

The confidence in our initial guesses, model and instrumentation are represented by P^+_0, Q and R respectively. P^+_0, Q and R are typically treated as tuning parameters, and generally have great influence on the EKF performance. Tuning those covariance matrices is challenging and different methods were proposed in the literature. Lima and Rawlings [2011] used the linear time-varying auto-covariance least squares (LTV-ALS) method to tune the noise matrices and obtain their statistics. On the other hand, Prasad *et al.* [2002] used trial and error to determine those matrices for their polymerization reactor. For simplicity, the tuning parameters P^+_0, Q and R in this work were adjusted through trial and error to achieve the satisfactory performance for the EKF. A common mistake that is often made is to choose a high Q value to obtain good convergence properties of the filter. Through choosing a high Q, this would actually mean that the model is useless and is disregarded and all the weight lies towards the measurements with a covariance R (Kozub and MacGregor [1992]). Instead of doing this, Kozub and MacGregor [1992] proposed the incorporation of stochastic disturbances which will be discussed in Section 5.2.5.

5.1.3 States

The EAF model consists of 40 differential states. While transforming the DAE model to ODE state space model, gLinearize in gPROMS finds the minimal subspace of the states that explains the relation between the inputs and the outputs (Process Systems Enterprise Ltd. [2004]). 10 states were neglected by gPROMS and after investigating

those states, it was found that they do not have any effect on the model. 9 of those states are the metal oxides in the molten metal and based on the assumption that no reactions occur in the molten metal, no oxides are formed in this zone. The other state is nitrogen in the slag-metal zone which is assumed to be constant and negligible through the duration of the batch. These states are initialized at zero and remain at this value until the end of the batch.

The 30 differential states that are considered for state estimation are shown below according to their corresponding EAF zone:

Gas Zone: The gas zone consists of 8 states, which are the elemental moles of carbon (GS.C), oxygen (GS.O), hydrogen (GS.H) and nitrogen (GS.N). It also includes the moles of volatile component (GS.Noilgas) and energy hold-up (GS.E). Beside those states formerly mentioned, two more states are included in the gas zone which represents the temperature of the roof (RD.T1) and the walls (RD.T2) of the furnace.

Slag-Metal Interaction Zone: The slag-metal zone consists of 12 states, which are the elemental moles of carbon (SM.C), oxygen (SM.O), iron (SM.Fe), manganese (SM.Mn), magnesium (SM.Mg), silicon (SM.Si) and aluminum (SM.Al). The other 5 states represent the moles of calcium oxide (SM.CaO), mass of calcium oxide floating on the slag layer ($SM.m_{CaO,float}$), mass of carbon floating on top of the slag layer ($SM.m_{C,float}$), mass of dolomite floating on slag layer ($SM.m_{dol,float}$) and energy hold-up (SM.E).

Molten Metal Zone: The molten metal zone contains 8 states, which are the molar amount of carbon (MM.C), oxygen (MM.O), iron (MM.Fe), manganese (MM.Mn), magnesium (MM.Mg), silicon (MM.Si) and aluminum (MM.Al). The last state is the molten metal temperature (MM.T).

Solid Scrap Zone: The solid zone contains 2 states, which are the mass of solid scrap (SS.mss) and the temperature of the solid scrap (SS.T).

5.1.4 Measurement Structure

In the EAF process two types of measurements exist; continuous measurements and discrete-time measurements. The continuous measurements are the offgas compositions, specifically the concentration of carbon monoxide (CO), carbon dioxide (CO_2), oxygen (O_2) and hydrogen (H_2), beside the roof and walls temperatures. The sample time for these measurements is 1 min. On the other hand, discrete measurements are the molten metal temperature, composition of carbon in molten metal and slag composition specifically the composition of iron II oxide (FeO), aluminum oxide (Al_2O_3), silicon dioxide (SiO_2), magnesium oxide (MgO) and calcium oxide (CaO). Typically only one sample is taken to measure the slag composition and two samples for the molten metal temperature and carbon content in molten metal.

5.2 Implementing a constrained-multirate EKF

5.2.1 Linearization

The EAF model developed in Chapter 3 is a nonlinear DAE model and in order to implement an extended Kalman filter, the DAE model is converted to a linear ODE state space model. As discussed in Section 5.1.2, the main difference between the KF and EKF is the linearization using the current estimate. The gPROMS linearize function tool was used to perform this linearization at every time step to convert the DAE system to an ODE state space model of the form (Process Systems Enterprise Ltd. [2004]):

$$\begin{aligned} \dot{\bar{x}} &= A\bar{x} + B\bar{u} \\ \bar{y} &= C\bar{x} + D\bar{u} \end{aligned} \tag{5.24}$$

The linearize function tool requires specifying the input and output variables. The input variables are carbon flux addition, carbon lance, oxygen lance, amount of water sprayed, natural gas addition, arc power, oil addition, lime, dolomite and scrap additions. The outputs at each time step depend on the measurement structure as described in Section 5.1.4. A DAE model is represented by the following equation system,

$$\begin{gathered} F(\dot{x}(t), x(t), u(t),\ z(t), t) = \dot{x} - f(x(t), u(t), z(t), t) = 0 \\ g(x(t), u(t), z(t), t) = 0 \end{gathered} \tag{5.25}$$

$$y(t_k) = h(x(t_k)) \tag{5.26}$$

in which x and z represent the differential state and algebraic variables respectively, and u represents the input variables. $\dot{x}$ is the set of derivatives of $x(t)$ with respect to time t. Considering a reference trajectory point $(x^*(t), \dot{x}^*(t), z^*(t), u^*(t))$ that satisfies equation (5.25), linearization would take place at this point as shown in the equations below:

$$F_{\dot{x}}\dot{\bar{x}} + F_x\bar{x} + F_u\bar{u} + F_z\bar{z} = 0 \tag{5.27}$$

$$g_x\bar{x} + g_u\bar{u} + g_z\bar{z} = 0 \tag{5.28}$$

in which $F_{\dot{x}}$, F_x, F_u, F_z, g_x, g_u and g_z represent $\frac{\partial F}{\partial \dot{x}}$, $\frac{\partial F}{\partial x}$, $\frac{\partial F}{\partial u}$, $\frac{\partial F}{\partial z}$, $\frac{\partial g}{\partial x}$, $\frac{\partial g}{\partial u}$ and $\frac{\partial g}{\partial z}$ respectively. All the partial derivatives are calculated about the reference trajectory points in which $\dot{\bar{x}}$, $\bar{x}$, $\bar{u}$ and $\bar{z}$ represent the deviation of the variables from the reference trajectories. Since the DAE system is of index 1, $\frac{\partial g}{\partial z}$ is non-singular and invertible. The $\bar{z}$ from equation (5.28) is then substituted into equation (5.27). Through linearization, the Jacobian matrices are hence calculated to give the A, B, C and D matrices, as shown in the equations below:

$$A = F_z g_z^{-1} g_x - F_x \tag{5.29}$$

$$B = F_z g_z^{-1} g_u - F_u \tag{5.30}$$

$$C = h_x \tag{5.31}$$

The full linearization derivation is provided in Appendix C.1 (Becerra *et al.* [2001]). The A and C matrices are the crucial ones for this work, since the observability analysis and the EKF implementation depend on those two matrices, as we will see in later sections. The B matrix becomes critical when controllability studies are investigated. The D matrix is usually zero, since in most dynamical systems the inputs do not have a direct influence on the output variable y. The dimension of the C matrix will depend at each time step on the number of measurements available. For the batch system considered in this work, this linearization algorithm is carried out at every time step.

5.2.2 Observability Analysis:

Before implementing a state observer, a detailed observability analysis is required. This is necessary to ensure that we get appropriate performance of the filter. Observability indicates the ability to fully reconstruct the internal states of the system through using the inputs and outputs of the system. Observability tests for nonlinear systems represented a great challenge to researchers and no rule exists for determining the observability of a general nonlinear system, therefore no prior judgments can be made about the EKF performance (Southall *et al.* [1998], Wu *et al.* [2012]). The observability of a nonlinear system generally depends on the inputs applied to the process and on the region of the measured output trajectory (Böhm *et al.* [2008]; Marafioti *et al.* [2009]). In this work, local linear observability is tested using the linearized A and C matrices obtained at every state estimate. One test for observability

is the rank test on the observability matrix. The *Obsv* command in $Matlab^{®}$ could be used to obtain the observability matrix (ϑ), which is calculated as,

$$\vartheta = \begin{bmatrix} C \\ CA \\ CA^2 \\ . \\ . \\ . \\ CA^{n-1} \end{bmatrix} \tag{5.32}$$

The system is fully observable, if for any initial state $x(0)$ and some final time k the initial state can be uniquely determined through the knowledge of the input u_i and output y_i for all i ∈ [0,k] (Simon [2006]) . The system is locally observable when the observability matrix is full rank. The rank could be calculated using $Matlab^{®}$ and the default tolerance (tol) formula in $Matlab^{®}$ is used. The rank would then be the number of singular values that are greater than this tolerance. The syntax of the *obsv* command is shown in Appendix C.2.

Although this test is widely used in literature to obtain the rank test for the observability analysis (eg. Prasad *et al.* [2002]), it has some limitations as well. This test is unique for linear systems, where the A and C matrices do not change with time and when the number of states in the system is small. Some nonlinear systems are ill-conditioned and as a result, when the observability matrix is calculated, a singular matrix could be obtained (MathWorks [2013]) and this could cause numerical issues. Therefore, a similarity transformation (observability staircase form) is often applied to the matrices, which separates the observable modes from the unobservable ones (observability canonical form). The transformation calculations are shown in the equations below.

$$\bar{A} = TAT^T \tag{5.33}$$

$$\bar{C} = CT^T \tag{5.34}$$

$$\bar{A} = \begin{bmatrix} A_{unob} & A_{12} \\ 0 & A_{ob} \end{bmatrix} \tag{5.35}$$

$$\bar{C} = \begin{bmatrix} 0 & C_{ob} \end{bmatrix} \tag{5.36}$$

A and $\bar{A}$ are called similar matrices and they share several properties such as the rank and determinant. The same applies to the C and $\bar{C}$ matrices. The T matrix which is called the similarity transformation matrix (nonsingular) is obtained using QR decomposition (Lima and Rawlings [2011]; Brogan [1991]). The *Obsvf* command in the Control Systems Toolbox of $Matlab^{®}$ could be used to apply the similarity transformation and to extract the observable states (MathWorks [2013]). The eigenvalues of A_{unob} are the unobservable modes and the system is fully observable, when the subspace A_{unob} is empty (Xue and Atherton [2007]). In this work the similarity transformation is applied and the *obsvf* command in $Matlab^{®}$ is used to test the observability of the system based on a tolerance calculated by $Matlab^{®}$. The syntax for this command is shown in Appendix C.2. The outcome of the observability analysis is discussed later in the results section.

5.2.3 Plant and Estimator Models

Two models are used in the state estimation procedure. Both models are built in gPROMS. A model (plant model) comprising 30 states mimics the plant and another model (estimator model) consisting of 30 states is used for the EKF estimator. The plant model provides the measurements to the estimator. The estimator interacts with the estimator model, which provides it with the *a priori* estimates. The estimator uses the measurements from the plant model and updates its states to give the *a*

posteriori states. The *a posteriori* states are then provided to the estimator model where integration occurs and a new *a priori* estimate is calculated. This algorithm is repeated until the end of the batch is reached. Figure 5.1 shows a schematic diagram of the algorithm.

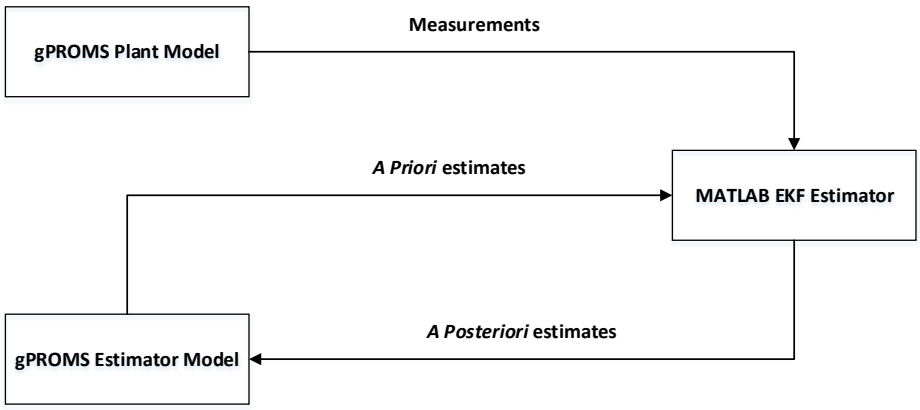

Figure 5.1: The flow between the plant, estimator and estimator model

The EKF is implemented in *Matlab*® and the nonlinear model is used by gPROMS. In order to carry out the state estimation, an interface between gPROMS and *Matlab*® is necessary. The gO:MATLAB tool is used in gPROMS (Process Systems Enterprise Ltd. [2004]). The nonlinear model in gPROMS is used to carry out the integration steps and provide the *a priori* estimates that is exported to *Matlab*® and used by the EKF to obtain the updated estimates (*a posteriori* estimates). Figure 5.2 shows the flow of information between *Matlab*® and gPROMS.

5.2.4 Constrained multi-rate EKF

Due to the fact that different sampling rates occur for the measurements (as discussed in Section 5.1.4), this should be taken into account, while designing the EKF. The

Figure 5.2: Interfacing gPROMS and *Matlab*® using gO:MATLAB tool

algorithm for the EKF will remain the same and the main variable that would change is the dimension of the C matrix which would affect the Kalman gain. Therefore, we will have three EKF versions. EKF1 would be used when only fast measurements represented by the offgas composition and the wall/roof temperatures are available. EKF2 would operate when the molten metal temperature, slag composition and carbon composition are available along with the fast measurements. EKF3 would be used when the molten metal temperature and carbon content are measured along with the fast measurements. Therefore, EKF1, EKF2 and EKF3 would use 6, 13 and 8 measurements respectively. This will affect the local observability of the system, in which some of the states were found to be unobservable at some points along the duration of the batch and observable at others. All the state estimates are stored in a state vector, and therefore no information is lost, while implementing the multi-rate algorithm. Figure 5.3 shows a schematic diagram for the implementation of the multi-rate EKF.

A limitation that could exist, while implementing the EKF, is that the state estimate could be unreliable. For example, the molar flow, concentration and temperatures can not be negative in the real process, and therefore this should be taken care of when implementing the filter. The EKF can drift towards such unreliable regions, especially that the EKF does not have any knowledge regarding the real operation of the process. Therefore, constraints were enforced to ensure that we get reliable state estimates. This is not limited to the sign of the quantities, but also uses industrial insight of

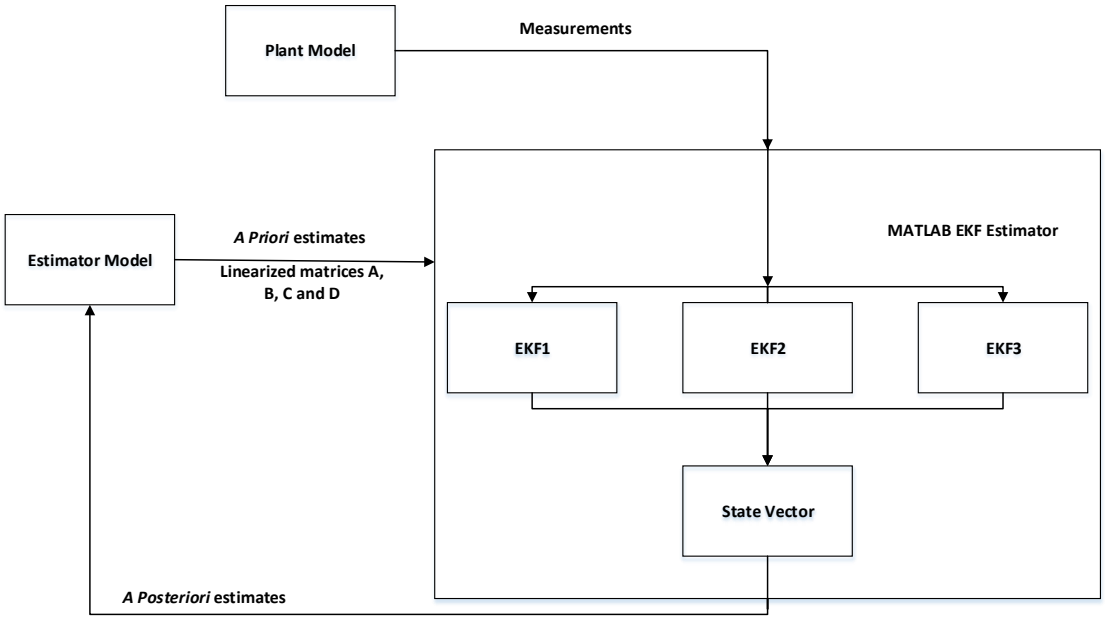

Figure 5.3: Multi-rate EKF implementation diagram

the process to enforce certain limits to make sure that the states are industrially realizable. In this case the unconstrained state estimate $\hat{x}_k^+$ is projected to a new constrained surface. The constrained estimate could be found using the following (Simon [2006]):

$$x_{k\ const}^+ = \arg\min_x (x - \hat{x}_k^+)^T H (x - \hat{x}_k^+) \tag{5.37}$$

$$s.t. \quad Dx \leq d \tag{5.38}$$

This problem is then considered as a quadratic programming problem and an interior point approach was used in $Matlab$®. If H is chosen to be the inverse of the covariance matrix (P^{-1}), this results in a maximum probability estimate of the state subject to the constraints (Simon [2006]). On the other hand, if H is chosen as an identity matrix (I), then we get a least squares estimate of the state subject to the constraints (Simon [2006]). H is chosen as shown in equation (5.41) below, which represents

a symmetrized version of P^{-1}. Although P^{-1} is symmetric in theory, small noise occurring through the estimation may cause the matrix to be non-symmetric in nature (Chong [2012]). This could be rewritten in a standard quadratic programming format as shown in the equations below, where we can see how the H matrix and f vector were chosen.

$$\min_x \frac{1}{2} x^T H x + f^T x \tag{5.39}$$

$$s.t. \;\; x_L \leq x \leq x_U \tag{5.40}$$

$$H = \frac{1}{2}[P^{+-1} + (P^{+-1})^T] \tag{5.41}$$

$$f = -P^{+-1}\hat{x}_k^+ \tag{5.42}$$

5.2.5 State augmentation and disturbance rejection

There is no perfect model that exactly mimics the plant, and therefore we usually have plant-model mismatch in reality. Two types of plant-model mismatch are usually considered, which are a structural mismatch and parametric mismatch. A structural mismatch results due to the inappropriateness of the model to represent the plant behaviour. A parametric mismatch occurs, when the model parameters do not match the plant parameters. Such mismatches could result in poor performance of the EKF and an offset could be obtained in the trajectories. As mentioned before, a common error in the EKF formulation, is neglecting the incorporation of non-stationary disturbance states that would be needed to remove the bias in the state estimates that might result from modeling errors or unknown disturbances occurring in the system (Kozub and MacGregor [1992]). As mentioned in the introduction, Kozub and MacGregor [1992], as well as, Prasad *et al.* [2002] discussed the use of stochastic disturbance states and augmenting those states to the model states. The disturbance states are estimated along with the model states, which add an integral action to the

estimator, in order to eliminate the offset. The true dynamics of the stochastic disturbances are usually unknown and it could be assumed that these disturbances follow a non-stationary random walk behaviour, as represented by the difference equation shown in equation (5.44) (Kozub and MacGregor [1992]). w_k^d is a white noise vector with a $N \sim (0, Q^d)$, which shows the amount of change in the stochastic states between the sampling intervals, and Q^d represents the covariance of the disturbance states model. The augmented system is then calculated as shown in the equations below.

$$x_{k+1} = A_k x_k + A_k^d x_k^d + w_k \tag{5.43}$$

$$x_{k+1}^d = x_k^d + w_k^d \tag{5.44}$$

$$\begin{bmatrix} x_{k+1} \\ x_{k+1}^d \end{bmatrix} = \begin{bmatrix} A_k & A_k^d \\ 0 & I \end{bmatrix} \begin{bmatrix} x_k \\ x_k^d \end{bmatrix} + \begin{bmatrix} w_k \\ w_k^d \end{bmatrix} \tag{5.45}$$

The superscript d refers to stochastic disturbance in this case. The augmented states now include the process states x_k and the disturbance states x_k^d. The disturbance states and their covariances are augmented to the process states and covariance matrices respectively. A_k^d is treated as a tuning parameter to reflect the weights of the disturbances that enter the system. The disturbance estimates may affect the state estimates significantly and are generally necessary to ensure accurate state estimate updates. Choosing which disturbances to incorporate and tuning the parameters (Q^d, P_0^{+d}) for these disturbance states is an art. In this work, the number of disturbances were chosen such that they would never exceed the number of measurements (Prasad *et al.* [2002]).

5.3 Results and Discussion

5.3.1 Observability

Through carrying out local linear observability analysis as discussed in Section 5.2.2, the system was found to be fully observable. The similarity transformation test was used and observability results are shown in Appendix C.2. It could be observed that at some time instants some states were unobservable. These unobservable states would be associated with a Kalman gain of zero and therefore those states would not be updated by the measurements provided at that time instant, and rather would be updated in an open loop fashion (Bageshwar [2008]). The ability to estimate 30 states from 13 measurements could appear strange, but through the knowledge of the EAF operation we could notice how all the states can affect the measurements and how the states affect each other. The stochastic states added were found to be observable as well. Simulation tests and case studies were used to confirm our observability results and to show that the EKF did not diverge as will be shown in the next sections.

5.3.2 Case Study 1

The first case study that will be investigated is the lack of knowledge of the true initial states. The plant model is initialized with the true initial conditions, while the estimator model does not know the exact initial conditions. The extended Kalman filter will be tested against its ability to converge to the true states using the feedback from the measurements provided by the plant. This case study is very critical, since it reflects what happens in the real plant, where the exact initial conditions are always unknown. This case study was performed initially without accounting for stochastic disturbances and the EKF performance was investigated. Then, the process states were augmented by stochastic disturbances to add integral action and the EKF

performance was compared to the base case. In this section, the important states are shown, while the trajectories for the rest of the states are attached in Appendix C.4.

Initial conditions, Constraints and Tuning parameters

The values for the plant's exact initial conditions (x_0), estimator initial conditions (x_0^+), tuning parameters (Q, P_0^+ and R) and constraints on the states are provided in Appendix C.3. The tuning parameters were determined by trial and error, through using insight on the range of variables and through performance analysis of repeated simulations. The constraints were chosen based on two principles. The first principle is to enforce the realizability of the variables by making sure that positive variables do not go negative at some point during the simulation of the batch. The second principle is to enforce industrial realizability through choosing an appropriate upper and lower bounds that is based on the current practice of the plant. The initial condition for the mass of solid scrap mass is supposed to be known to a high degree of accuracy since it is measured by the plant for every batch.

Case Study 1A: Base Case (no stochastic disturbances added)

The performance of the EKF was investigated without adding any disturbance states and the results are represented by Figures 5.4 - 5.7. Some of the states that were discussed in Section 5.3, were represented as mole fractions as shown in Figures 5.4, 5.5 and 5.6. It could be observed that the performance of the EKF is very good in tracking the true states; however, as expected some offset occurred. The only two states where offset was obtained are the mole fraction of aluminum (MM.Al) in the molten metal as shown in Figure 5.6 and the solid scrap temperature (SS.T) as shown in Figure 5.7. Even though the offset for (MM.Al) is in a magnitude of (2×10^{-4}), adding disturbance states could be investigated to see if it will be able to

remove this offset. The same will be applied to the solid scrap temperature (SS.T), where a negligible offset was also obtained. The molten metal temperature estimates, as shown in Figure 5.6, converge to the true states and specifically after the time instant when full measurements are available. However, a gap could be noticed up to time t=44 min and in order to apply MPC control strategies getting more accurate estimates at those time instants would be preferable. The molten metal temperature is important in EAF control applications as it determines the tap time, which is the time when the molten metal is poured out of the furnace for further refining. Stochastic disturbances will be investigated in order to get faster convergence for the molten metal temperature.

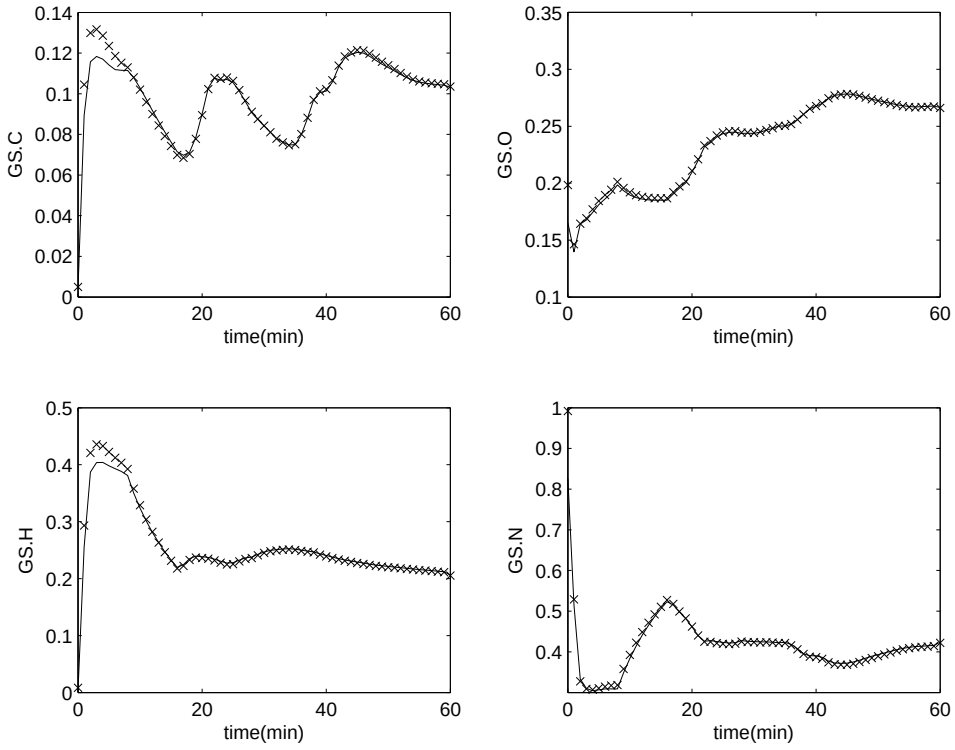

Figure 5.4: Gas zone state profiles for the base case (Case Study 1A) without disturbance state augmentation. (×) represents the estimated states while (–) represents the actual states

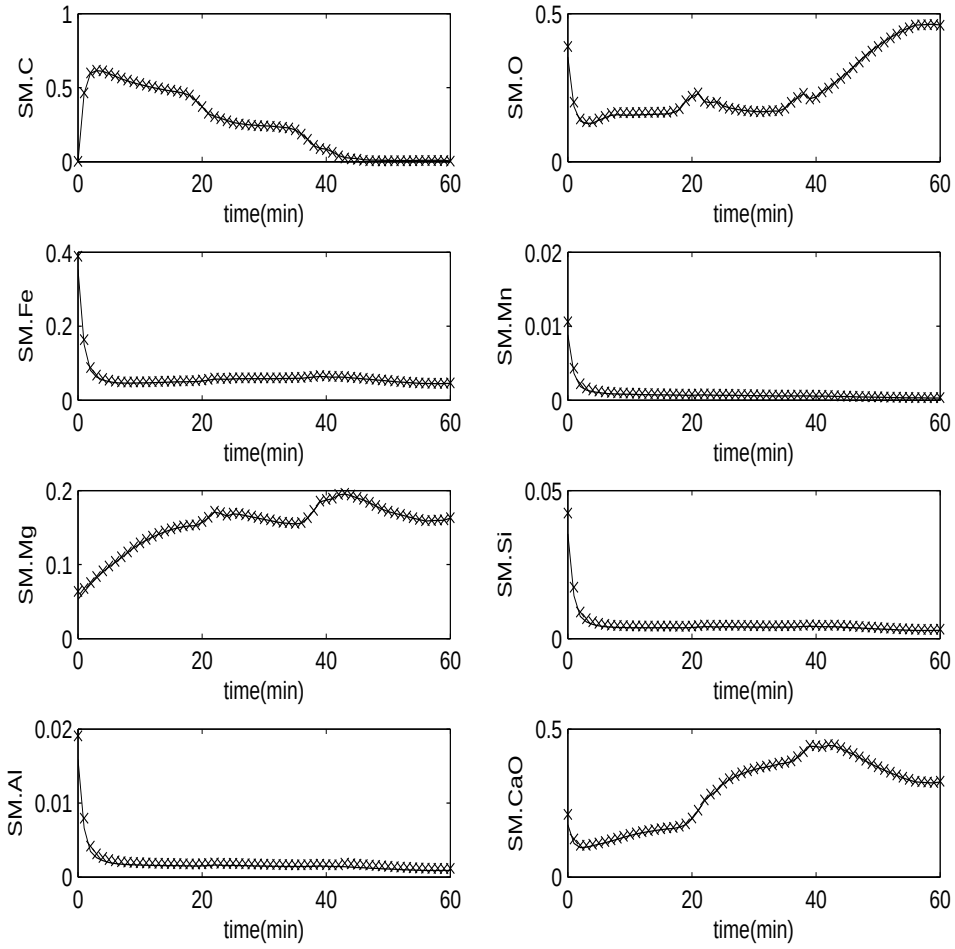

Figure 5.5: Slag zone state profiles for the base case (Case Study 1A) without disturbance state augmentation. (×) represents the estimated states while (–) represents the actual states

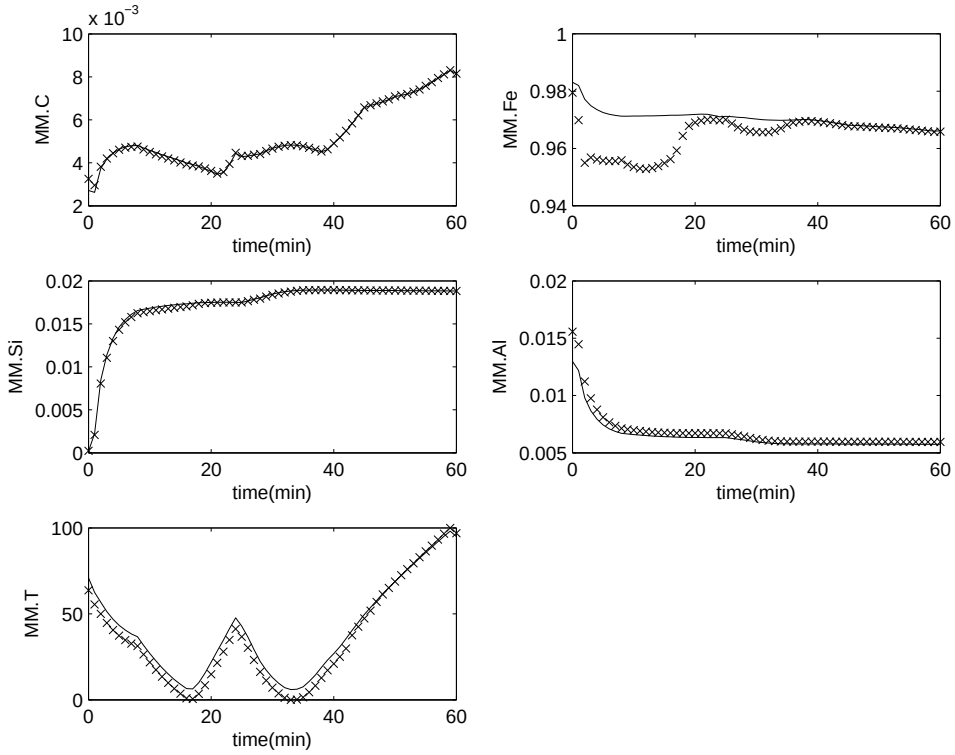

Figure 5.6: Molten metal zone state profiles for the base case (Case Study 1A) without disturbance state augmentation. (×) represents the estimated states while (–) represents the actual states

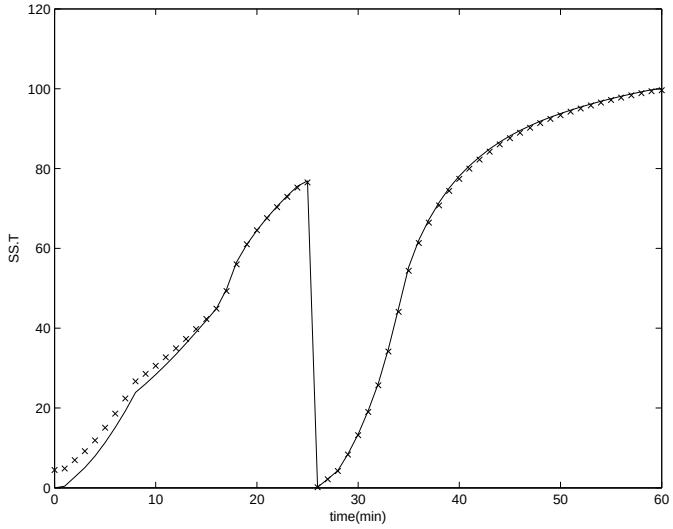

Figure 5.7: Solid zone state profiles for the base case (Case Study 1A) without disturbance state augmentation. (×) represents the estimated states while (–) represents the actual states

Case Study 1B: Augmented Disturbances

Two disturbances were added, which affect the (MM.Al) and (MM.T) directly. The tuning matrix (A_k^d) is provided in Appendix C.3, in addition to the covariance tuning parameters (Q^d and P_0^{+d}) and initial disturbance state estimates (x_0^{+d}). It could be noticed from Figures 5.8-5.11, that the augmented disturbances were able to remove the offset from the SS.T (as shown in Figure 5.8) and MM.Al trajectories (as shown in Figure 5.11). Better estimates were obtained for the molten metal temperature (MM.T) compared to the base case (Figure 5.11) which makes it more suitable for MPC control algorithms. The only issue with the molten metal temperature profile is the occurrence of an offset between time t=58 min and t=60 min.

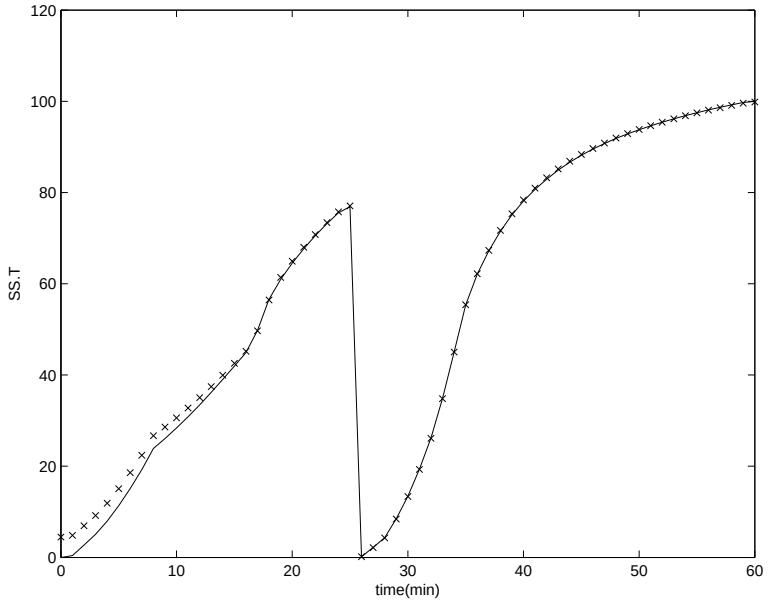

Figure 5.8: Solid zone state profiles for Case Study 1B with disturbance state augmentation. (×) represents the estimated states while (–) represents the actual states

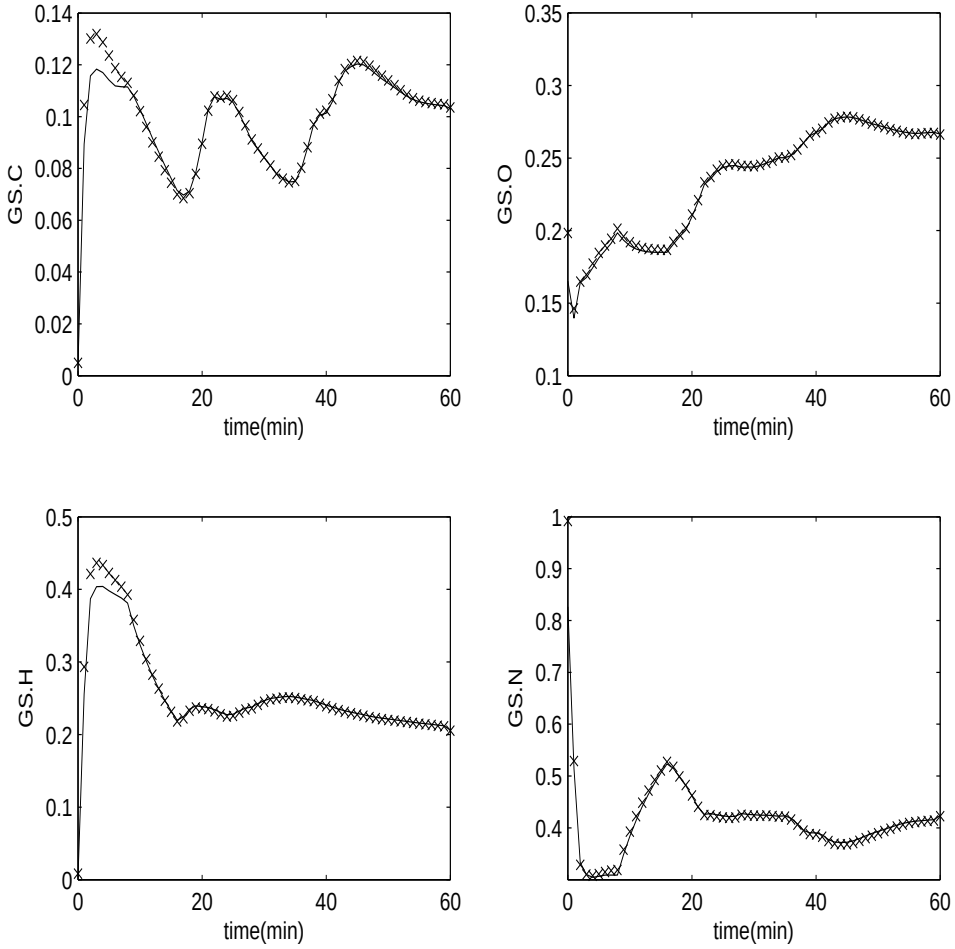

Figure 5.9: Gas zone state profiles for Case Study 1B with disturbance state augmentation. (×) represents the estimated states while (–) represents the actual states

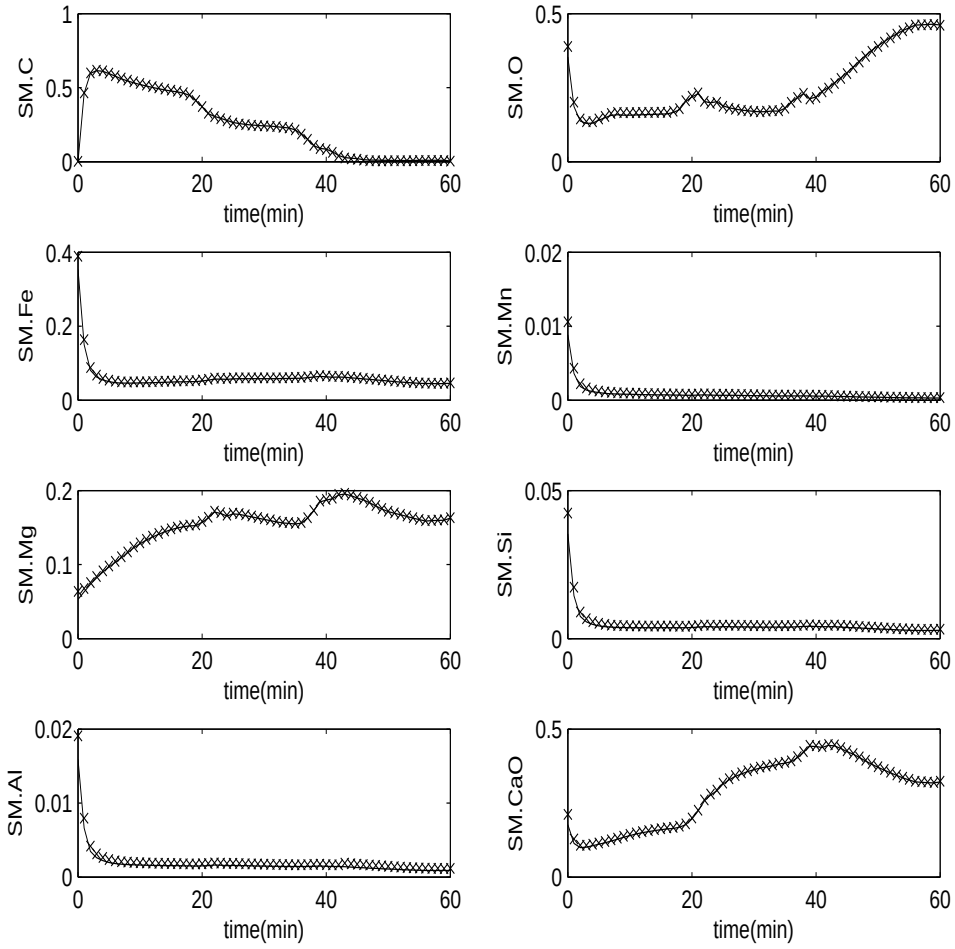

Figure 5.10: Slag zone state profiles for Case Study 1B with disturbance state augmentation. (×) represents the estimated states while (–) represents the actual states

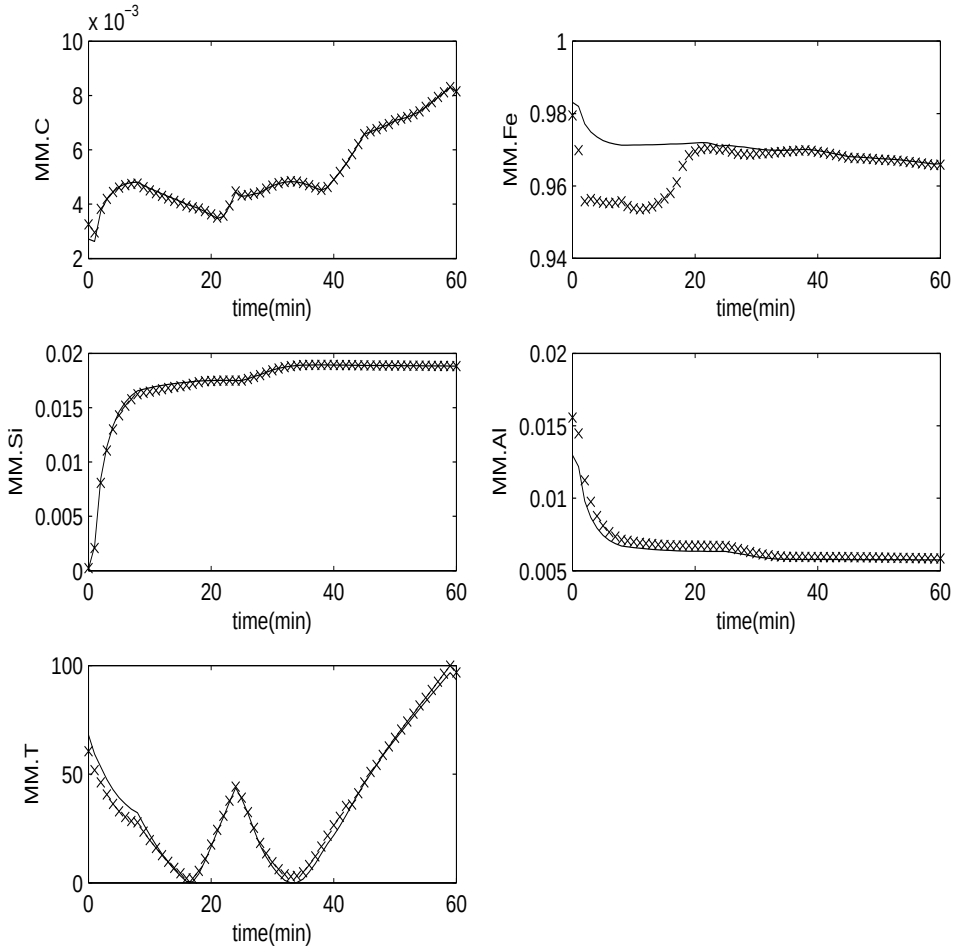

Figure 5.11: Molten metal zone state profiles for Case Study 1B with disturbance state augmentation. (×) represents the estimated states while (–) represents the actual states

5.3.3 Frequent molten metal temperature measurements

A hypothetical case study was investigated to see the effect of having more frequent molten metal temperature measurements on the estimation of the EAF states and specifically the molten metal temperature. This was mainly investigated on Case Study 1. Three extra molten metal temperature measurements were obtained at time t= 25, 56 and 59 minutes. Those time instants were chosen such all the scrap in the furnace has melted and a pool of molten bath has been formed to ensure its feasibility. The molten metal temperature profile is shown below and it is compared to Case Study 1A (as shown in Figure 5.12a) and Case Study 1B (as shown in Figure 5.12b).

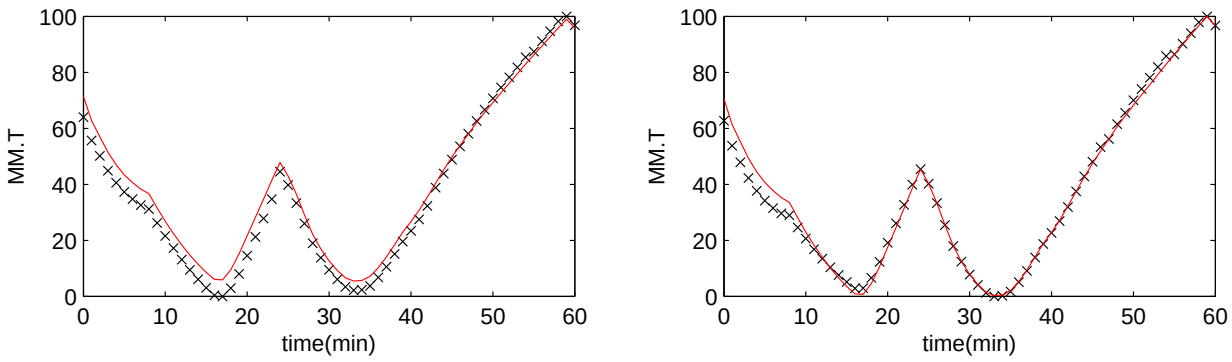

(a) Molten metal temperature without stochastic disturbances

(b) Molten metal temperature with stochastic disturbances

Figure 5.12: Molten metal temperature trajectories with frequent molten metal temperature measurements

It can be observed in Figure 5.12a that better predictions are obtained compared to Case Study 1A, and specifically at t= 25 min which is the time instant after a molten metal temperature becomes available. This shows that the more frequent measurements available, the better the estimation for the molten metal temperature will be. Figure 5.12b shows the molten metal trajectory when stochastic disturbances are included and more frequent temperature measurements are available. Comparing

this trajectory to Case Study 2B, it could be observed that the offset in the molten metal temperature profile has been eliminated and very good performance was obtained. The rest of the trajectories converged similar to Case Study 1A and Case Study 1B (Appendix C.4); however, the solid scrap temperature (SS.T) showed better convergence in the absence of disturbance augmentation compared to Case Study 1A.

5.3.4 Case Study 2

The previous case study focused on state estimation using a model that lacks the knowledge of the true initial states of the process. In this case study, a parametric mismatch is going to be applied and the EKF performance will be analyzed, with and without the addition of augmented disturbances. Three parameters were chosen to be mismatched with the plant, which are the power factor (k_p), the base mass transfer coefficient (k_m) and the oxygen injection factor in the slag-metal zone ($Bias_{O2}SM^*$). The reader is referred to Table 4.1 which indicates the model equations in which the parameters appear. Those parameters were chosen based on sensitivity results and due to the fact that they affect a range of different states from all zones. Also the initial conditions are not known by the model as in Case Study 1. Frequent temperature measurements similar to that discussed in Section 5.3.3 will be used in this case as it provided the preferable performance.

Initial conditions, Constraints and Tuning parameters

The initial conditions provided to the estimator model are the same as those in Case Study 1, and the same applies for the constraints. The tuning parameters for the process states are given in Appendix C.3.

Case study 2A: Base Case (no stochastic disturbances added)

After inducing a parameter mismatch between the estimator model and the plant model, the EKF was initially implemented without the incorporation of state disturbances, as a base case. Through inspection of the estimated trajectories by the EKF in Figures 5.13-5.16, it could be observed that the EKF performance is worse than the base scenario in Case Study 1A. This is expected due to the errors added to the model in terms of parametric plant-model mismatch, which resulted in an offset in several trajectories which are the (GS.C) as shown in Figure 5.13; (SM.O) as shown in Figure 5.15; (SS.T) as shown in Figure 5.16; (MM.C), (MM.Al) and (MM.T) as shown in Figure 5.14. This shows that the EKF would fail to converge, if such disturbances occurred without considering stochastic disturbances incorporation. Therefore, augmenting some stochastic disturbances would be essential to try to eliminate some of these offsets in the estimated trajectories.

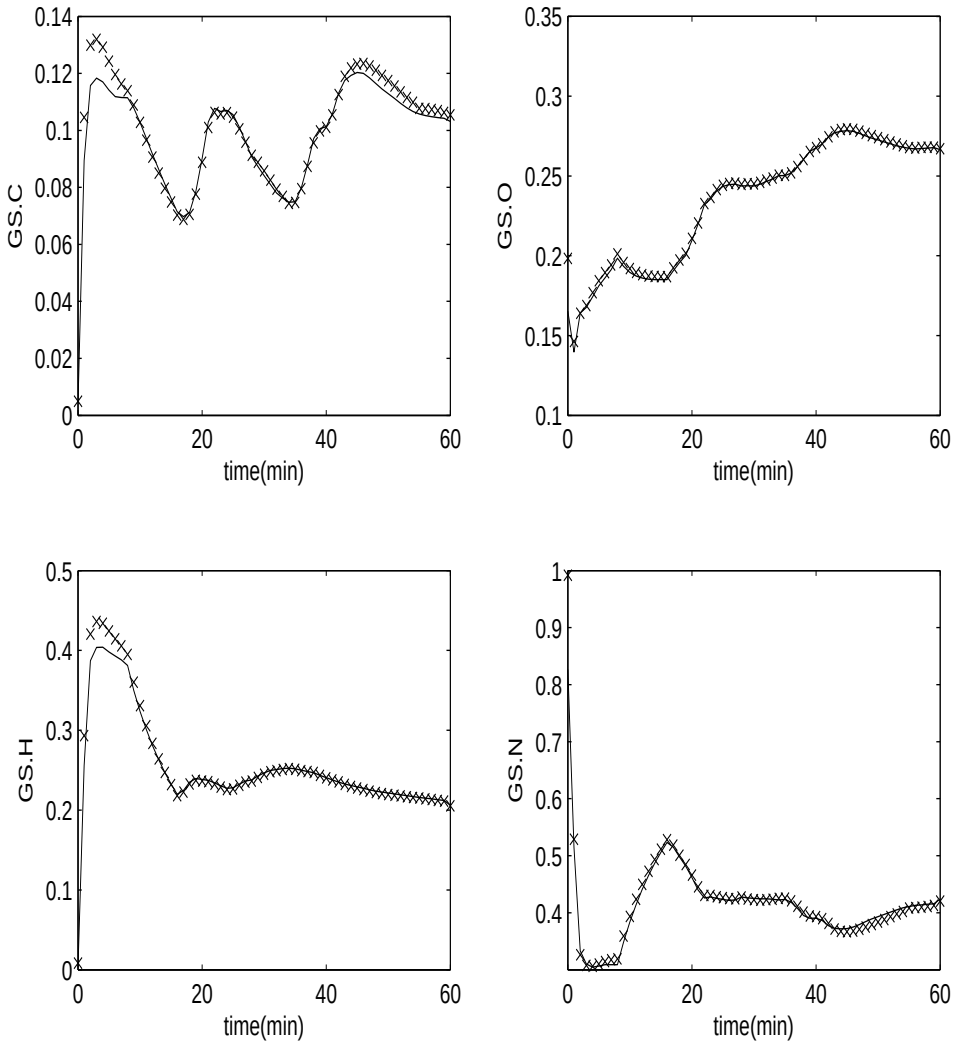

Figure 5.13: Gas zone state profiles for the Case Study 2A without disturbance state augmentation. (×) represents the estimated states while (–) represents the actual states

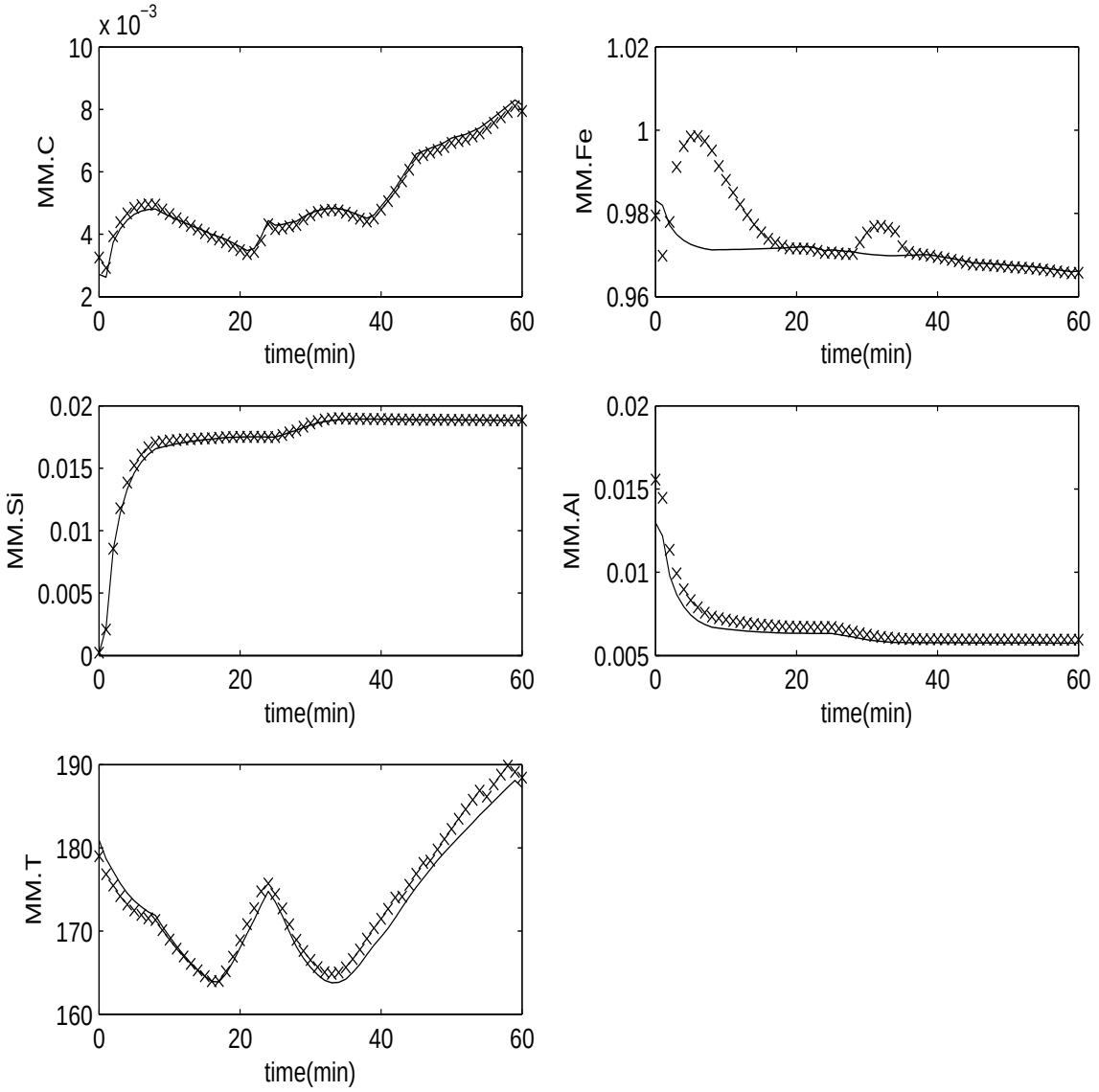

Figure 5.14: Molten metal zone state profiles for the Case Study 2A without disturbance state augmentation. (×) represents the estimated states while (–) represents the actual states

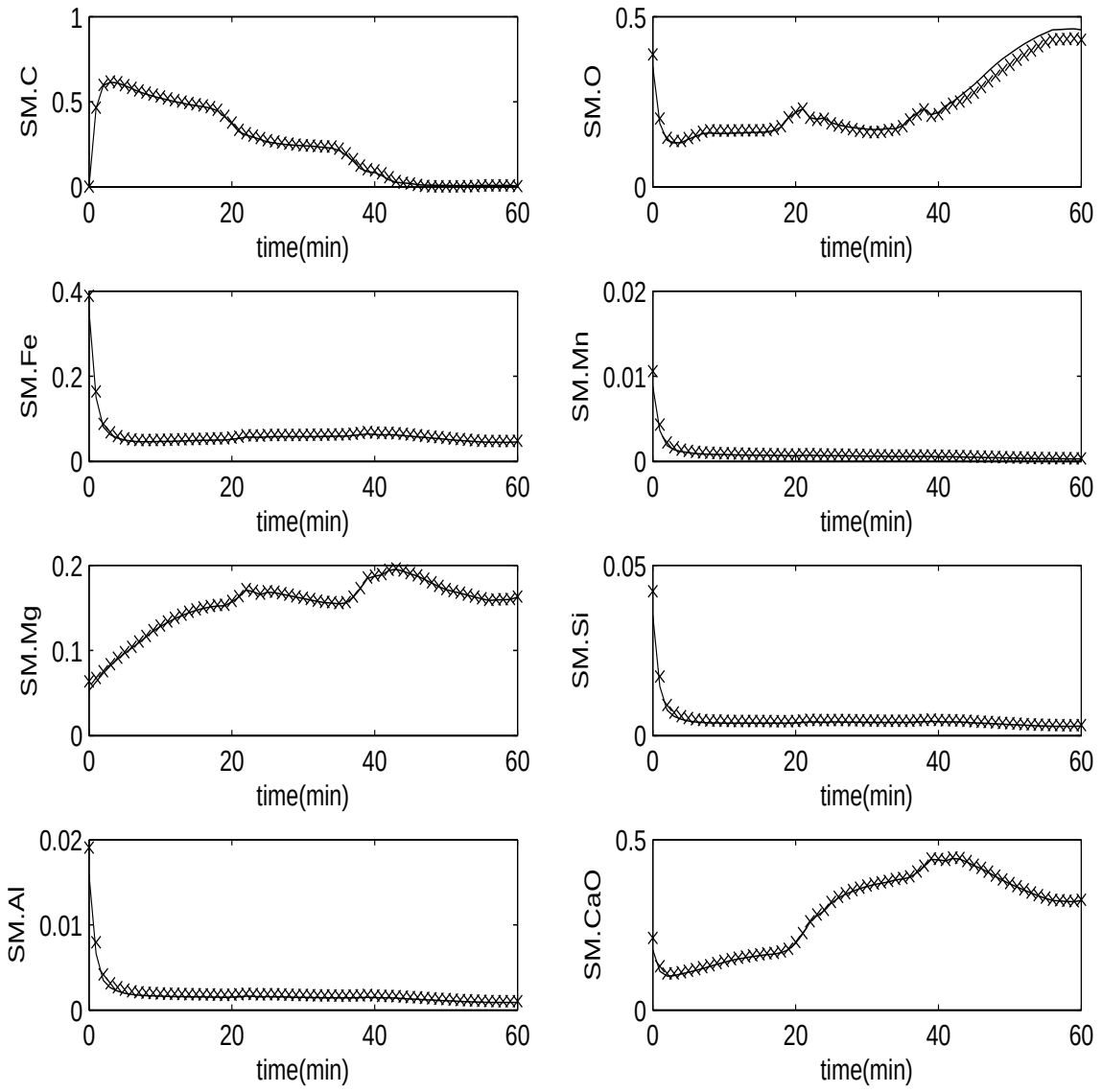

Figure 5.15: Slag zone state profiles for the Case Study 2A without disturbance state augmentation. (×) represents the estimated states while (–) represents the actual states

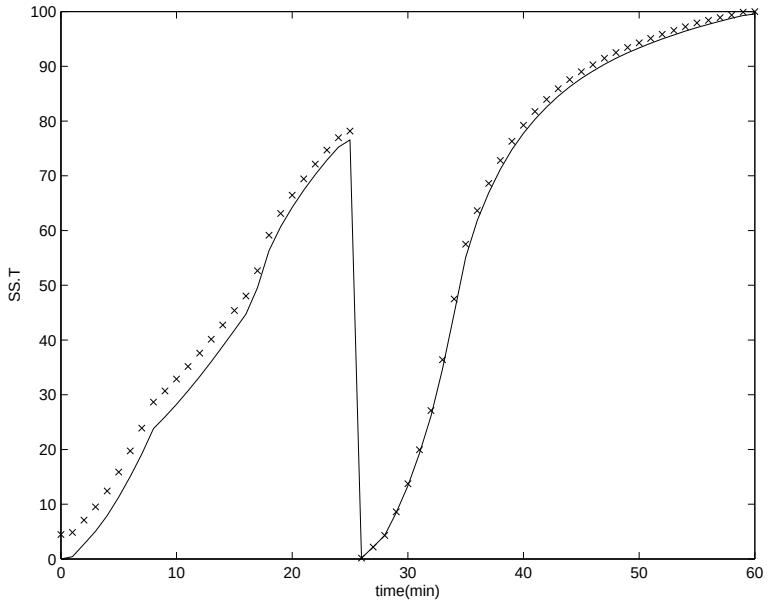

Figure 5.16: Solid zone state profiles for the Case Study 2A without state augmentation. (×) represents the estimated states while (–) represents the actual states

Case study 2B: Augmented Disturbances

Five disturbances were chosen to be augmented to the process states. Those disturbances were chosen to affect specific process states, which are (MM.T), (MM.C), (MM.O), (SM.O) and (MM.Al) in sequence. The tuning parameters (A_k^d), (Q^d) and (P_0^{+d}) are provided in Appendix C.3, as well as the initial disturbance state estimates (x_0^{+d}). The stochastic disturbances have shown a great impact in improving the performance of the EKF, in which it was able to eliminate the offsets that were present in the base case. Figures 5.17-5.20 show the effect of the stochastic disturbances on the performance of the EKF in the presence of plant-model mismatch. The disturbances were able to completely remove the offset from all the trajectories that were mentioned above.

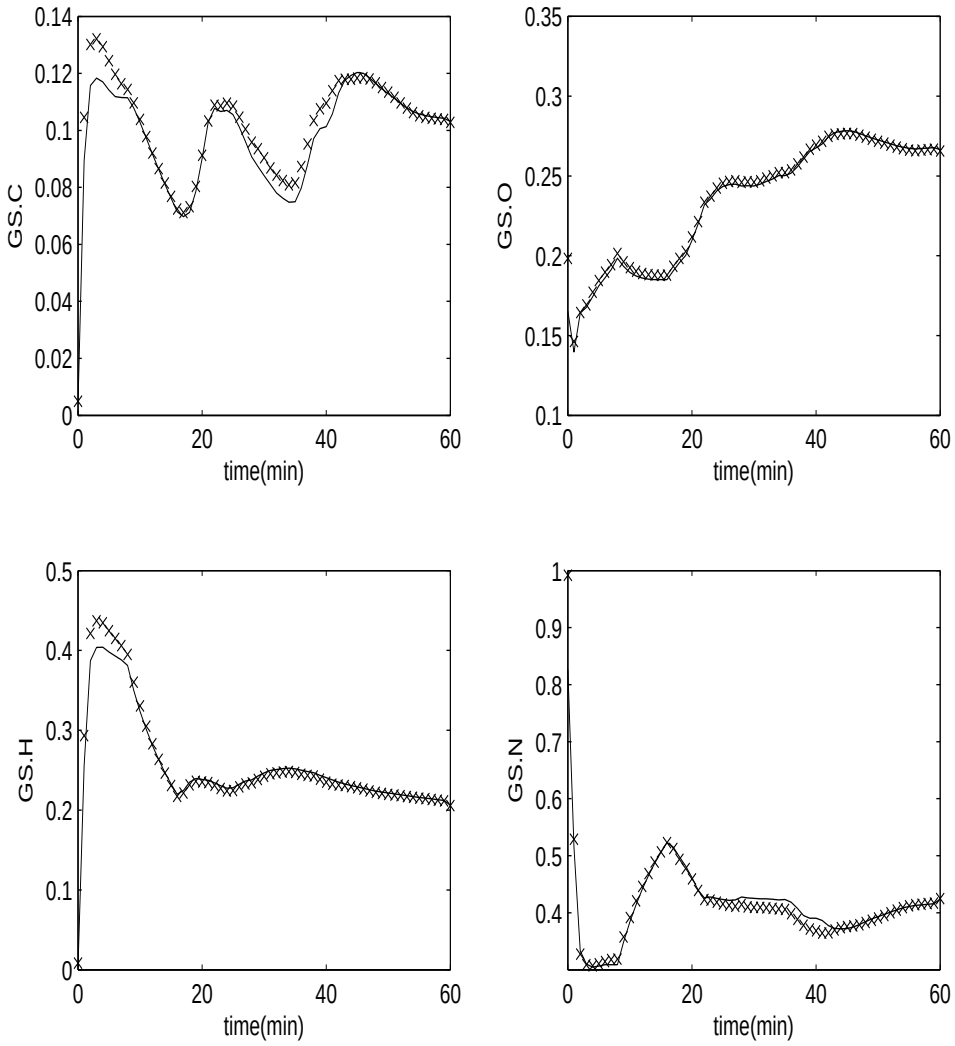

Figure 5.17: Gas zone state profiles for the Case Study 2B with disturbance state augmentation. (×) represents the estimated states while (–) represents the actual states

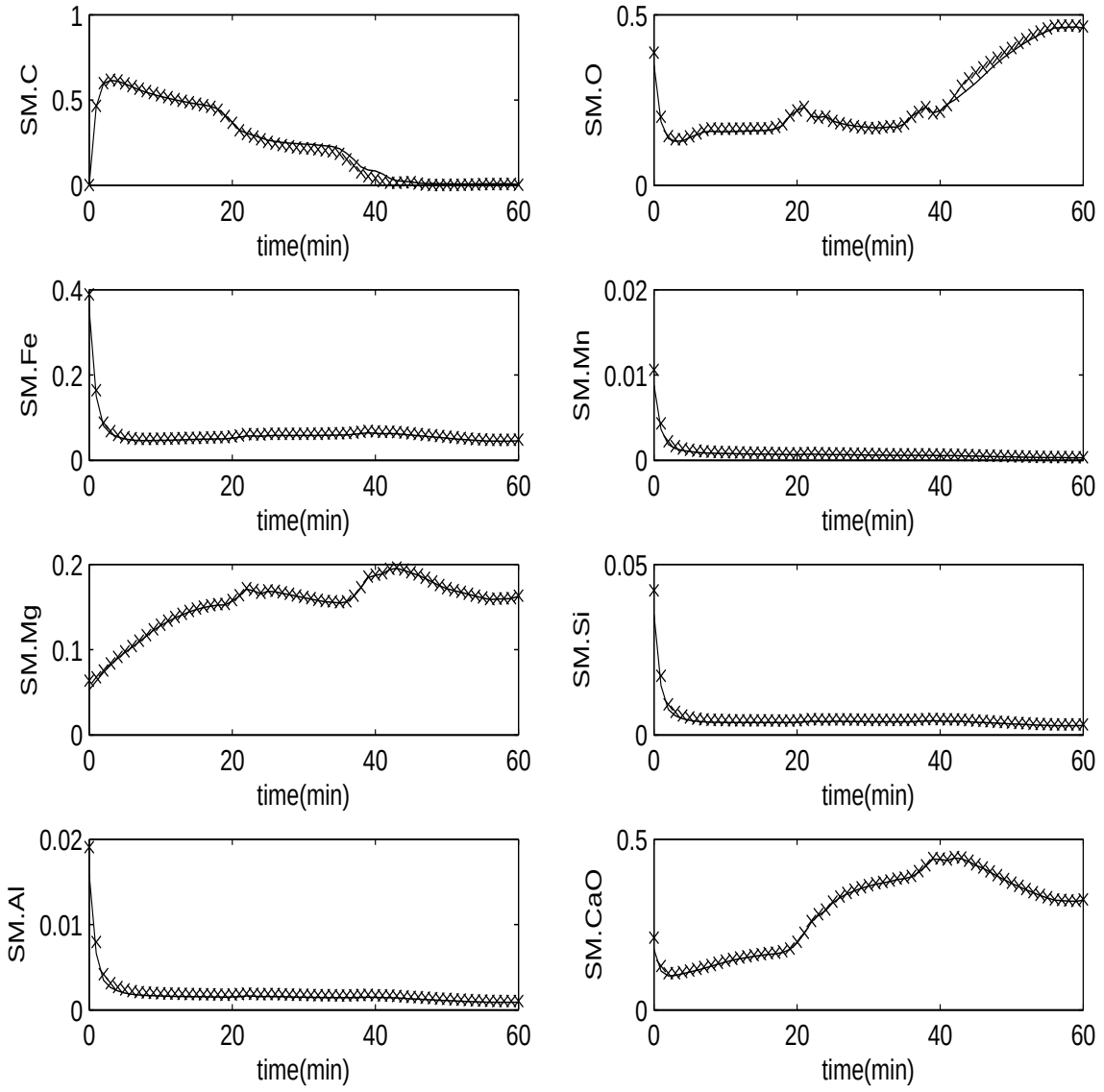

Figure 5.18: Slag zone state profiles for the Case Study 2B with disturbance state augmentation. (×) represents the estimated states while (–) represents the actual states

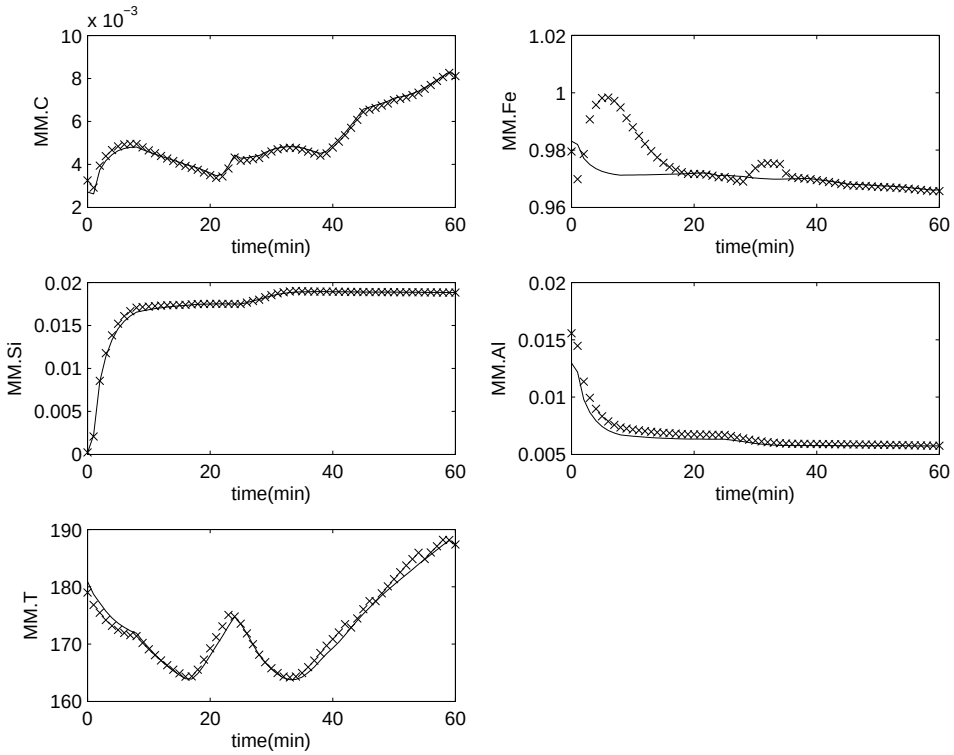

Figure 5.19: Molten metal zone state profiles for the Case Study 2B with disturbance state augmentation. (×) represents the estimated states while (–) represents the actual states

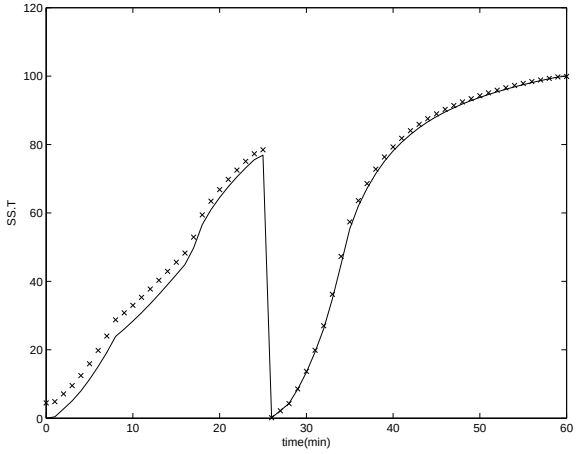

Figure 5.20: Solid zone state profiles for the Case Study 2B with disturbance state augmentation. (×) represents the estimated states while (–) represents the actual states

Chapter 6

Conclusions and Recommendations

The intent of this chapter is to summarize the findings of this research and recommend some potential future work.

6.1 Conclusions

A detailed first principles model for the electric arc furnace (EAF) obtained from MacRosty and Swartz [2005] has been reconfigured and modified to meet a new industrial partner's operation. The two major modifications in the model involved the addition of three JetBoxes, which control the supply of oxygen to the furnace. The second modification was through assuming a flat surface geometry for the scrap melting. Some assumptions were made throughout the model and validated based on simulation results.

The model has been validated against plant data through parameter estimation. A sensitivity analysis on the parameters was performed using local differential analysis and 6 parameters have been identified to be the most sensitive. An initial set of

parameters was obtained through brute force method and the 6 most sensitive parameters were estimated using the maximum-likelihood function in gPROMS/gEST. A sensitivity analysis on the initial composition of the scrap and fluxes that enter the furnace was performed using local differential analysis. It was found that iron has the highest influence on the EAF operation and manganese has the least effect. This analysis enhanced the understanding of the effect of each scrap component on the operation of the electric arc furnace.

The optimal input profiles of the furnace were determined through economic optimization. The trade-off between chemical and electrical energy was captured, in which more electrical energy is consumed, when the electricity price is low and as a result less chemical energy is used. On the other hand, when the electricity price is high more chemical energy is consumed over electrical energy.

The internal states of the system were estimated through the implementation of a constrained multi-rate extended Kalman filter. An observability test was performed and the system was found to be fully observable. Tuning parameters were obtained through trial and error and stochastic disturbances were considered to add an integral action. The filter showed satisfactory performance in predicting the true states of the system even in the presence of parametric plant-model mismatch.

6.2 Recommendations for Further Work

Further potential research and improvements could be investigated due to the complex nature of the EAF operation. In this section we will provide some potential future work that could be investigated based on the current work that has been completed.

6.2.1 Modeling Approach

Rigorous, first principles models for the electric arc furnace operation are highly complex. Such models are suitable to be used offline due to their complexity and high computational time. The potential use of data driven models, such as partial least squares (PLS) would seem promising for real-time applications. Developing such models does not require significant amount of time as that for a first principles model, and the solution time should be significantly reduced. A hybrid approach could also be used, in which the measurements from the plant in addition to data generated from a first principles model could be used combined to build a PLS model. This would then allow the data driven model to predict variables that are not measured by the plant. Data driven models could be also be used to implement optimization and control strategies. Sandberg *et al.* [2005] implemented a PLS model using data from 4 EAFs in Sweden and Norway, to predict the final alloying (Cr, Ni, Mo) and tramp elements (Cu, As, Sn) contents, beside the yield of oxidizable and impurity elements (C, Si, Mn, P, S), and electrical energy consumption. The model performance was satisfactory for the alloying and tramp elements predictions and unsatisfactory for the others. Scrap management applications were discussed, in which a PLS model would be used to predict the scrap grade composition and be used to optimize the addition of the second scrap basket.

6.2.2 Optimization

The optimization case studies investigated in this research focused on economic optimization; however the objective function can incorporate other criteria such as productivity, etc. The sequential approach was used to solve the optimization problem. The next stage is to use a simultaneous approach and compare its computational time for optimization with the sequential method. Reducing the optimization computation

time will enhance the on-line implementation of the model.

6.2.3 State Estimation and Control

The extended Kalman filter was used in this work; however other nonlinear state observers such as the moving horizon estimator (MHE) could also be investigated. Comparing the performance of both filters on the EAF would be of great interest. Lima and Rawlings [2011] implemented both an EKF and a MHE on a continuous stirred tank reactor (CSTR). The MHE showed a better performance than the EKF. The other potential is to incorporate a real-time optimization framework that would be coupled to the state estimator. This could be used as an advisory tool for the operator, to find the optimal input trajectories along the batch at every time step. Park *et al.* [2002] implemented a model predictive controller (MPC) coupled to an extended Kalman filter (EKF) on a semi-batch copolymerization reactor, in which the reaction temperature and feed rate of the polymer were manipulated to control the weight average molecular weight and the copolymer composition.

List of References

Bageshwar, V. (2008). *Quantifying Performance Limitations of Kalman Filters in State Vector Estimation Problems*. University of Minnesota.

Becerra, V., Roberts, P., and Griffiths, G. (2001). Applying the extended Kalman filter to systems described by nonlinear differential-algebraic equations. *Control Engineering Practice.*, **9**, 267–281.

Bekker, J., Craig, I., and Pistorius, P. (2000). Model predictive control of an electric arc furnace off-gas process. *Control Engineering Practice*, **8**(4), 445 – 455.

Bekker, J. G., Craig, I. K., and Pistorius, P. C. (1999). Modeling and simulation of an electric arc furnace process. *ISIJ (Iron Steel Institution Japan) International*, **39**, 23–32.

Biegler, L. T., Damiano, J. J., and Blau, G. E. (1986). Nonlinear parameter estimation: A case study comparison. *AIChE Journal*, **32**(1), 29–45.

Biegler, L. T. and Grossmann, I. E. (2004). Retrospective on optimization. *Computers & Chemical Engineering*, **28**(8), 1169 – 1192.

Billings, S. A., Boland, F. M., and Nicholson, H. (1979). Electric arc furnace modelling and control. *Automatica*, **15**, 137–148.

Böhm, C., Findeisen, R., and Allgöwer, F. (2008). Proceedings of the 17^{th} IFAC World Congress. In *Africon, 1999 IEEE*, Vol. 17, pp. 1952–1957.

Brhel, J. (2002). *JetBox^{TM}* - Chemical Energy System. Surrey, United Kingdom.

Brogan, W. L. (1991). *Modern Control Theory*. Prentice-Hall.

Cervantes, A. and Biegler, L. T. (2001). Optimization strategies for dynamic systems. In *C. Floudas, P. Pardalos (Eds), Encyclopedia of Optimization*. Kluwer Academic Publishers.

Chachuat, B. (2009). *Nonlinear and Dynamic Optimization: From Theory to Practice - IC-32: Spring Term 2009*. Polycopiés de l'EPFL. EPFL.

Chong, Z. (2012). *Dynamic Optimization Formulations for plant operation under partial shutdown conditions*. PhD Thesis, McMaster University.

Clarke-Pringle, T. and MacGregor, J. F. (1997). Nonlinear adaptive temperature control of multi-product, semi-batch polymerization reactors. *Computers and Chemical Engineering*, **21**, 1395–1409.

Dochain, D. (2003). State and parameter estimation in chemical and biochemical processes: a tutorial. *Journal of Process Control*, **13**(8), 801 – 818.

Franceschini, G. and Macchietto, S. (2008). Model-based design of experiments for parameter precision: State of the art. *Chemical Engineering Science*, **63**, 4846 – 4872.

Fruehan, R. J. (1998). *The Making, Shaping and Treating of Steel*. AISE Steel Foundation, 11^{th} edition.

Gitgarts, D. A. and Vershinina, T. I. (1984). Dynamic optimization of the electrical operating conditions of electric arc steelmelting furnaces. *Soviet Electrical Engineering*, **55(2)**, 25–28.

Görtler, G. and Jörgl, H. P. (2004). Energetically optimized control of an electric arc furnace. In *Proceedings of the 2004 IEEE International Conference on Control Applications*, pp. 137–142.

Gosiewski, A. and Wierzbicki, A. (1970). Dynamic optimization of a steelmaking process in electric arc furnace. *Automatica*, **6**, 767–778.

Guo, D. and Irons, G. (2003). Modeling of radiation intensity in EAF. In *Proceedings of the 3rd International Conference on CFD in the Minerals and Process Industries*, pp. 223–228.

Huang, Z., Chu, Y., and Hahn, J. (2010). Model simplification procedure for signal transduction pathway models: An application to IL-6 signaling. *Chemical Engineering Science*, **65**, 1964 – 1975.

Irons, G. (2005). Developments in electric arc furnace steelmaking. In *AISTech 2005 Proceedings*.

Jiang, R. and Fruehan, R. (1991). Viscosity estimation of slags. *Metallurgical Transactions B*, **22B**, 111–116.

Jones, J., Safe, P., and Wiggins, B. (1999). Modeling of radiation intensity in EAF. In *Electric Furnace Conference Proceedings*, pp. 459–480.

Jones, J. A. T., Bowman, B., and Lefrank, P. (1998). Electric furnace steelmaking. In *The AISE Steel Foundation*, pp. 624–628.

Kozub, D. J. and MacGregor, J. F. (1992). State estimation for semi-batch polymerization reactors. *Chemical Engineering Science.*, **47**, 1047–1062.

Kravaris, C., Hahn, J., and Chu, Y. (2013). Advances and selected recent developments in state and parameter estimation. *Computers & Chemical Engineering*, **51**(0), 111 – 123.

Lainchbury, S. (2003). Results validate $JetBox^{TM}$ EAF injection system. Surrey, United Kingdom.

Lima, F., Rajamani, M. R., Soderstrom, T. A., and Rawlings, J. B. (2013). Covariance and state estimation of weakly observable systems: Application to polymerization processes. *IEEE Transactions on Control Systems Technology*, **21**, 1249–1257.

Lima, F. V. and Rawlings, J. B. (2011). Nonlinear stochastic modeling to improve state estimation in process monitoring and control. *American Institute of Chemical Engineers*, **57**, 996–1007.

Logar, V., Dovžan, D., and Škrjanc, I. (2012a). Modeling and validation of an electric arc furnace: Part1, heat and mass transfer. *ISIJ International*, **52**, 402–412.

Logar, V., Dovžan, D., and Škrjanc, I. (2012b). Modeling and validation of an electric arc furnace: Part2, thermo-chemistry. *ISIJ International*, **52**, 413–423.

MacRosty, R. D. and Swartz, C. L. E. (2005). Dynamic modeling of an industrial electric arc furnace. *Ind.Eng.Chem.Res.*, **44**, 8067 – 8083.

MacRosty, R. D. M. and Swartz, C. L. E. (2007). Dynamic optimization of electric arc furnace operation. *AIChE Journal*, **53**, 640 – 653.

Marafioti, G., Olaru, S., and Hovd, M. (2009). State estimation in nonlinear model predictive control, unscented Kalman filter advantages. In Magni, L., Raimondo, D., and Allgöwer, F. (Eds.), *Nonlinear Model Predictive Control*, Vol. 384 of *Lecture Notes in Control and Information Sciences*, pp. 305–313. Springer Berlin Heidelberg.

MathWorks (2013). Control system *toolbox*^{TM} user's guide. Natick,MA.

Matson, S. and Ramirez, W. F. (1997). The dynamic modeling of an electric arc furnace. In *Electric Furnace Conference Proceedings*, pp. 675–685.

Matson, S. and Ramirez, W. F. (1999). Optimal operation of an electric arc furnace. In 57^{th} *Electric Furnace Conference Proceedings*, pp. 719–728, Warrendale, PA.

McAuley, K. B., Wu, S., and Harris, T. J. (2010). Selecting parameters to estimate to obtain the best model predictions. In *Proceedings of the 2010 International Conference on Modelling, Identification and Control*, pp. 161–166.

McLean, K. A. P. and McAuley, K. B. (2012). Mathematical modelling of chemical processes - Obtaining the best model predictions and parameter estimates using identifiability and estimability procedures. *The Canadian Journal Of Chemical Engineering*, **90**, 351– 366.

McLean, K. A. P., Wu, S., and McAuley, K. B. (2012). Mean-squared-error methods for selecting optimal parameter subsets for estimation. *Industrial and Engineering Chemistry Research*, **51**, 6105 – 6115.

Mills, K. C. and Keene, B. (1987). Physical properties of BOS slags. *International Materials Reviews*, **32(1-2)**, 1 – 114.

Modigell, M., Traebert, A., and Monheim, P. (2001). A modeling technique for metallurgical processes and its applications. *AISE Steel Technology*, **28**, 45–47.

Morales, R. D., Rodriguez-Hernandez, H., Garnica-Gonzalez, P., and Romero-Serrano, J. A. (1997). A mathematical model for the reduction kinetics of iron oxide in electric furnace slags by graphite injection. *ISIJ International*, **37(11)**, 1072–1080.

Nyssen, P., Colin, R., J. L. Junqu, n., and Knoops, S. (2004). Application of a dynamic metallurgical model to the electric arc furnace. *Revue de Mtallurgie*, **101**, 317–326.

Oosthuizen, D., Craig, I., and Pistorius, P. (2004). Economic evaluation and design of an electric arc furnace controller based on economic objectives. *Control Engineering Practice*, **12**(3), 253 – 265.

Oosthuizen, D. J., Craig, I., and Pistorius, P. C. (1999). Model predictive control of an electric arc furnace offgas procedure combined with temperature control. In *Africon, 1999 IEEE*, Vol. 1, pp. 415–420 vol.1.

Park, M.-J., Hur, S.-M., and Rhee, H.-K. (2002). Online estimation and control of polymer quality in a copolymerization reactor. *AIChE Journal*, **48(5)**, 1013–1021.

Park, P. and Kailath, T. (1995). New square-root algorithms for Kalman filtering. *Automatic Control, IEEE Transactions on*, **40**(5), 895–899.

Pozzi, M., Maiolo, J., and Memoli, F. (2005). EAF process optimisation with Techint technologies. *Steel Times International*, **29(3)**, 20–22.

Prakash, J., Patwardhan, S. C., and Shah, S. L. (2010). State estimation and nonlinear predictive control of autonomous hybrid system using derivative free state estimators. *Journal of Process Control*, **20**(7), 787 – 799.

Prasad, V., Schely, M., Russo, L. P., and Bequette, B. W. (2002). Product property and production rate control of styrene polymerization. *Journal of Process Control*, **12**, 353 – 372.

Pretorius, E. B. and Carlisle, R. C. (1998). Foamy slag fundamentals and their practical application to electric furnace steelmaking. In *EAF Conference*, pp. 624–628.

Process Systems Enterprise Ltd. (2004). gPROMS Advanced User Guide. London, United Kingdom.

Sandberg, E., Lennox, B., Marjanovic, O., and Smith, K. (2005). Multivariate process monitoring of EAFs. *Ironmaking and Steelmaking*, **32(3)**, 221–225.

Siegel, R. and Howell, J. (2001). *Thermal Radiation Heat Transfer*. Taylor and Francis, 4^{th} edition edition.

Simon, D. (2006). *Optimal State Estimation Kalman, H_∞, and Nonlinear Approaches*. Wiley.

Southall, B., Buxton, B. F., and Marchant, J. A. (1998). Controllability and observability: Tools for Kalman filter design.

Stankevic, Y. A., Timoshpol'skii, V. I., Pavlyukevich, N. V., German, M. G., and Grinchuk, P. S. (2009). Mathematical modeling of the heating and melting of the metal charge in an electric-arc steel making furnace. *Journal of Engineering Physics and Thermophysics*, **82**, 221–235.

Urbain, G. (1987). Viscosity estimation of slags. *Steel Research*, **58(3)**, 111–116.

Vassiliadis, V. S., Sargent, R. W. H., and Pantelides, C. C. (1994). Solution of a class of multistage dynamic optimization problems. 1. problems without path constraints. *Industrial & Engineering Chemistry Research*, **33**(9), 2111–2122.

Wai, C. M. and Hutchison, S. G. (1989). Free energy minimization calculation of complex chemical equilibria. *Journal of Chemical Education*, **66(7)**, 546–549.

Wang, F., Jin, Z., Zhu, Z., and Wang, X. (2005). Application of extended Kalman filter to the modeling of electric arc furnace for power quality issues. *IEEE*, **05**, 991–996.

Wendelstorf, J. (2008). Analysis of the EAF operation by process modelling. *Archives of Metallurgy and Materials*, **53**, 385–390.

Wendelstorf, J. and Spitzer, K.-H. (2006). A process model for EAF steelmaking. *AISTech*, **2**, 435–443.

Woodside, C. M., Pagurek, B., Pauksens, J., and Ogale, A. N. (1970). Singular arcs occurring in optimal electric steel refining. *IEEE Transactions on Automatic Control*, **AC-15**, 549–556.

World Steel Association (2012). Crude Steel Production. `http://www.worldsteel.org/dms/internetDocumentList/steel-stats/2013/Crude-steel-pdf/document/Steel`.

Wu, Y., Zhang, H., Wu, M., Hu, X., and Hu, D. (2012). Observability of Strapdown INS Alignment: A Global Perspective. *Aerospace and Electronic Systems, IEEE Transactions on*, **48**(1), 78–102.

Xue, D., C. Y. and Atherton, D. P. (2007). *Linear Feedback Control, Analysis and Design with MATLAB*. Siam.

Appendix A

Modeling Details

A.1 Molten Metal Temperature

The molten metal temperature is calculated as shown in equation (A.1). C_p is the specific heat capacity, n is the number of moles and sub is an estimated parameter to account for bulk density and compositional variation. Equation (A.2) describes the cooling that results from the water sprays on the molten metal temperature profile, and k_{mcool} is an estimated parameter.

$$\frac{dT}{dt}(\sum_{i=1}^{16}(n(i)C_p(i))sub) = Q_{power-mm} - Q_{mm-ss} - Q_{cool} - Q_{mm-sm} - q_{rad}^4 \quad \text{(A.1)}$$

$$Q_{cool} = k_{mcool}(T_{mm} - 298K); \quad \text{(A.2)}$$

A.2 Offgas flow rate and entrained air

In this section, the calculations for the amount of gas being sucked and pushed away are shown. A pseudo steady state assumption is made about the freeboard gas volume in which constant pressure is assumed. The air being sucked (F_{suck}) or pushed away (F_{push}) depends on this pseudo steady state and the constant offgas flow rate assumed. The max and min functions that were discussed in equation (3.25) are approximated as shown in the equations below (Biegler and Grossmann [2004]; MacRosty and Swartz [2007]).

$$F_{suck} = \max(0, F_{net}) = \frac{1}{2}F_{net} + \frac{1}{2}(F_{net}^2 + \epsilon)^{\frac{1}{2}} \tag{A.3}$$

$$F_{push} = \min(0, F_{net}) = -\frac{1}{2}F_{net} + \frac{1}{2}(F_{net}^2 + \epsilon)^{\frac{1}{2}} \tag{A.4}$$

in which ϵ has a magnitude of 1×10^{-3}, and F_{net} is calculated based on the constant pressure assumption in the freeboard gas volume and is calculated using the expression below:

$$F_{net} = F_{offgas} - F_{sm-gs} - F_{burner} - F_{volatile} \tag{A.5}$$

The offgas flow rate (F_{offgas}) is calculated using the ideal gas law as shown in the expression below, in which R is the gas constant, T is the offgas duct's temperature, P is the offgas duct's pressure, $\dot{V}_{offgas}$ is the volumetric flow rate in the offgas duct based on the fan speed and the cross-sectional area of the duct, and $EA1$ is an estimated parameter.

$$F_{offgas}(RT) = \dot{V}_{offgas}\ P\ EA_1; \tag{A.6}$$

As mentioned in Section 3.1.3, the gases ingressed will have the same composition as ambient air and the flow rate of the ingressed components could be calculated as

follows:

$$F_{ingressed,i} = X_{air,i}\ F_{suck}\ EA_3 \tag{A.7}$$

It is expected that both parameters EA_1 and EA_3 would be highly correlated. The reason for including EA_3 in this model was to account for ingressed air that has not been considered in the model due to opening of the roof of the furnace. However, it is suggested in further work that the parameter EA_3 could be neglected and only EA_1 would be estimated.

F_{push} and $F_{ingressed,i}$ are then related to $F_{Pconst,i}$ in equation (3.25) as shown below:

$$F_{Pconst,i} = x_{freeboard-gas,i}F_{push} + F_{ingressed,i} \tag{A.8}$$

A.3 Total Carbon entering the slag-metal interaction zone

In this section, the rate of addition of carbon charged and lanced ($F^{C}_{add,sm}$) into the slag-metal zone is shown. k_c is an estimated parameter which represents the amount of reacted carbon.

$$F^{C}_{add,sm} = k_c F_C^{Charge+Lanced} \tag{A.9}$$

A.4 Water entering the gas zone

The molar amount of water added to the gas zone ($F^{H_2O}_{add}$) is modeled as shown below. $\dot{V}^{Spray}_{H_2O}$ is the volumetric flow rate of water from the sprays and $Fstar_{H2O}$ is an estimated parameter. The ideal gas law is used in which P is the pressure of the freeboard gas volume and T is the temperature of the gas zone.

$$F^{H_2O}_{add}\ R\ T = \dot{V}^{Spray}_{H_2O}\ Fstar_{H2O}\ P \tag{A.10}$$

A.5 View Factors Calculations

In this section, the view factors calculations are shown in detail. Those relationships were obtained from Siegel and Howell [2001]. The five surfaces being considered are the roof (disk), wall (right circular cylinder), scrap (coaxial disk), bath (coaxial disk) and arc (cylinder) as discussed in Section 3.4.

A.5.1 Roof

The radiation flow from the roof to the molten metal and the scrap is represented by equations (A.12) and (A.11) respectively. $Switch^{rad}$ is the switch function to account when the molten metal and scrap perceives the roof of the furnace. r is the radius of the surface which is assumed to be the same for the roof, molten metal and scrap. a is the distance between the roof and the corresponding surface.

$$\begin{aligned} F_{1-3} &= Switch^{rad}\ \frac{1}{2}\left[X-(X^2-4)^{\frac{1}{2}}\right] \\ R &= \frac{r}{a} \\ X &= \frac{(2R^2+1)}{R^2} \end{aligned} \tag{A.11}$$

$$\begin{aligned} F_{1-4} &= (1-Switch^{rad})\ \frac{1}{2}\left[X-(X^2-4)^{\frac{1}{2}}\right] \\ R &= \frac{r}{a} \\ X &= \frac{(2R^2+1)}{R^2} \end{aligned} \tag{A.12}$$

No radiation flow from the roof to the arc exists, since the arc is assumed to be a black body (equation A.13). Also, as a result of assuming the roof as a flat surface,

no radiation occurs within the roof itself (equation A.14).

$$F_{1-5} = 0 \tag{A.13}$$

$$F_{1-1} = 0 \tag{A.14}$$

A.5.2 Wall

The fraction of energy transferred from the wall to the roof is calculated as shown in equation (A.15), in which h_1 is the height of the exposed wall, h_2 is the distance between the roof and exposed wall height and r is the radius of the roof of the furnace.

$$\begin{aligned} F_{2-1} &= \frac{1}{4}\left((1+\tfrac{H_2}{H_1})\Big[4+(H_1+H_2)^2\Big]^{\frac{1}{2}} - (H_1+2H_2) - \tfrac{H_2}{H_1}(4+H_2^2)^{\frac{1}{2}}\right) \\ H_1 &= \frac{h_1}{r} \\ H_2 &= \frac{h_2}{r} \end{aligned} \tag{A.15}$$

The fraction of radiation transferred between the inside walls of the furnace and itself is approximated as shown in equation (A.16), in which h is the height of exposed wall and r is the radius of the furnace.

$$\begin{aligned} F_{2-2} &= (1+H) - (1+H^2)^{\frac{1}{2}} \\ H &= \frac{h}{2r} \end{aligned} \tag{A.16}$$

The view factors from the wall to the scrap and bath are calculated though the reciprocity (equation A.18) and enclosure constraint respectively. No radiation is received by the arc from the wall as shown in equation (A.17) below.

$$F_{2-5} = 0 \tag{A.17}$$

$$F_{2-3} = F_{3-2}\ \frac{A_3}{A_2} \tag{A.18}$$

A.5.3 Scrap

The calculations for the fraction of energy from scrap to the other surfaces are shown in equations (A.19-A.23). It is assumed that no radiation takes place between the scrap and molten metal as shown in equation (A.21). Also, no radiation takes place between the scrap and itself due to being a flat surface. Reciprocity relationship was used to calculate the radiation from the scrap to the roof as shown in equation (A.19) below.

$$F_{3-1} = F_{1-3}\ \frac{A_1}{A_3} \tag{A.19}$$

$$F_{3-3} = 0 \tag{A.20}$$

$$F_{3-4} = 0 \tag{A.21}$$

$$F_{3-5} = 0 \tag{A.22}$$

Equation (A.23) shows the fraction of radiation from the scrap to the wall, where h is the exposed wall height and r is the radius of scrap. It was made sure that the sum of the view factors equal to one to maintain the enclosure constraint, in the case when the scrap is present. $Switch^{rad}$ makes sure that when no scrap is present, no radiation is transfered to/from the scrap anymore.

$$\begin{aligned} F_{3-2} &= Switch^{rad}\ \left[2H\left((1+H^2)^{\frac{1}{2}} - H\right)\right] \\ H &= \frac{h}{2r} \end{aligned} \tag{A.23}$$

A.5.4 Molten Metal

The view factors for the molten metal are shown below. No radiation transfer takes place between the bath from one side and the scrap, bath and arc from the other. This is the same as has been assumed for the scrap. The fraction of radiation from the molten metal to the roof is calculated as through the reciprocity relationship as shown in equation (A.24). $Switch^{rad}$ makes sure that no radiation takes place when scrap amount dominates in the furnace.

$$F_{4-1} = F_{1-4}\ \frac{A_1}{A_4} \tag{A.24}$$

$$F_{4-3} = 0 \tag{A.25}$$

$$F_{4-4} = 0 \tag{A.26}$$

$$F_{4-5} = 0 \tag{A.27}$$

The radiation transfer from the bath to the wall is approximated through equation (A.28), in which h is the height of exposed wall and r is the radius of the bath. The sum of the view factors is ensured to be 1 when the molten metal dominates over the scrap amount.

$$\begin{aligned} F_{4-2} &= Switch^{rad}\ \left[2H\left((1+H^2)^{\frac{1}{2}} - H\right)\right] \\ H &= \frac{h}{2r} \end{aligned} \tag{A.28}$$

A.5.5 Arc

The fraction of radiation from the arc to the rest of the surfaces is calculated as shown below. The amount of radiation transfer from the arc to the scrap and the molten metal is calculated through equations (A.29) and (A.30) respectively. r_1 and

r_2 are the radius of the electrode and (bath/scrap) respectively. h is the exposed wall height.

$$F_{5-3} = Switch^{rad} \left[\frac{B}{8RH} + \frac{1}{2\pi}\left(cos^{-1}(\frac{A}{B}) - \frac{1}{2H}\left[\frac{(A+2)^2}{R^2} - 4\right]^{\frac{1}{2}} cos^{-1}(\frac{AR}{B}) - \frac{A}{2RH} sin^{-1}R\right)\right]$$
$$R = \frac{r_1}{r_2}$$
$$H = \frac{h}{r_2}$$
$$A = H^2 + R^2 - 1$$
$$B = H^2 - R^2 + 1 \tag{A.29}$$

$$F_{5-4} = (1 - Switch^{rad}) \left[\frac{B}{8RH} + \frac{1}{2\pi}\left(cos^{-1}(\frac{A}{B}) - \frac{1}{2H}\left[\frac{(A+2)^2}{R^2} - 4\right]^{\frac{1}{2}} cos^{-1}(\frac{AR}{B}) - \frac{A}{2RH} sin^{-1}R\right)\right]$$
$$R = \frac{r_1}{r_2}$$
$$H = \frac{h}{r_2}$$
$$A = H^2 + R^2 - 1$$
$$B = H^2 - R^2 + 1 \tag{A.30}$$

The radiation transfer between the arc and the wall is approximated through equation (A.31), in which h is the height of the exposed wall. r_1 and r_2 are the radius of the electrode and wall respectively. No radiation is exchanged between the arc itself and the fraction of radiative transfer between the arc and the roof would be calculated using the enclosure constraint property.

$$
\begin{aligned}
F_{5-2} &= \frac{1}{\pi R_1}\begin{bmatrix} \frac{1}{2}(R_2^2 - R_1^2 - 1)cos^{-1}\frac{R_1}{R_2} + \pi R_1 - \frac{\pi}{2}AB - 2R_1 tan^{-1}(R_2^2 - R_1^2)^{\frac{1}{2}} + \\ \Big((1+A^2)(1+B^2)\Big)^{\frac{1}{2}} tan^{-1}\Big(\frac{(1+A^2)B}{(1+B^2)A}\Big)^{\frac{1}{2}} \end{bmatrix} \\
R_1 &= \frac{r_1}{h} \\
R_2 &= \frac{r_2}{h} \\
A &= R_2 + R_1 \\
B &= R_2 - R_1
\end{aligned}
\tag{A.31}
$$

$$F_{5-5} = 0 \tag{A.32}$$

A.6 Procedure for normalizing the trajectories

The trajectories are normalized between 0 and 100 using the maximum and minimum values for all the trajectories involved in a specified figure. For example, consider two trajectories $\mathbf{x}$ and $\mathbf{y}$. The normalized trajectory for each variable could be calculated as follows:

$$\mathbf{x}_{\text{normalized}} = 100[\mathbf{x} - \min(x_{min}, y_{min})]/[\max(x_{max}, y_{max}) - \min(x_{min}, y_{min})] \tag{A.33}$$

$$\mathbf{y}_{\text{normalized}} = 100[\mathbf{y} - \min(x_{min}, y_{min})]/[\max(x_{max}, y_{max}) - \min(x_{min}, y_{min})] \tag{A.34}$$

such that:

$$x_{min} = \min(\mathbf{x}) \tag{A.35}$$

$$y_{min} = \min(\mathbf{y}) \tag{A.36}$$

$$x_{max} = \max(\mathbf{x}) \tag{A.37}$$

$$y_{max} = \max(\mathbf{y}) \tag{A.38}$$

Appendix B

Parameter Estimation

Table B.1: Model parameters

Parameter	**Value**
k_{cool}	1.169×10^{1}
k_{dm}	4.5×10^{-1}
k_{dt}	6.9×10^{-1}
k_p	8×10^{-1}
k_{t1}	4.2×10^{-4}
k_{t3}	3.1×10^{-8}
k_m	1.66×10^{4}
k_{mcool}	6×10^{-3}
k_{t2}	8.5×10^{-3}
sub	8×10^{-1}
θ_L	7.5×10^{-1}
y_C^*	2×10^{-3}
γ_d	8×10^{-1}
α_3	3.7×10^{-1}
β_3	1.11×10^{-2}
$Bias_{O_2}GS^\star$	7×10^{-1}
EA_1	1.34×10^{-1}
EA_3	1.3
$Fstar_{H2O}$	2
k_{oil}	8.27×10^{-1}
k_{PO2}	1.3×10^{2}
θ_3	1×10^{1}
$Xoil$	6×10^{-1}
$Bias_{O_2}SM^\star$	1
k_c	9.6×10^{-2}
k_{cao}	7×10^{-1}
k_{dc}	4.37×10^{-1}
h_{gs}	4.35

Appendix C

State Estimation

C.1 Converting DAE system to ODE state space model using linearization

In this section, the derivation for converting a DAE system to an ODE system will be illustrated (Becerra *et al.* [2001]).

Considering a DAE system described by the equations below, in which x and z represent differential states and algebraic variables respectively. u is the vector of input variables.

$$\begin{aligned} \dot{x}(t) &= f(x(t), u(t), z(t), t) \\ g(x(t), u(t), z(t), t) &= 0 \end{aligned} \tag{C.1}$$

The measurement model is described as shown below, where y represent the measured variables.

$$y(t_k) = h(x(t_k)) \tag{C.2}$$

Using a reference trajectory $(x^*(t), \dot{x}^*(t), z^*(t), u^*(t))$, the variables are expressed in

their deviation form as follows:

$$\bar{x}(t) = x(t) - x^*(t) \tag{C.3}$$

$$\dot{\bar{x}}(t) = \dot{x}(t) - \dot{x}^*(t) \tag{C.4}$$

$$\bar{z}(t) = z(t) - z^*(t) \tag{C.5}$$

$$\bar{u}(t) = u(t) - u^*(t) \tag{C.6}$$

$$\bar{y}(t) = y(t) - y^*(t) \tag{C.7}$$

The set of differential equations are rewritten as follows:

$$F(\dot{x}(t), x(t), u(t), z(t), t) = \dot{x} - f(x(t), u(t), z(t), t) = 0 \tag{C.8}$$

Through carrying out a first-order Taylor series expansion of F and g about the trajectory $(x^*(t), \dot{x}^*(t), z^*(t), u^*(t))$, the following expressions are obtained.

$$F(\dot{x}^*+\dot{\bar{x}}, x^*+\bar{x}, u^*+\bar{u}, z^*+\bar{z}, t) = F(\dot{x}^*, x^*, u^*, z^*, t)+F_{\dot{x}}\dot{\bar{x}}+F_x\bar{x}+F_u\bar{u}+F_z\bar{z} = 0 \tag{C.9}$$

$$g(x^* + \bar{x}, u^* + \bar{u}, z^* + \bar{z}, t) = g(x^*, u^*, z^*, t) + g_x\bar{x} + g_u\bar{u} + g_z\bar{z} = 0 \tag{C.10}$$

By definition, $F(\dot{x}^*, x^*, u^*, z^*, t)$ and $g(x^*, u^*, z^*, t)$ are equal to 0, and therefore the following expressions are obtained.

$$F_{\dot{x}}\dot{\bar{x}} + F_x\bar{x} + F_u\bar{u} + F_z\bar{z} = 0 \tag{C.11}$$

$$g_x\bar{x} + g_u\bar{u} + g_z\bar{z} = 0 \tag{C.12}$$

Equation (C.12) can be rearranged to solve for $\bar{z}$ as shown below.

$$\bar{z} = -g_z^{-1}[g_x\bar{x} + g_u\bar{u}] \tag{C.13}$$

Substituting (C.13) into (C.11) and solving for $\dot{\bar{x}}$ in which $F_{\dot{x}} = I$, the following linearized state expression is obtained.

$$\dot{\bar{x}} = [F_z g_z^{-1} g_x - F_x]\bar{x} + [F_z g_z^{-1} g_u - F_u]\bar{u} = A\bar{x} + B\bar{u} \tag{C.14}$$

The A and B matrices are therefore expressed as shown in the following equations:

$$A = F_z g_z^{-1} g_x - F_x \tag{C.15}$$

$$B = F_z g_z^{-1} g_u - F_u \tag{C.16}$$

The measurement equation is then linearized in the same way to obtain the following equation, in which h_x is evaluated along the trajectory $x^*(t)$.

$$\bar{y} = h_x \bar{x} = C\bar{x} \tag{C.17}$$

C.2 Local Observability Results

The rank test on the observability matrix which is obtained using the *obsv* command in $Matlab^{®}$ is shown below. The tolerance (*tol*) is calculated using equation (C.20) below, in which *eps* is the floating-point relative accuracy determined by $Matlab^{®}$.

$$Ob = obsv(A, C) \tag{C.18}$$

$$r = rank(ob, tol) \tag{C.19}$$

$$tol = max(size(A))\ eps(norm(A)) \tag{C.20}$$

The similarity transformation is carried out using the *obsvf* command in $Matlab^{®}$ as shown below:

$$[\bar{A}, \bar{B}, \bar{C}, T, k] = obsvf(A, B, C, tol) \tag{C.21}$$

$$tol = 10\ n\ norm(A, 1)\ eps \tag{C.22}$$

The tolerance (tol) is calculated as shown in equation (C.22), in which n is the number of states in the A matrix. k is a vector of length n which represents the number of observable states that are factored out at each time step during the transformation matrix calculation. The sum of the elements in k would represent the number of states in the observable portion of $\bar{A}$ (MathWorks [2013]).

Table C.1: Observability Results for Case Study 1B with augmented disturbances

Time	**Number of observable states**
0	27
1	30
2	30
3	30
4	31
5	32
6	31
7	32
8	32
9	31
10	31
11	31
12	31
13	31
14	31
15	31
16	31
17	31
18	31
19	31
20	31
21	31
22	31
23	31
24	31
25	31
26	31
27	32
28	31
29	32
30	31

Time	**Number of observable states**
31	32
32	32
33	32
34	32
35	32
36	31
37	31
38	31
39	32
40	31
41	31
42	32
43	32
44	32
45	31
46	31
47	32
48	31
49	31
50	31
51	31
52	31
53	31
54	31
55	31
56	31
57	31
58	31
59	31
60	32

C.3 EKF parameters

The state vector $\mathbf{x}$ could be represented as,

$$\mathbf{x} = \begin{bmatrix} \mathbf{x}^{GS} \\ \mathbf{x}^{mm} \\ \mathbf{x}^{sm} \\ \mathbf{x}^{RD} \end{bmatrix}$$

such that:

$$\mathbf{x}^{GS} = \begin{bmatrix} \text{GS.C} \\ \text{GS.O} \\ \text{GS.H} \\ \text{GS.N} \\ \text{GS.Noilgas} \\ \text{SS.T} \\ \text{GS.E} \end{bmatrix} \quad \mathbf{x}^{mm} = \begin{bmatrix} \text{MM.C} \\ \text{MM.O} \\ \text{MM.Fe} \\ \text{MM.Mn} \\ \text{MM.Mg} \\ \text{MM.Si} \\ \text{MM.Al} \\ \text{MM.T} \\ \text{SS.mss} \end{bmatrix} \quad \mathbf{x}^{sm} = \begin{bmatrix} \text{SM.C} \\ \text{SM.O} \\ \text{SM.Fe} \\ \text{SM.Mn} \\ \text{SM.Mg} \\ \text{SM.Si} \\ \text{SM.Al} \\ \text{SM.CaO} \\ \text{SM.m}_{\text{CaO,float}} \\ \text{MM.m}_{\text{C,float}} \\ \text{MM.m}_{\text{dol,float}} \\ \text{SM.E} \end{bmatrix} \quad \mathbf{x}^{RD} = \begin{bmatrix} \text{RD.T1} \\ \text{RD.T2} \end{bmatrix}$$

The tuning matrices Q, R and P_0^+ are partitioned accordingly, where they form diagonal matrices.

C.3.1 Tuning parameters

Case study 1

$Q^{GS} = \text{diag}[10^3,\ 10^3,\ 10^3,\ 10^3,\ 10^1,\ 10^2,\ 10^3]$

$P_0^{+GS} = \text{diag}[10^4,\ 10^4,\ 10^4,\ 10^4,\ 10^1,\ 10^2,\ 10^6]$

$Q^{sm} = \text{diag}[10^4,\ 10^4,\ 10^4,\ 10^4,\ 10^4,\ 10^4,\ 10^4,\ 10^4,\ 10^1,\ 10^1,\ 10^1,\ 10^6]$

$P_0^{+sm} = \text{diag}[10^3,\ 10^3,\ 10^3,\ 10^3,\ 10^3,\ 10^3,\ 10^3,\ 10^3,\ 10^3,\ 10^3,\ 10^3,\ 10^6]$

$Q^{mm} = \text{diag}\ [10^4,\ 10^3,\ 10^4,\ 10^3,\ 10^3,\ 10^4,\ 10^3,\ 10^2,\ 10^3]$

$P_0^{+mm} = \text{diag}[10^4,\ 10^3,\ 10^4,\ 10^3,\ 10^3,\ 10^4,\ 10^3,\ 10^2,\ 10^{-6}]$

$Q^{RD} = \text{diag}[10^2,\ 10^2]$

$P_0^{+RD} = \text{diag}[10^2,\ 10^2]$

$R^{GS} = \text{diag}[1 \times 10^{-1},\ 1 \times 10^{-1},\ 1 \times 10^{-1},\ 1 \times 10^{-1}]$

$R^{RD} = \text{diag}[1 \times 10^2,\ 1 \times 10^2]$

$R^{mm} = \text{diag}[1 \times 10^2,\ 1 \times 10^{-3}]$

$R^{sm} = \text{diag}\ [1 \times 10^{-3},\ 1 \times 10^{-3},\ 1 \times 10^{-3},\ 1 \times 10^{-3},\ 1 \times 10^{-3}]$

$Q^d = \text{diag}[2 \times 10^5,\ 1 \times 10^2]$

$P_0^{+d} = \text{diag}[2 \times 10^5,\ 1 \times 10^2\ ]$

$A_k^d = \text{diag}[5,\ 5]$

Case study 2

$Q^{GS} = \text{diag}[7 \times 10^3,\ 10^3,\ 10^3,\ 10^3,\ 10^1,\ 10^2,\ 10^3]$

$P_0^{+GS} = \text{diag}[10^4,\ 10^4,\ 10^4,\ 10^4,\ 10^1,\ 10^2,\ 10^6]$

$Q^{sm} = \text{diag}[10^4,\ 10^4,\ 10^4,\ 10^4,\ 10^4,\ 10^4,\ 10^4,\ 10^4,\ 10^1,\ 10^1,\ 10^1,\ 10^6]$

$P_0^{+sm} = \text{diag}[10^3,\ 10^3,\ 10^3,\ 10^3,\ 10^3,\ 10^3,\ 10^3,\ 10^3,\ 10^3,\ 10^3,\ 10^3,\ 10^6]$

$Q^{mm} = \text{diag}\ [10^4,\ 10^3,\ 10^4,\ 10^3,\ 10^3,\ 10^4,\ 10^3,\ 10^2,\ 10^3]$

$P_0^{+mm} = \text{diag}[10^4,\ 10^3,\ 10^4,\ 10^3,\ 10^3,\ 10^4,\ 10^3,\ 10^2,\ 10^{-6}]$

$Q^{RD} = \text{diag}[10^2,\ 10^2]$

$P_0^{+RD} = \text{diag}[10^2,\ 10^2]$

$R^{GS} = \text{diag}[1 \times 10^{-1},\ 1 \times 10^{-1},\ 1 \times 10^{-1},\ 1 \times 10^{-1}]$

$R^{RD} = \text{diag}[1 \times 10^2,\ 1 \times 10^2]$

$R^{mm} = \text{diag}[1 \times 10^{2},\ 1 \times 10^{-3}]$

$R^{sm} = \text{diag}\ [1 \times 10^{-3},\ 1 \times 10^{-3},\ 1 \times 10^{-3},\ 1 \times 10^{-3},\ 1 \times 10^{-3}]$

$Q^{d} = \text{diag}\ [1 \times 10^{2},\ 1 \times 10^{4},\ 1 \times 10^{4},\ 5 \times 10^{3},\ 2 \times 10^{5}]$

${P_0^+}^{d} = \text{diag}[1 \times 10^{2},\ 6 \times 10^{5},\ 1 \times 10^{4},\ 5 \times 10^{4},\ 2 \times 10^{5}]$

$A_k^d = \text{diag}[2,\ 2,\ 6,\ 2,\ 6]$

C.3.2 Constraints

The lower (LB) and upper (UB) bounds enforced on the states are shown below, in which they are partitioned according to the x vector represented previously.

$LB^{GS} = [0,\ 0,\ 0,\ 0,\ 1 \times 10^{-6},\ 298\ -4 \times 10^{9}]^{T}$

$LB^{mm} = [0,\ 0,\ 0,\ 0,\ 0,\ 0,\ 0,\ 1500,\ 0]^{T}$

$LB^{RD} = [273,\ 273]^{T}$

$LB^{sm} = [0,\ 0,\ 0,\ 0,\ 0,\ 0,\ 0,\ 0,\ 0,\ 0,\ 0,\ -5 \times 10^{9}]^{T}$

$$UB^{GS} = \begin{bmatrix} 5 \times 10^{4} \\ 1.2 \times 10^{5} \\ 1 \times 10^{5} \\ 2 \times 10^{5} \\ 2 \times 10^{4} \\ 1809 \\ -2572.0261 \end{bmatrix} \quad UB^{mm} = \begin{bmatrix} 3 \times 10^{4} \\ 5 \times 10^{4} \\ 3 \times 10^{7} \\ 1.5 \times 10^{4} \\ 100 \\ 4 \times 10^{5} \\ 1.2 \times 10^{5} \\ 3000 \\ 6 \times 10^{5} \end{bmatrix} \quad UB^{sm} = \begin{bmatrix} 5 \times 10^{4} \\ 7 \times 10^{5} \\ 8 \times 10^{4} \\ 5 \times 10^{3} \\ 3 \times 10^{5} \\ 5 \times 10^{4} \\ 2 \times 10^{4} \\ 6 \times 10^{5} \\ 2 \times 10^{4} \\ 6 \times 10^{3} \\ 2 \times 10^{4} \\ -1354371.4 \end{bmatrix}$$

$$UB^{RD} = \begin{bmatrix} 5.8 \times 10^2 \\ 5.8 \times 10^2 \end{bmatrix}$$

C.3.3 Initial Conditions

Actual initial conditions

$x_0{}^{GS} = [5,\ 200,\ 5,\ 1000,\ 0,\ 300,\ -2572.0261]^T$

$x_0{}^{mm} = [450,\ 0,\ 163 \times 10^3,\ 147.439,\ 0,\ 32.044,\ 2151,\ 1809,\ 53982.4]^T$

$x_0{}^{RD} = [500,\ 500]^T$

$x_0{}^{sm} = [10,\ 2000,\ 2000,\ 50,\ 300,\ 200,\ 90,\ 1000,\ 0,\ 0,\ 0,\ -1354371.4]^T$

Case study 1

$x_0^{+GS} = [6,\ 240,\ 10,\ 1200,\ 2,\ 360,\ -3086.43]^T$

$x_0^{+mm} = [540,\ 2,\ 162.4 \times 10^3,\ 177,\ 2,\ 38,\ 2580,\ 1750,\ 53962.4]^T$

$x_0^{+RD} = [440,\ 440]^T$

$x_0^{+sm} = [12,\ 2200,\ 2200,\ 60,\ 360,\ 240,\ 108,\ 1200,\ 2,\ 2,\ 2,\ -1625245.7]^T$

$x_0^{+d} = [0,\ 0]^T$

Case study 2

$x_0^{+GS} = [6,\ 240,\ 10,\ 1200,\ 2,\ 360,\ -3086.43]^T$

$x_0^{+mm} = [540,\ 2,\ 162.4 \times 10^3,\ 177,\ 2,\ 38,\ 2580,\ 1750,\ 53962.4]^T$

$x_0^{+RD} = [440,\ 440]^T$

$x_0^{+sm} = [12,\ 2200,\ 2200,\ 60,\ 360,\ 240,\ 108,\ 1200,\ 2,\ 2,\ 2,\ -1625245.7]^T$

$x_0^{+d} = [0,\ 0,\ 0,\ 0,\ 0]^T$

C.4 EKF Trajectories

C.4.1 Case Study 1

Case 1A: Base case (no stochastic disturbances added)

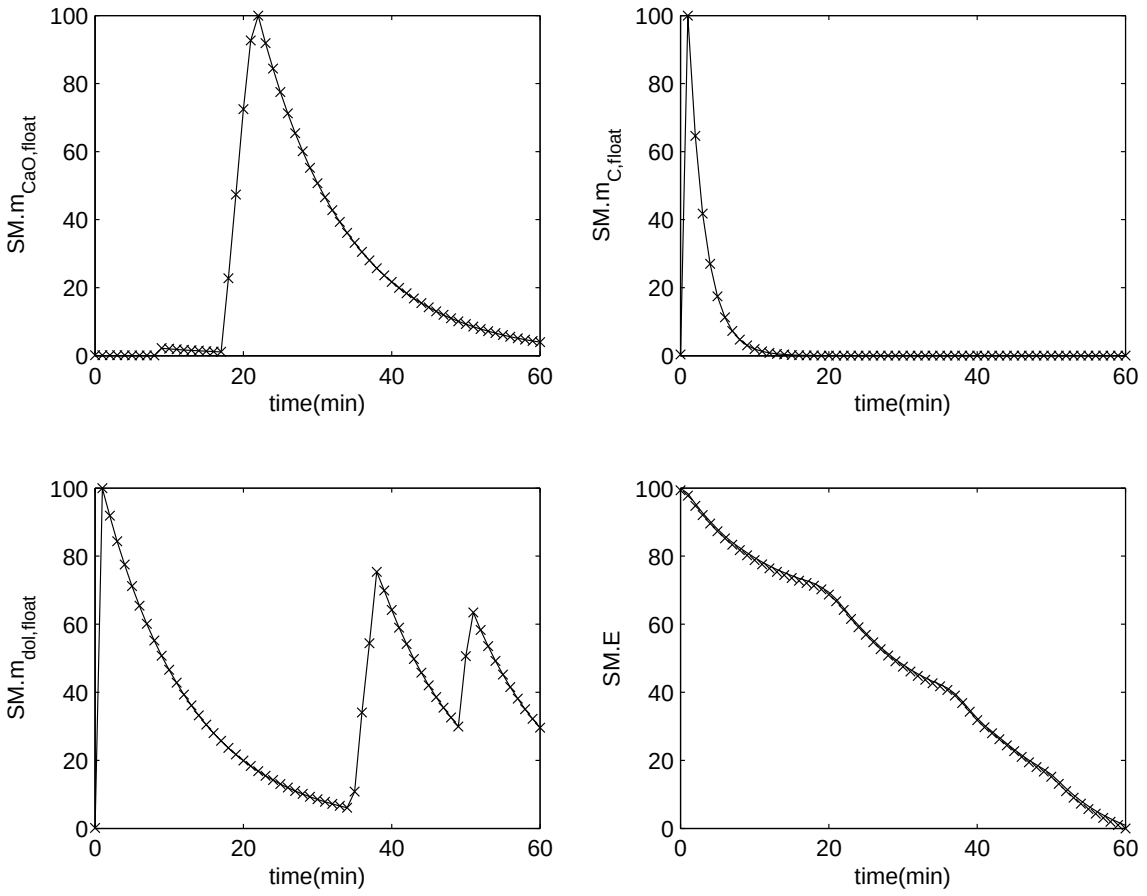

Figure C.1: Slag zone state profiles for the base case (Case Study 1A) without disturbance state augmentation. (×) represents the estimated states while (–) represents the actual states

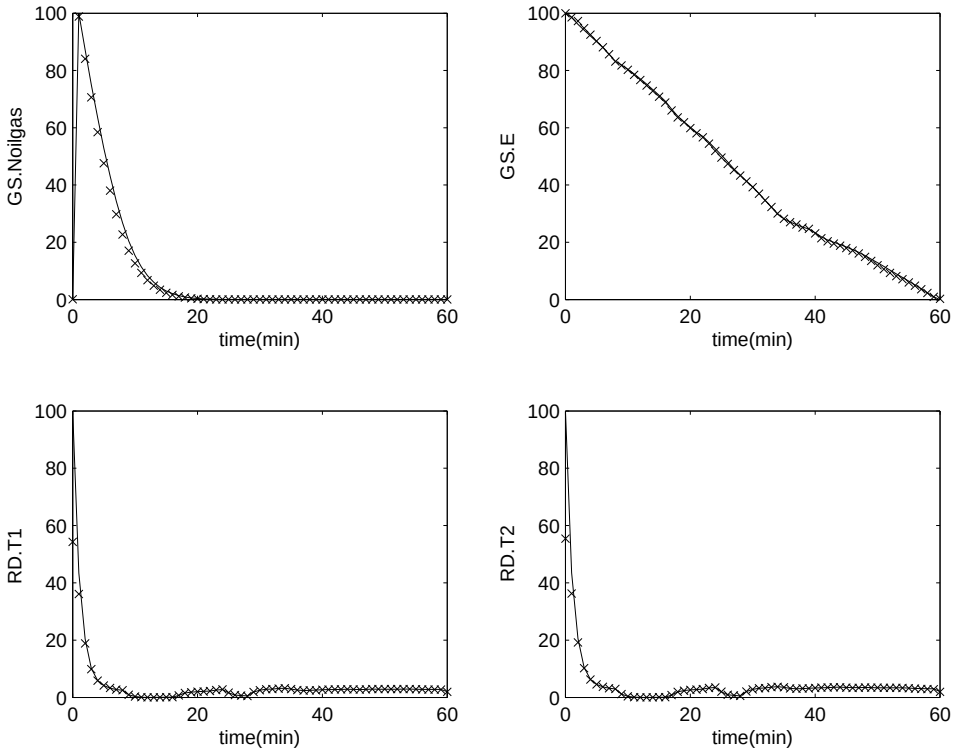

Figure C.2: Gas zone state profiles for the base case (Case Study 1A) without disturbance state augmentation. (×) represents the estimated states while (–) represents the actual states

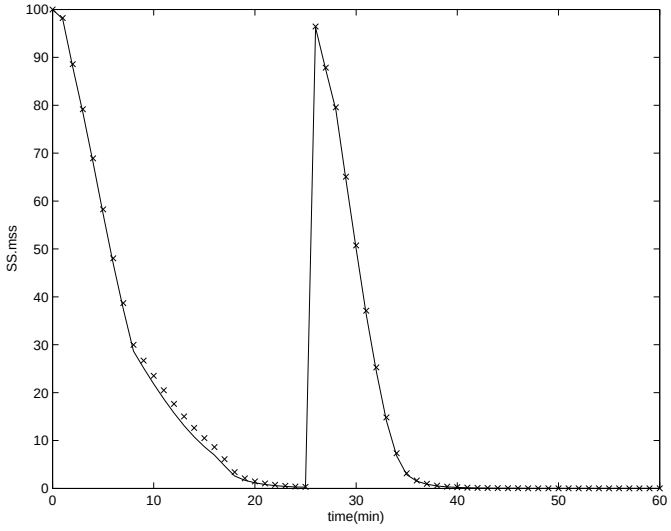

Figure C.3: Solid zone state profiles for the base case (Case Study 1A) without disturbance state augmentation. (×) represents the estimated states while (–) represents the actual states

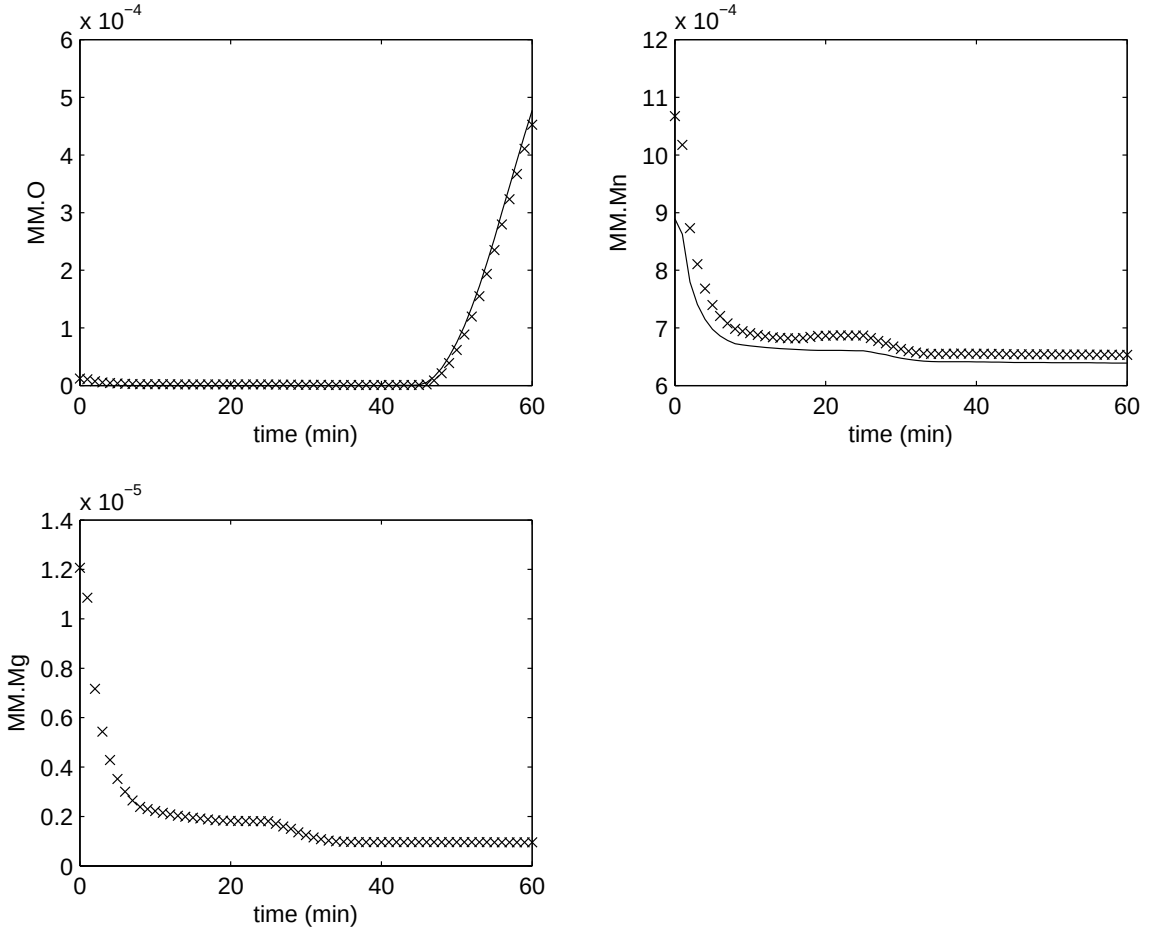

Figure C.4: Molten metal zone state profiles for the base case (Case Study 1A) without disturbance state augmentation. (×) represents the estimated states while (–) represents the actual states

Case 1B: Augmented disturbances

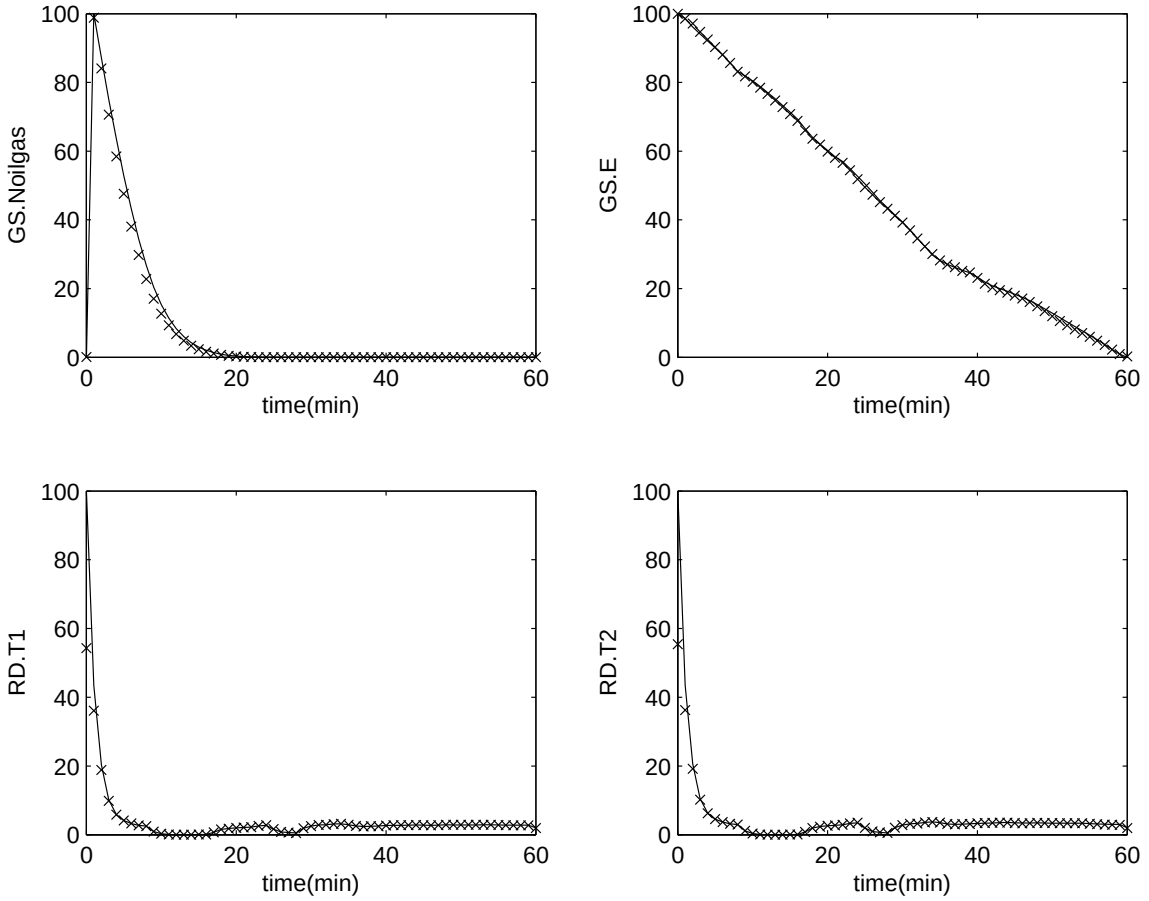

Figure C.5: Gas zone state profiles for Case Study 1B with disturbance state augmentation. (×) represents the estimated states while (–) represents the actual states

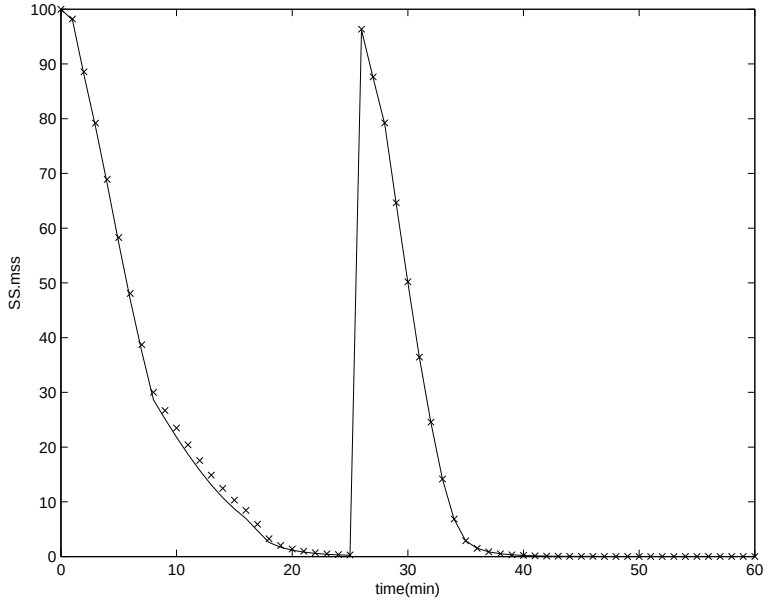

Figure C.6: Solid zone state profiles for Case Study 1B with disturbance state augmentation. (×) represents the estimated states while (–) represents the actual states

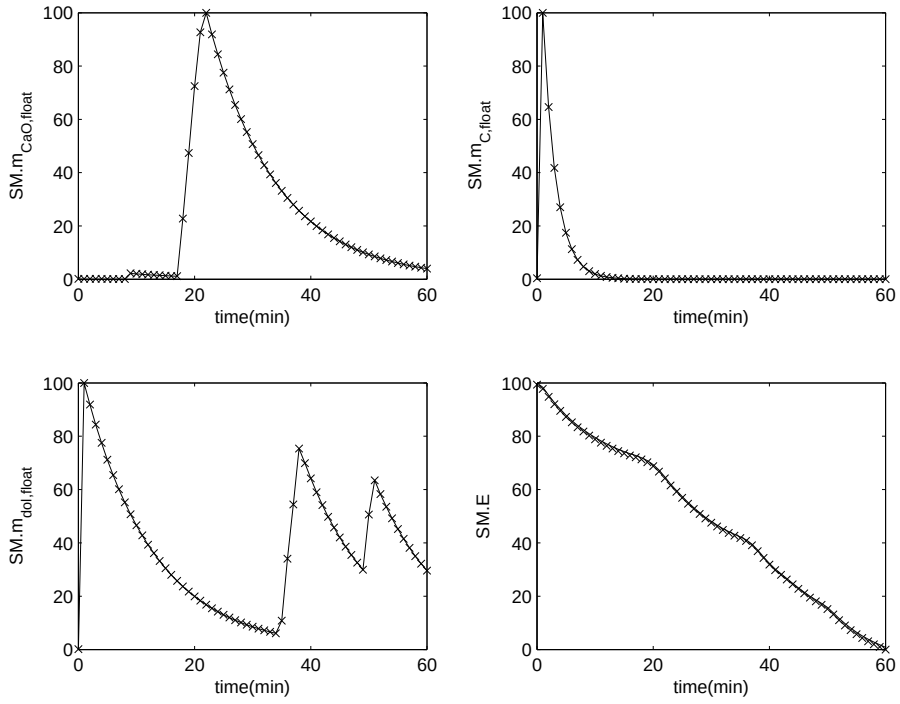

Figure C.7: Slag zone state profiles for Case Study 1B with disturbance state augmentation. (×) represents the estimated states while (–) represents the actual states

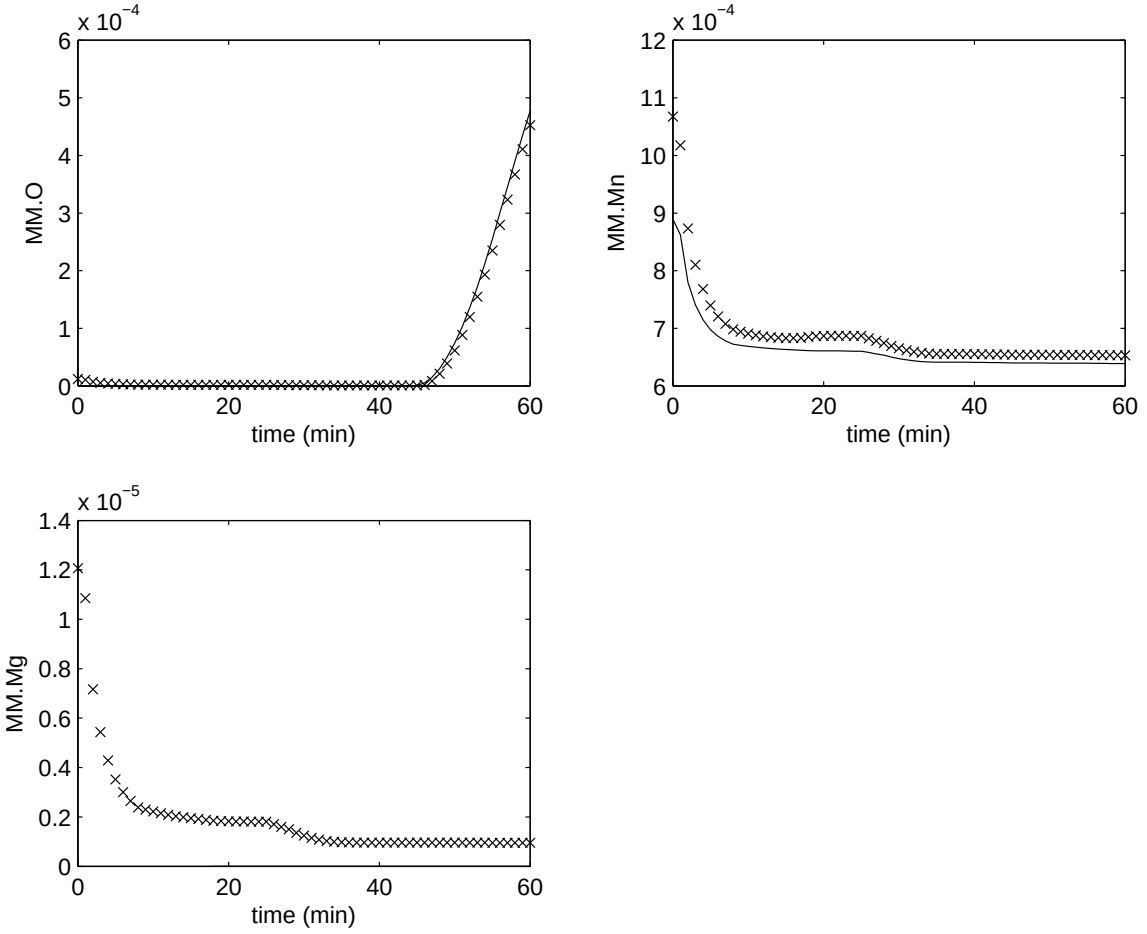

Figure C.8: Molten metal zone state profiles for Case Study 1B with disturbance state augmentation. (×) represents the estimated states while (–) represents the actual states

C.4.2 Frequent molten metal temperature measurements on Case Study 1

Case Study 1A

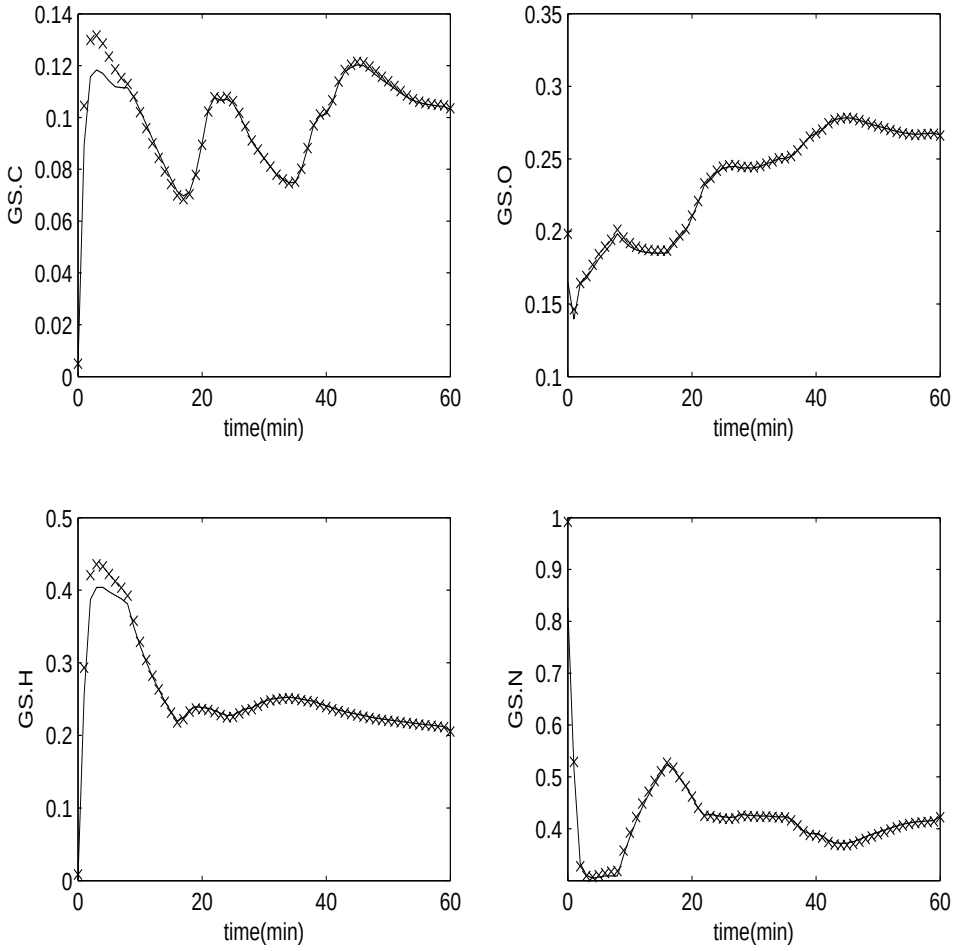

Figure C.9: Gas zone state profiles for the base case (Case Study 1A) without disturbance state augmentation using frequent MM.T measurements. (×) represents the estimated states while (–) represents the actual states

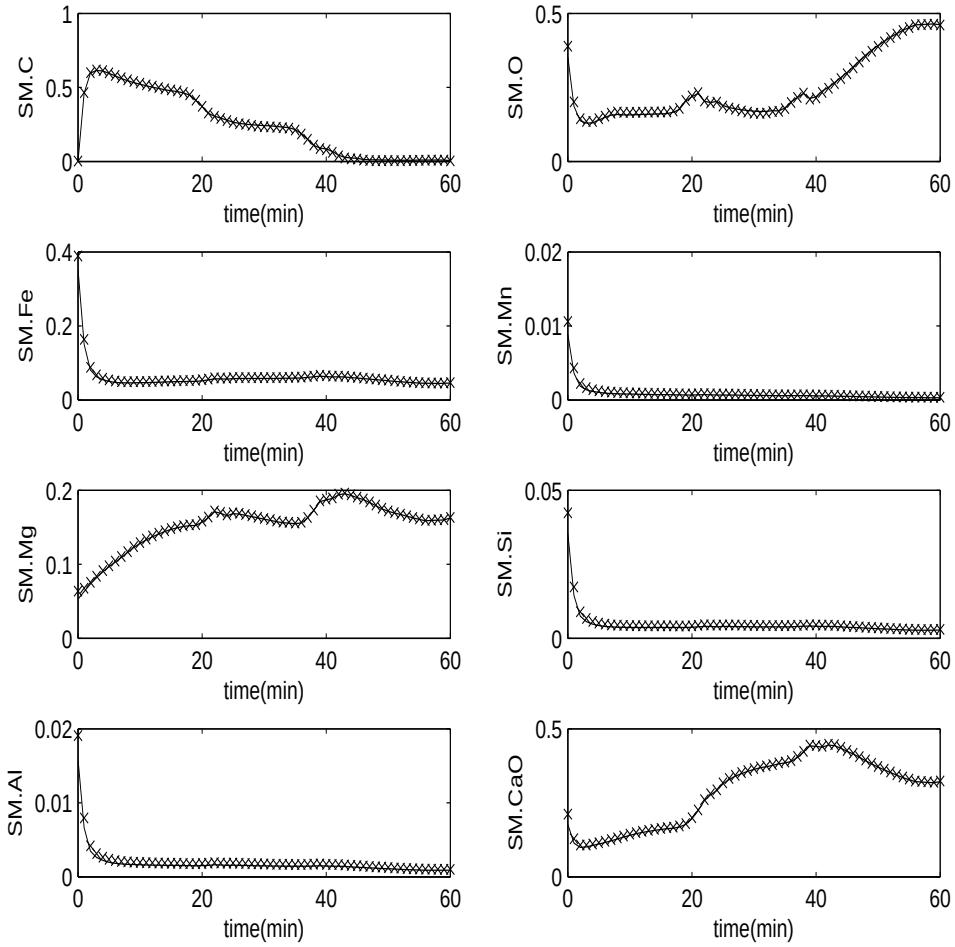

Figure C.10: Slag zone state profiles for the base case (Case Study 1A) without disturbance state augmentation using frequent MM.T measurements. (×) represents the estimated states while (–) represents the actual states

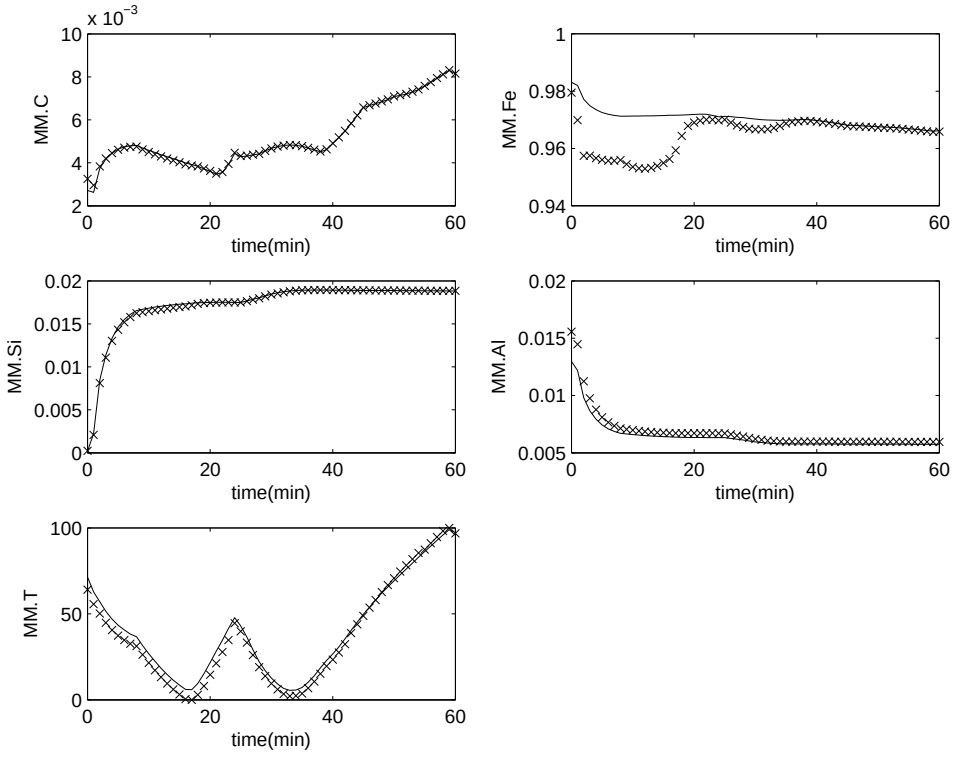

Figure C.11: Molten metal zone state profiles for the base case (Case Study 1A) without disturbance state augmentation using frequent MM.T measurements. (×) represents the estimated states while (–) represents the actual states

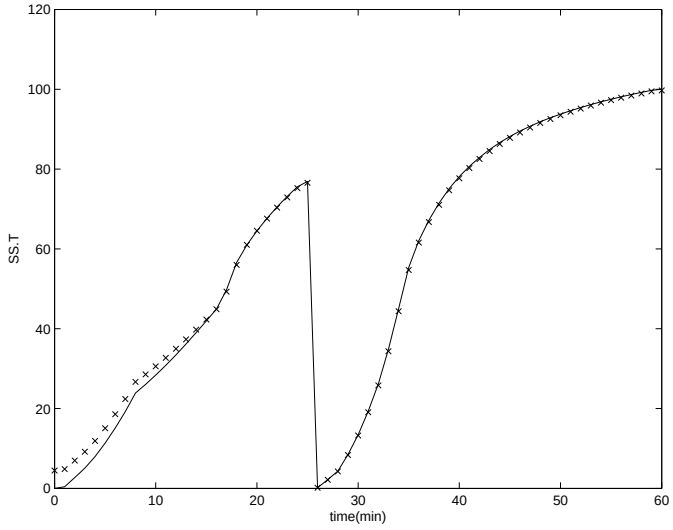

Figure C.12: Solid zone state profiles for the base case (Case Study 1A) without disturbance state augmentation using frequent MM.T measurements. (×) represents the estimated states while (–) represents the actual states

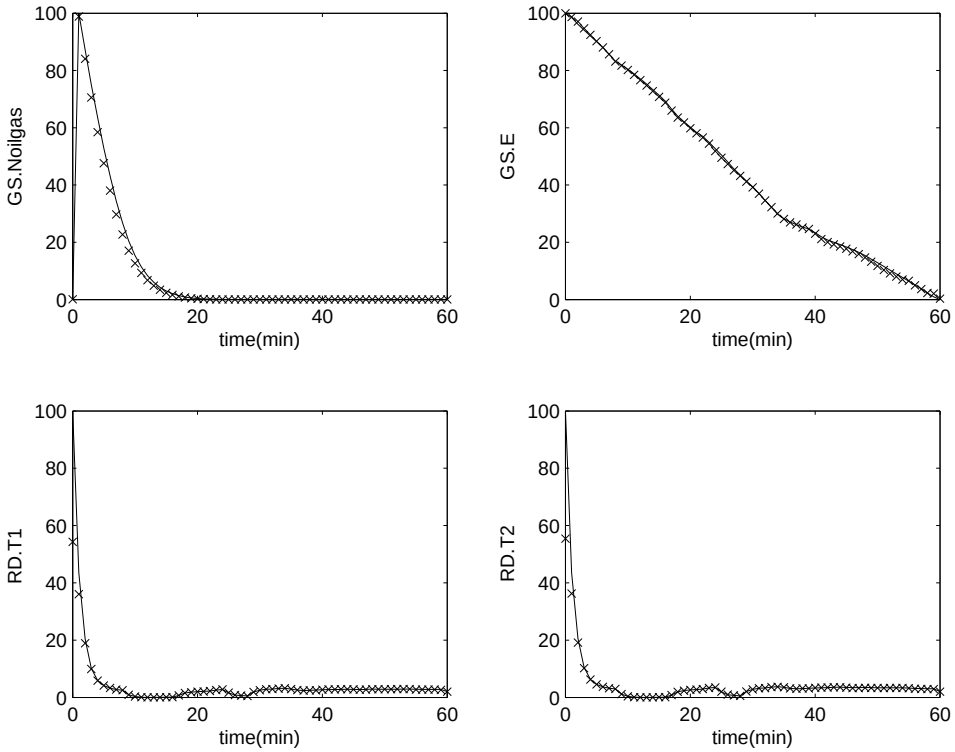

Figure C.13: Gas zone state profiles for the base case (Case Study 1A) without disturbance state augmentation using frequent MM.T measurements. (×) represents the estimated states while (–) represents the actual states

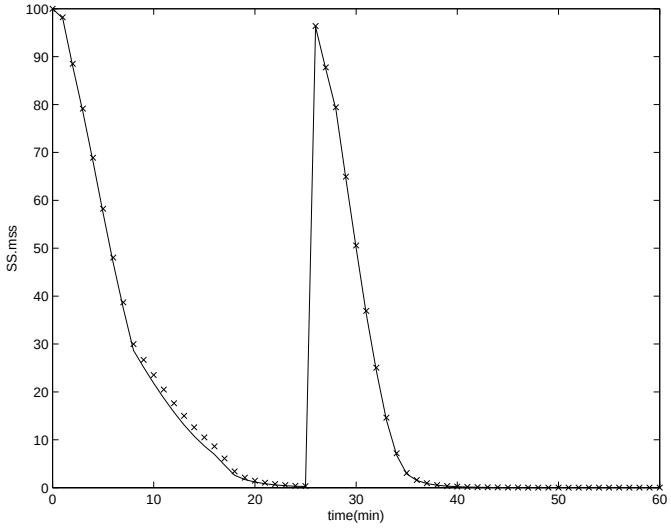

Figure C.14: Solid zone state profiles for the base case (Case Study 1A) without disturbance state augmentation using frequent MM.T measurements. (×) represents the estimated states while (–) represents the actual states

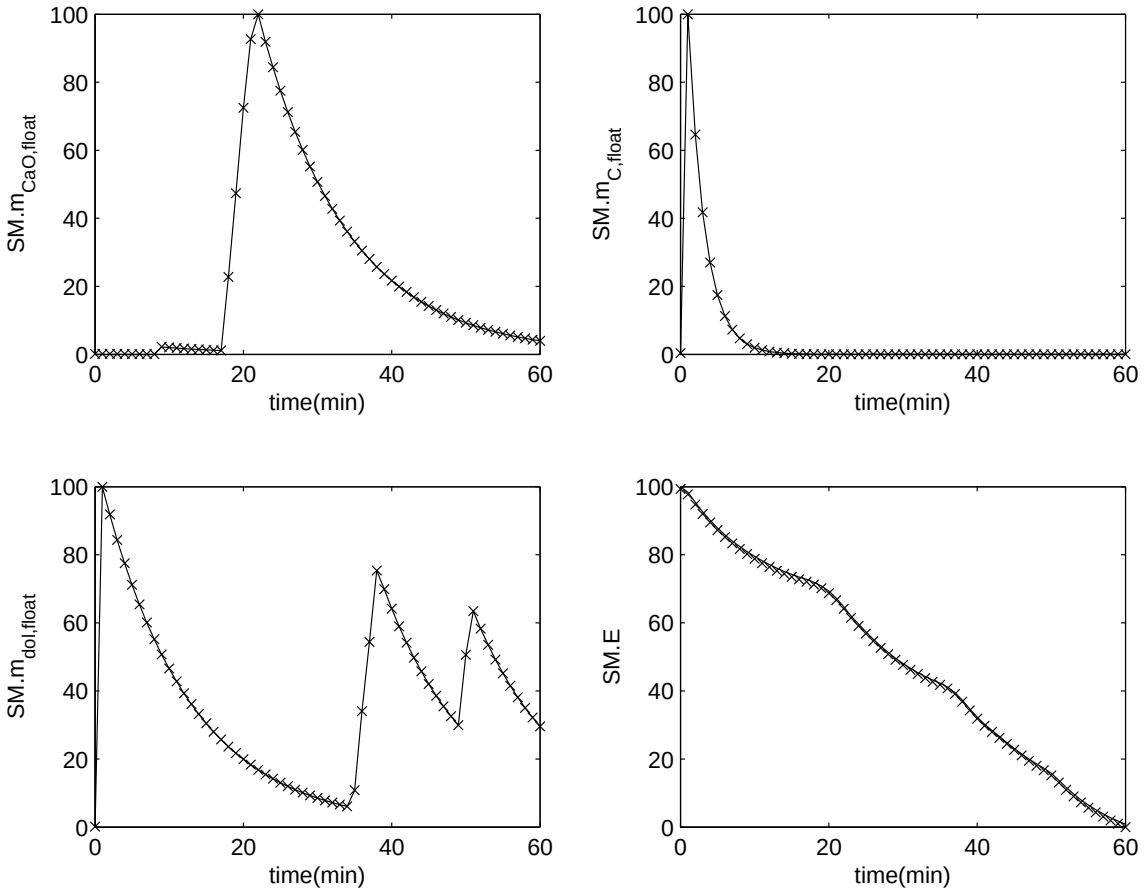

Figure C.15: Slag zone state profiles for the base case (Case Study 1A) without disturbance state augmentation using frequent MM.T measurements. (×) represents the estimated states while (–) represents the actual states

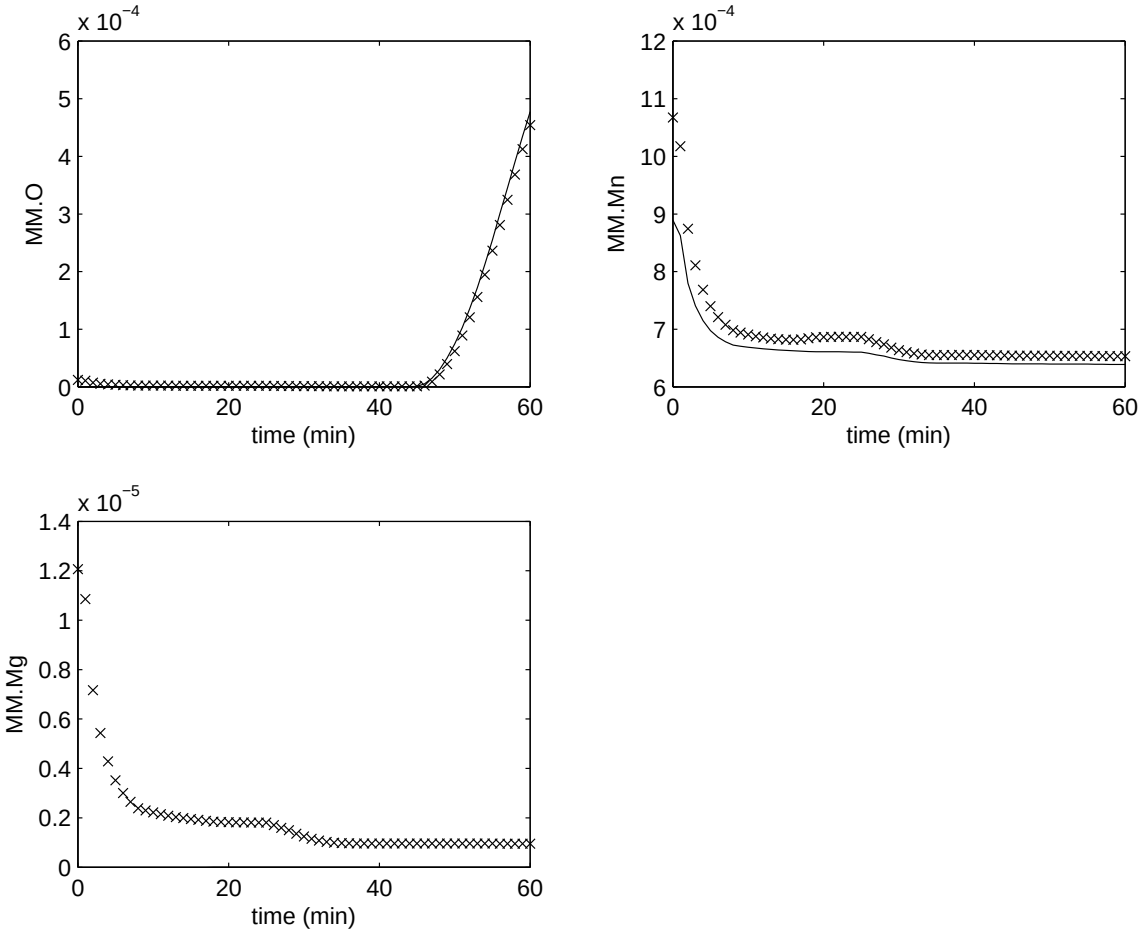

Figure C.16: Molten metal zone state profiles for the base case (Case Study 1A) without disturbance state augmentation using frequent MM.T measurements. (×) represents the estimated states while (–) represents the actual states

Case Study 1B

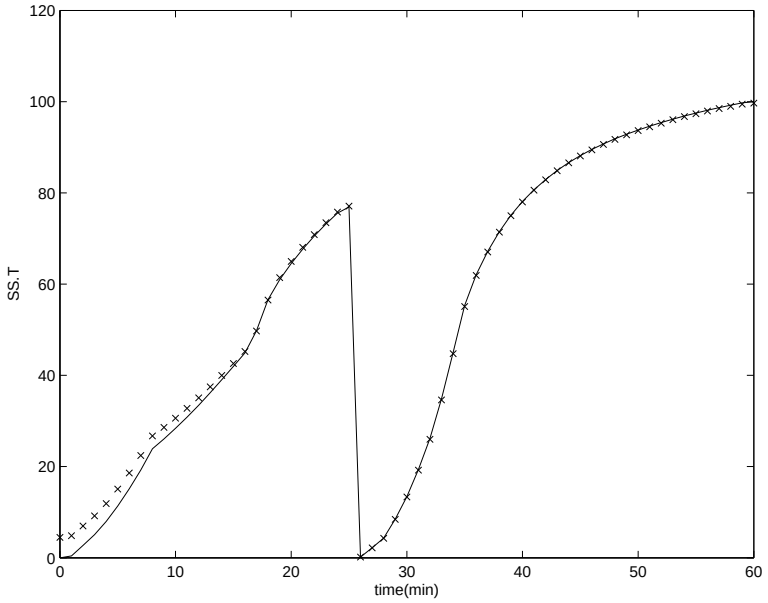

Figure C.17: Solid zone state profiles for Case Study 1B with disturbance state augmentation using frequent MM.T measurements. (×) represents the estimated states while (–) represents the actual states

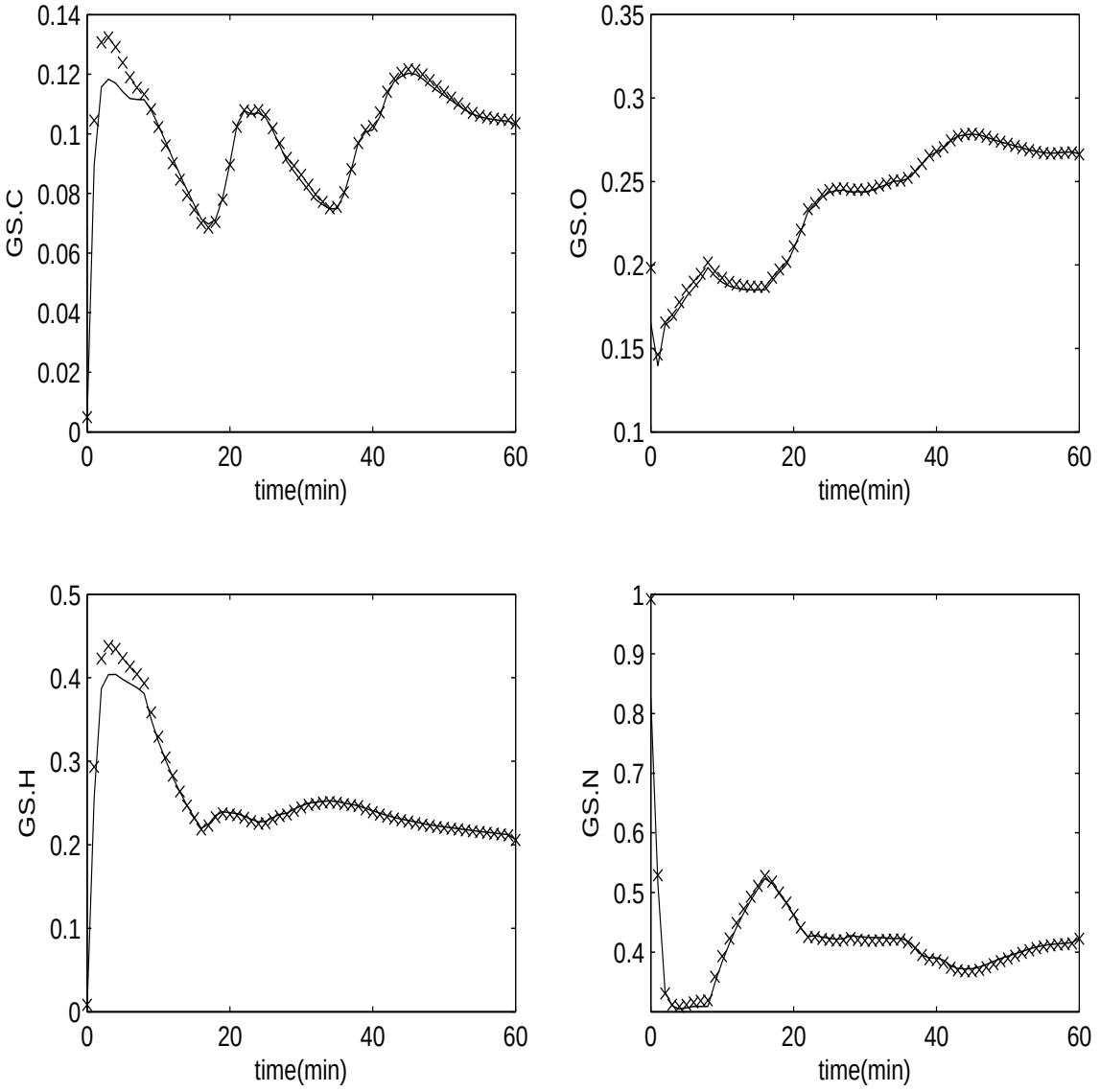

Figure C.18: Gas zone state profiles for Case Study 1B with disturbance state augmentation using frequent MM.T measurements. (×) represents the estimated states while (–) represents the actual states

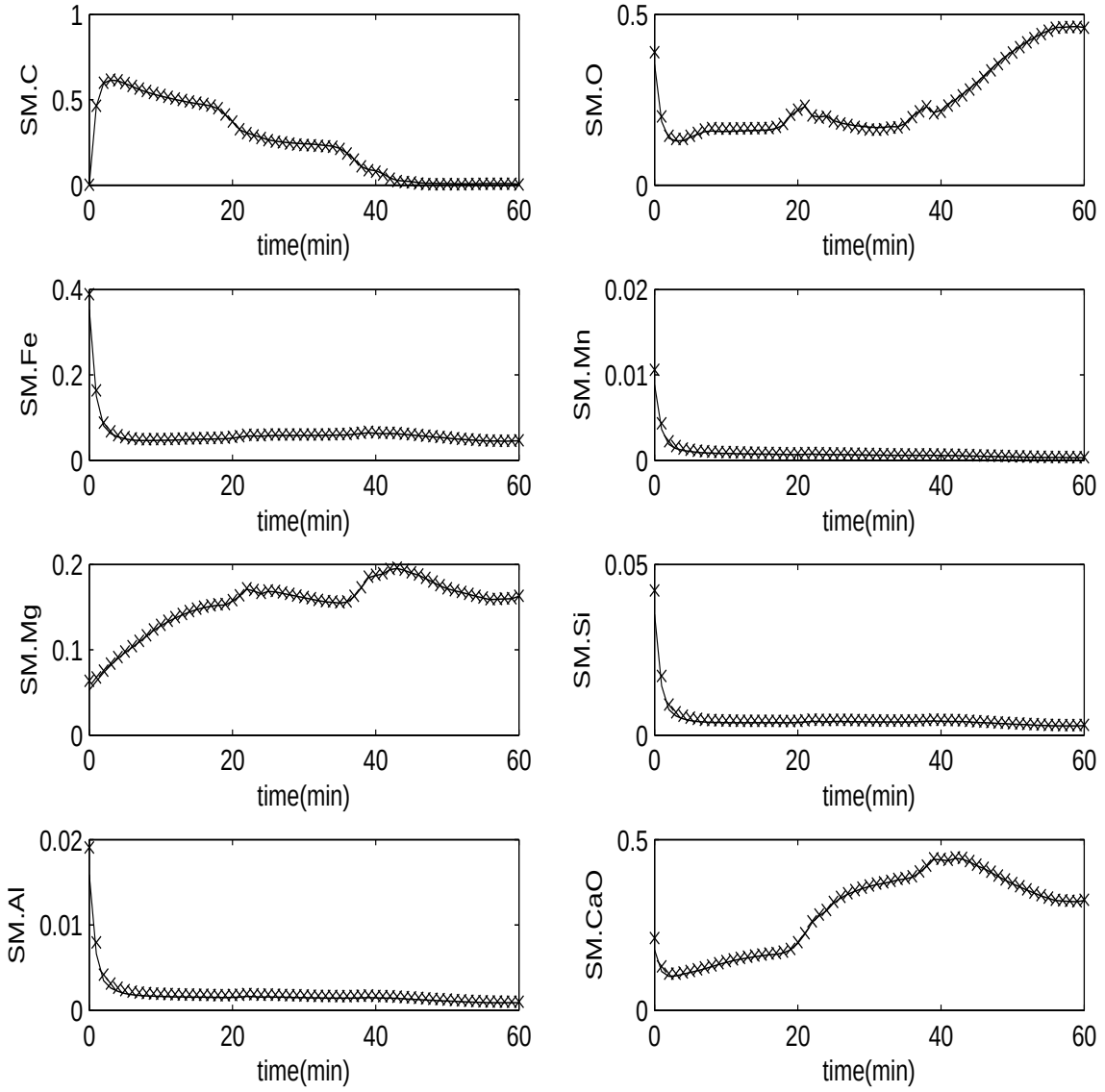

Figure C.19: Slag zone state profiles for Case Study 1B with disturbance state augmentation using frequent MM.T measurements. (×) represents the estimated states while (–) represents the actual states

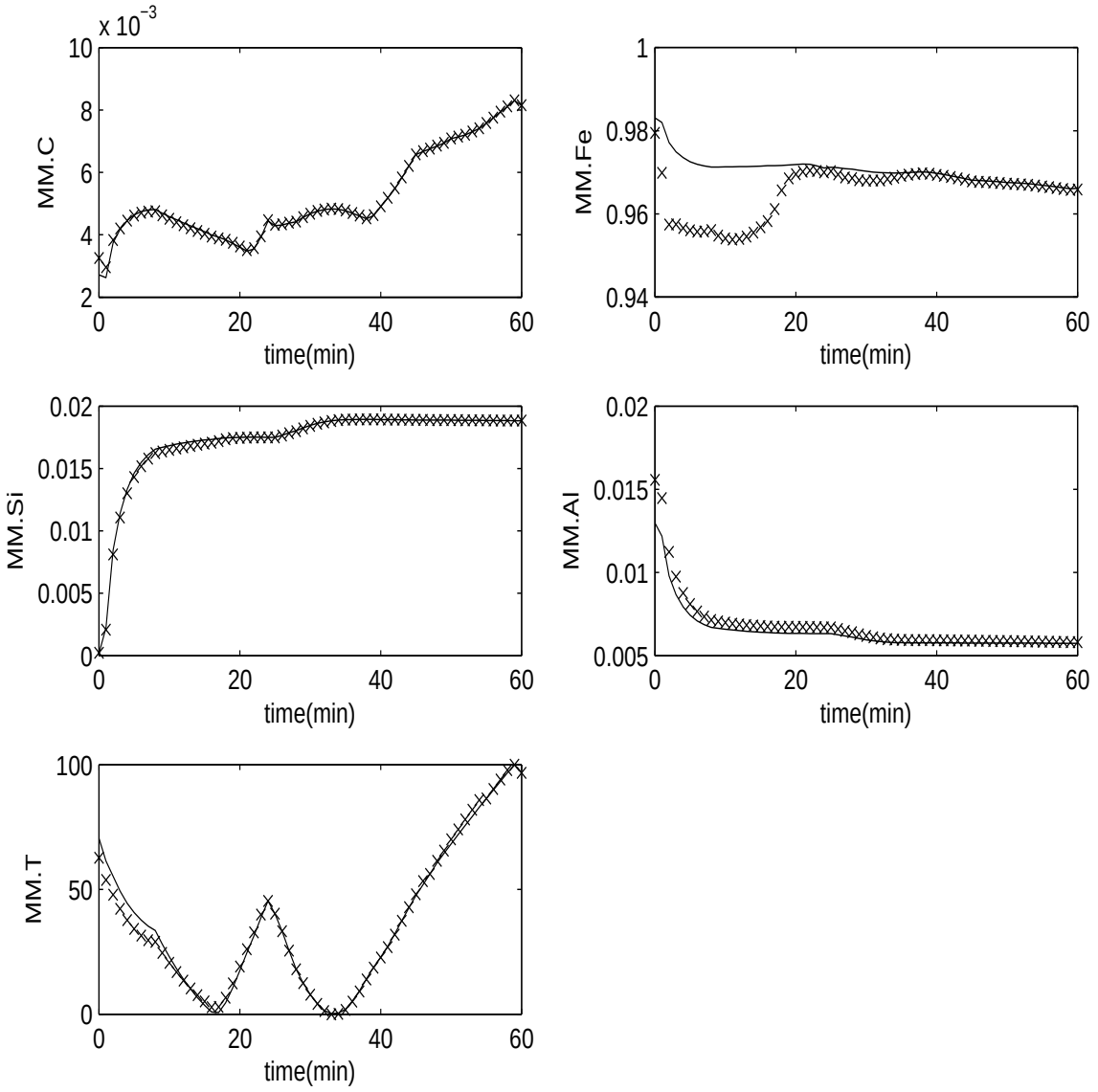

Figure C.20: Molten metal zone state profiles for Case Study 1B with disturbance state augmentation using frequent MM.T measurements. (×) represents the estimated states while (–) represents the actual states

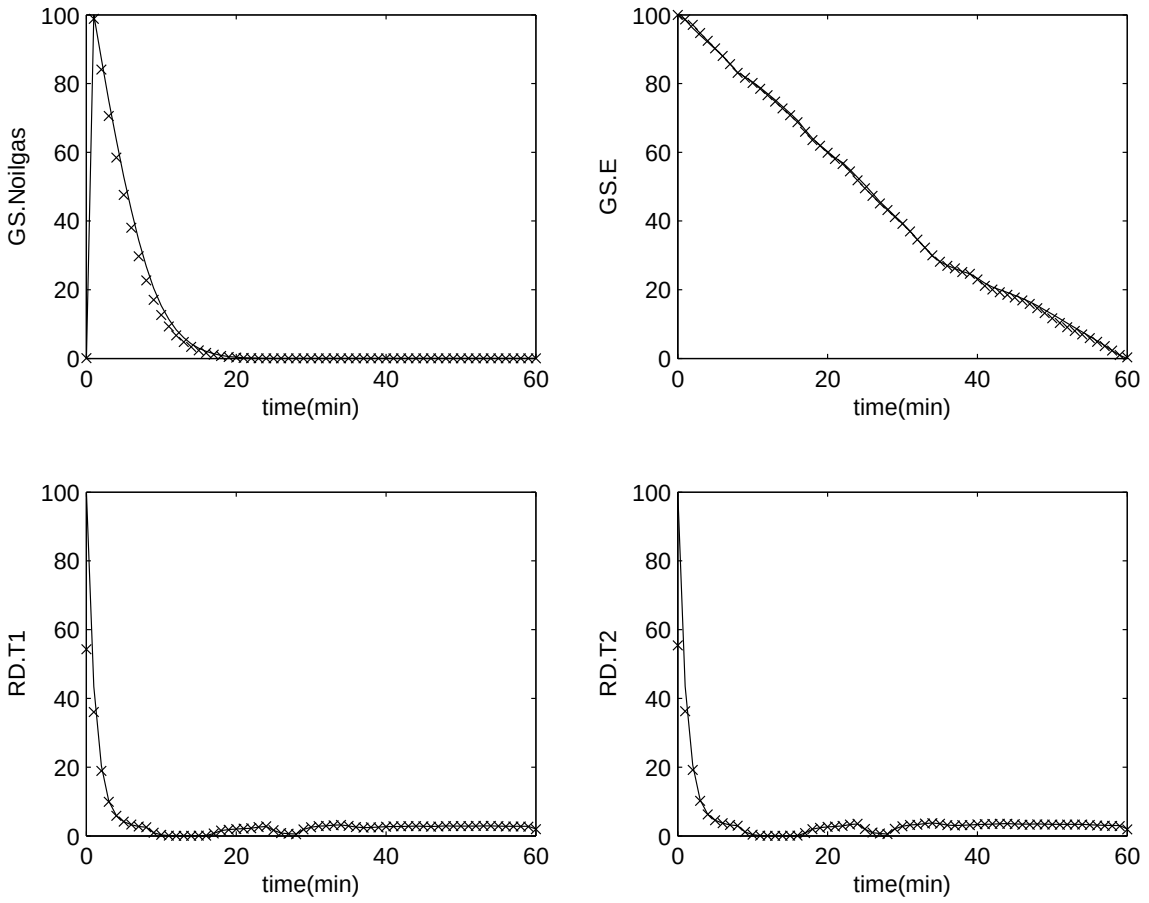

Figure C.21: Gas zone state profiles for Case Study 1B with disturbance state augmentation using frequent MM.T measurements. (×) represents the estimated states while (–) represents the actual states

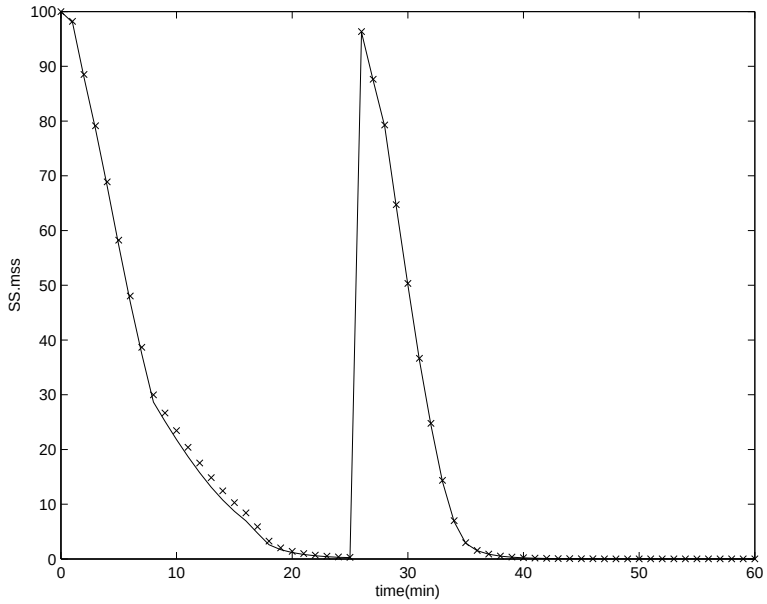

Figure C.22: Solid zone state profiles for Case Study 1B with disturbance state augmentation using frequent MM.T measurements. (×) represents the estimated states while (–) represents the actual states

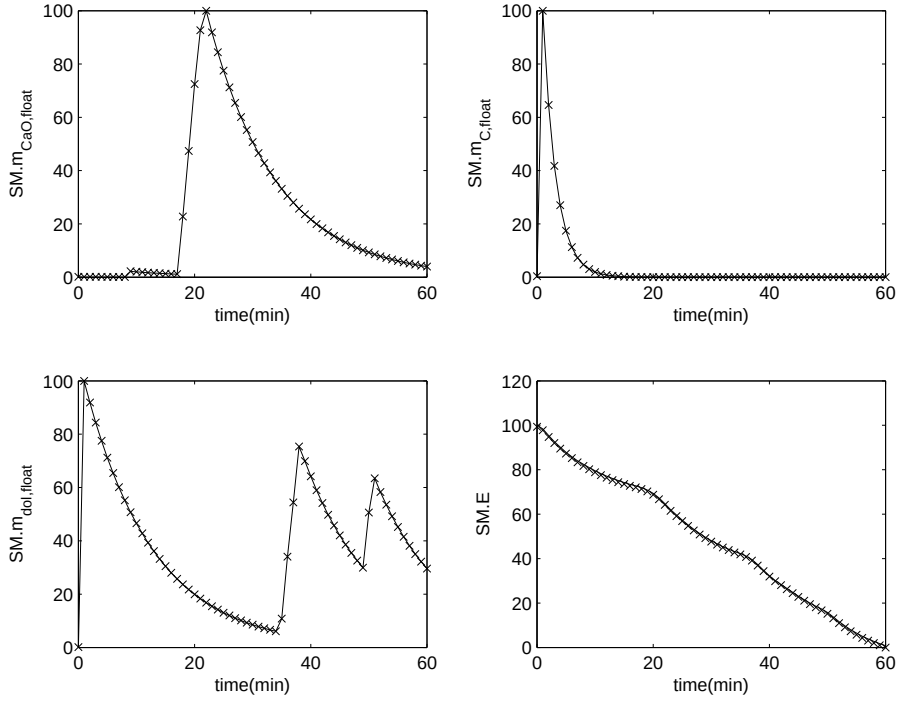

Figure C.23: Slag zone state profiles for Case Study 1B with disturbance state augmentation using frequent MM.T measurements. (×) represents the estimated states while (–) represents the actual states

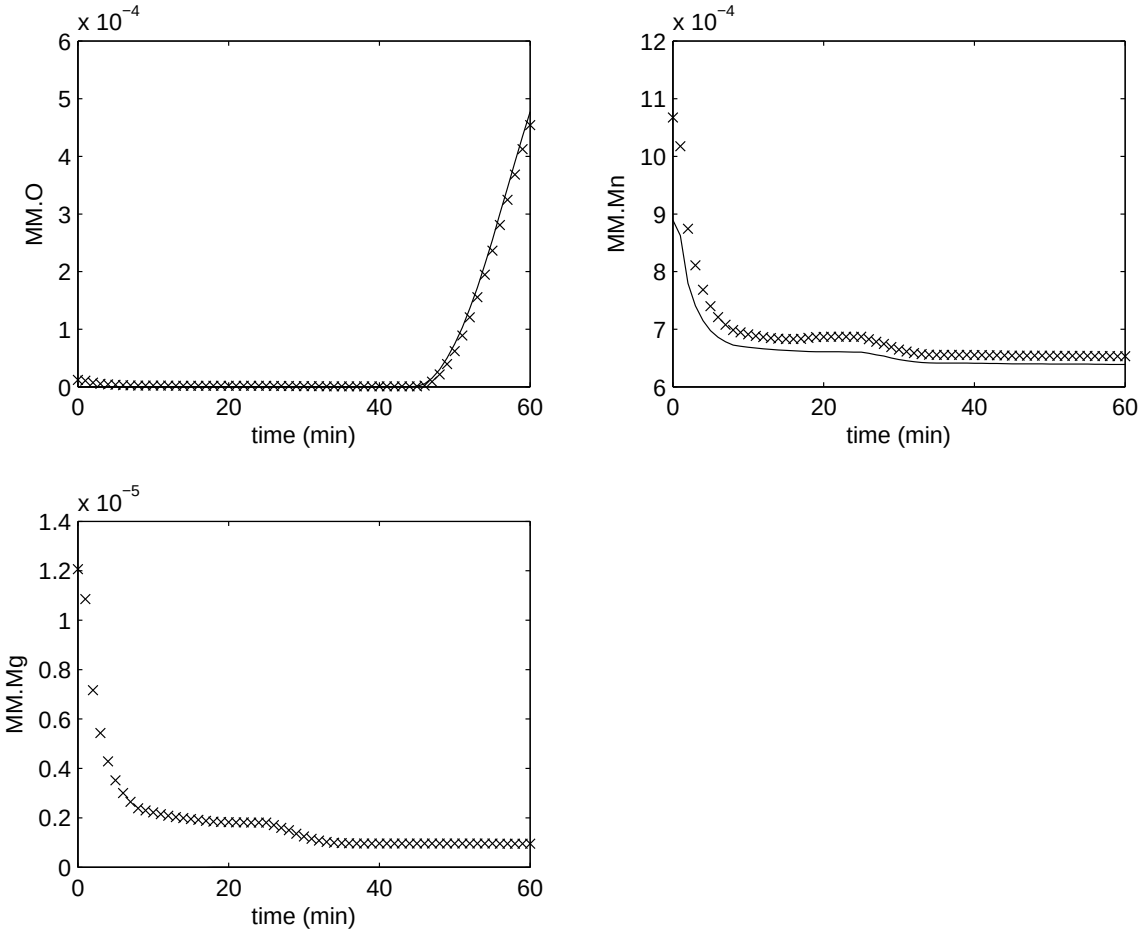

Figure C.24: Molten metal zone state profiles for Case Study 1B with disturbance state augmentation using frequent MM.T measurements. (×) represents the estimated states while (–) represents the actual states

C.4.3 Case Study 2

Case 2A: Base case (no stochastic disturbances added)

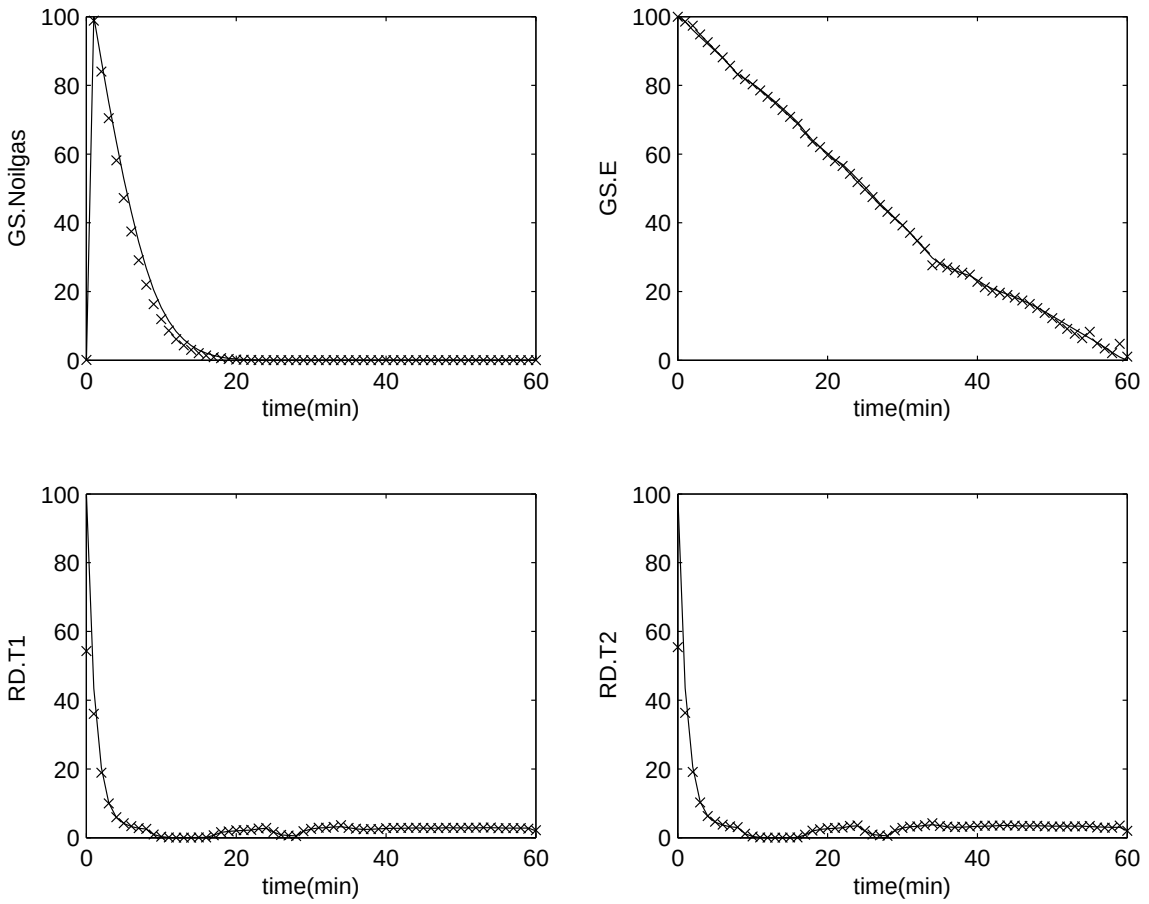

Figure C.25: Gas zone state profiles for the Case Study 2A without disturbance state augmentation. (×) represents the estimated states while (–) represents the actual states

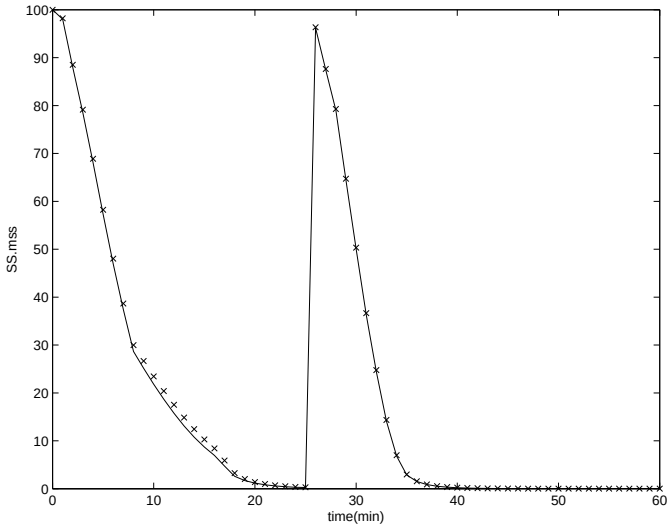

Figure C.26: Solid zone state profiles for Case Study 2A with disturbance state augmentation. (×) represents the estimated states while (–) represents the actual states

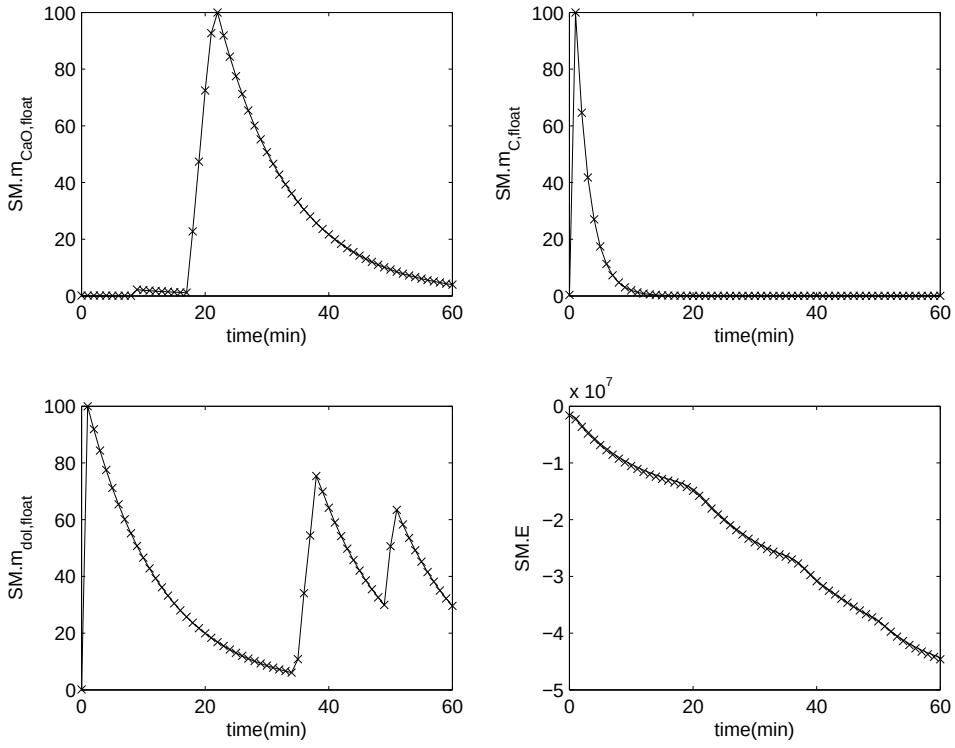

Figure C.27: Slag zone state profiles for the Case study 2A without disturbance state augmentation. (×) represents the estimated states while (–) represents the actual states

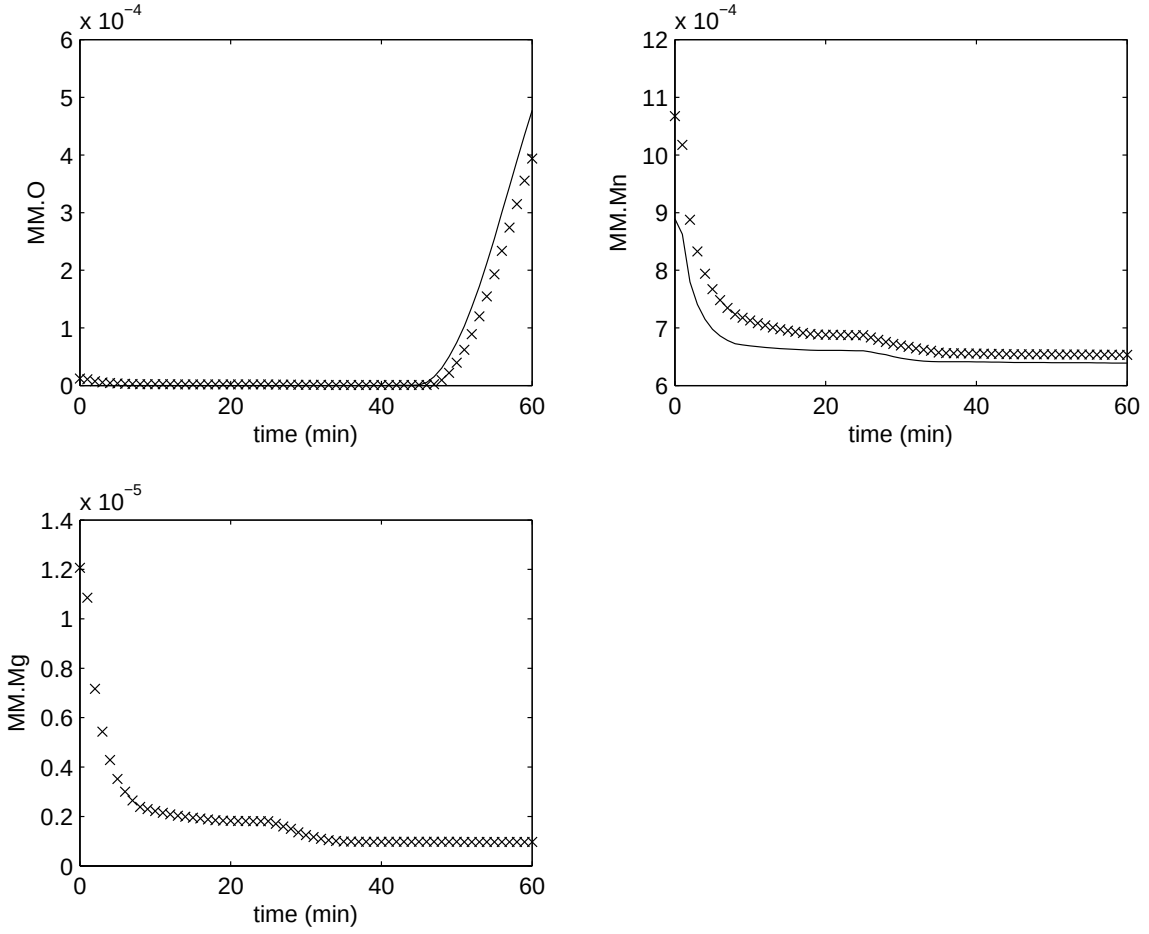

Figure C.28: Molten metal zone state profiles for the Case study 2A without disturbance state augmentation. (×) represents the estimated states while (–) represents the actual states

Case 2B: Augmented disturbances

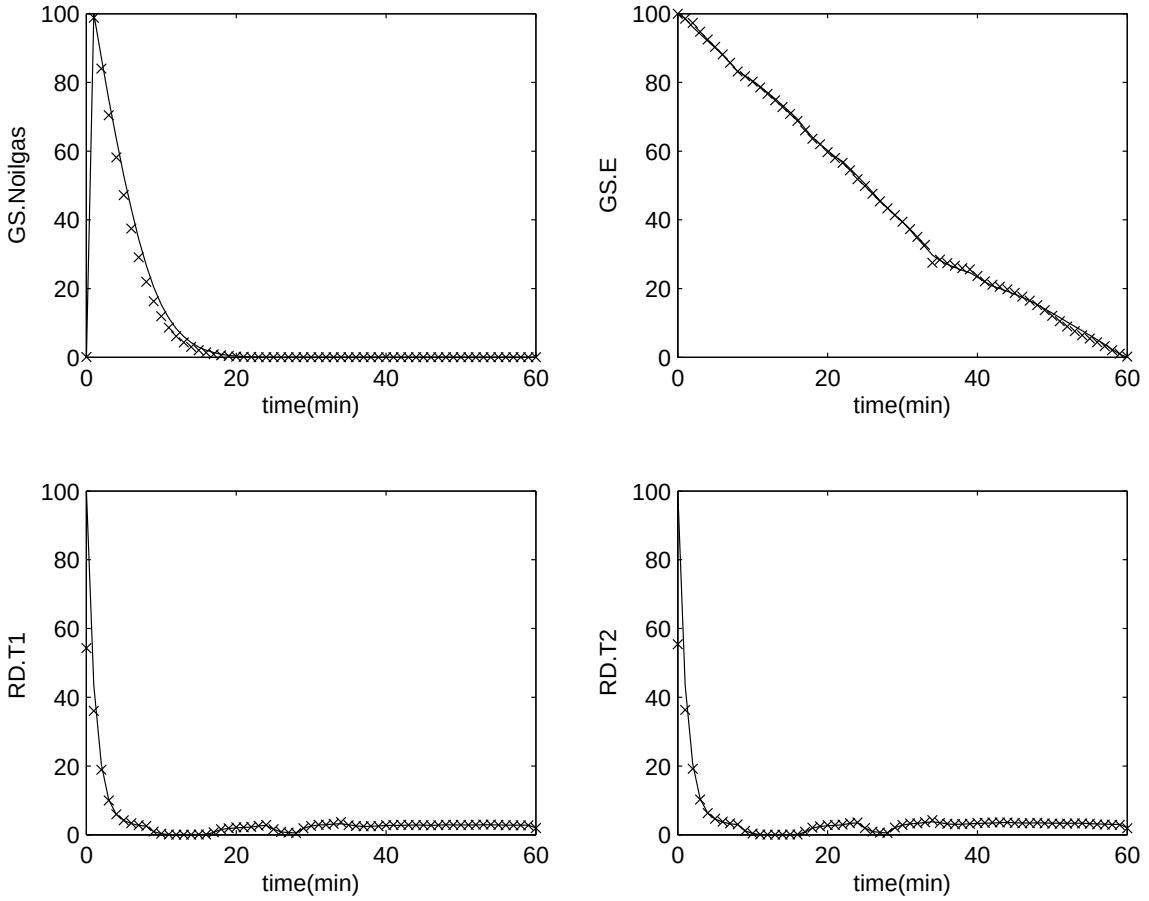

Figure C.29: Gas zone state profiles for the Case Study 2B with disturbance state augmentation. (×) represents the estimated states while (–) represents the actual states

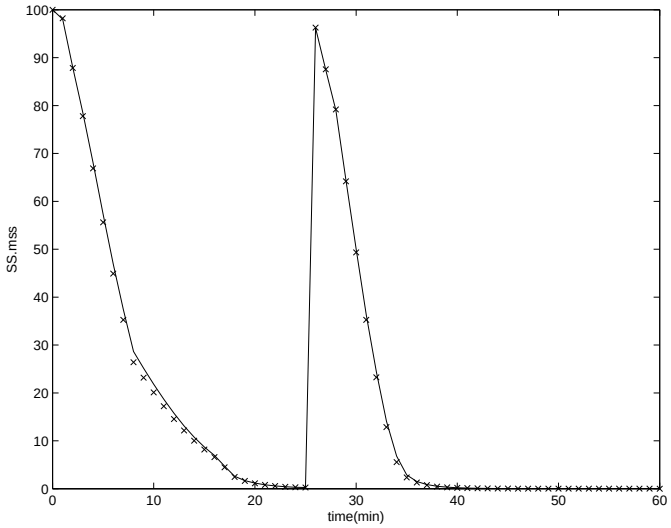

Figure C.30: Solid zone state profiles for the Case Study 2B with disturbance state augmentation. (×) represents the estimated states while (–) represents the actual states

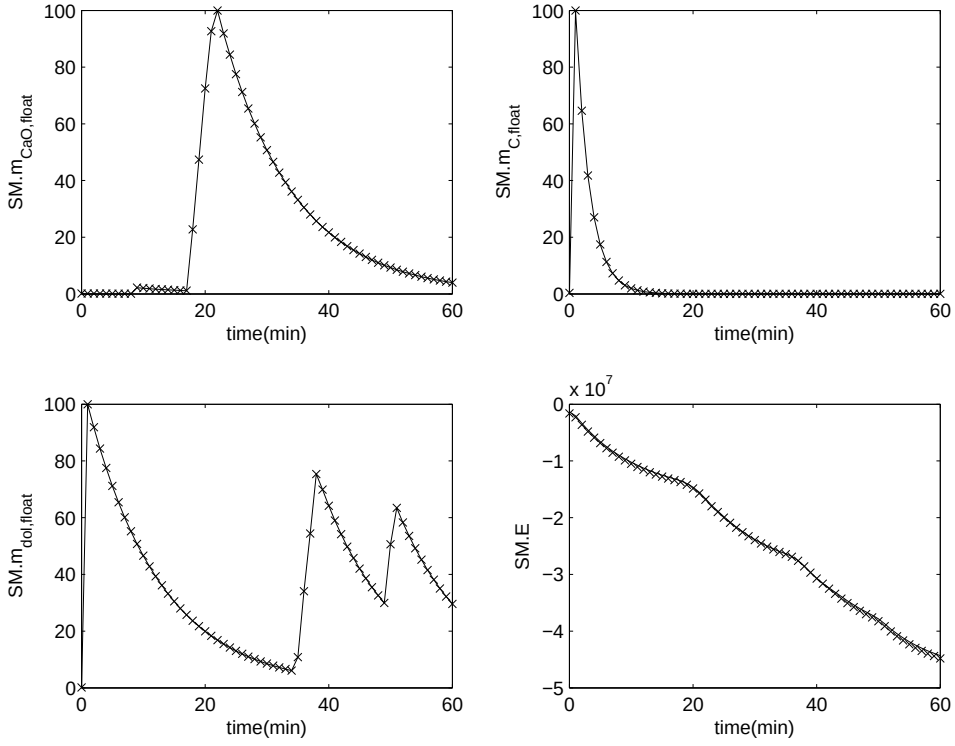

Figure C.31: Slag zone state profiles for the Case Study 2B with disturbance state augmentation. (×) represents the estimated states while (–) represents the actual states

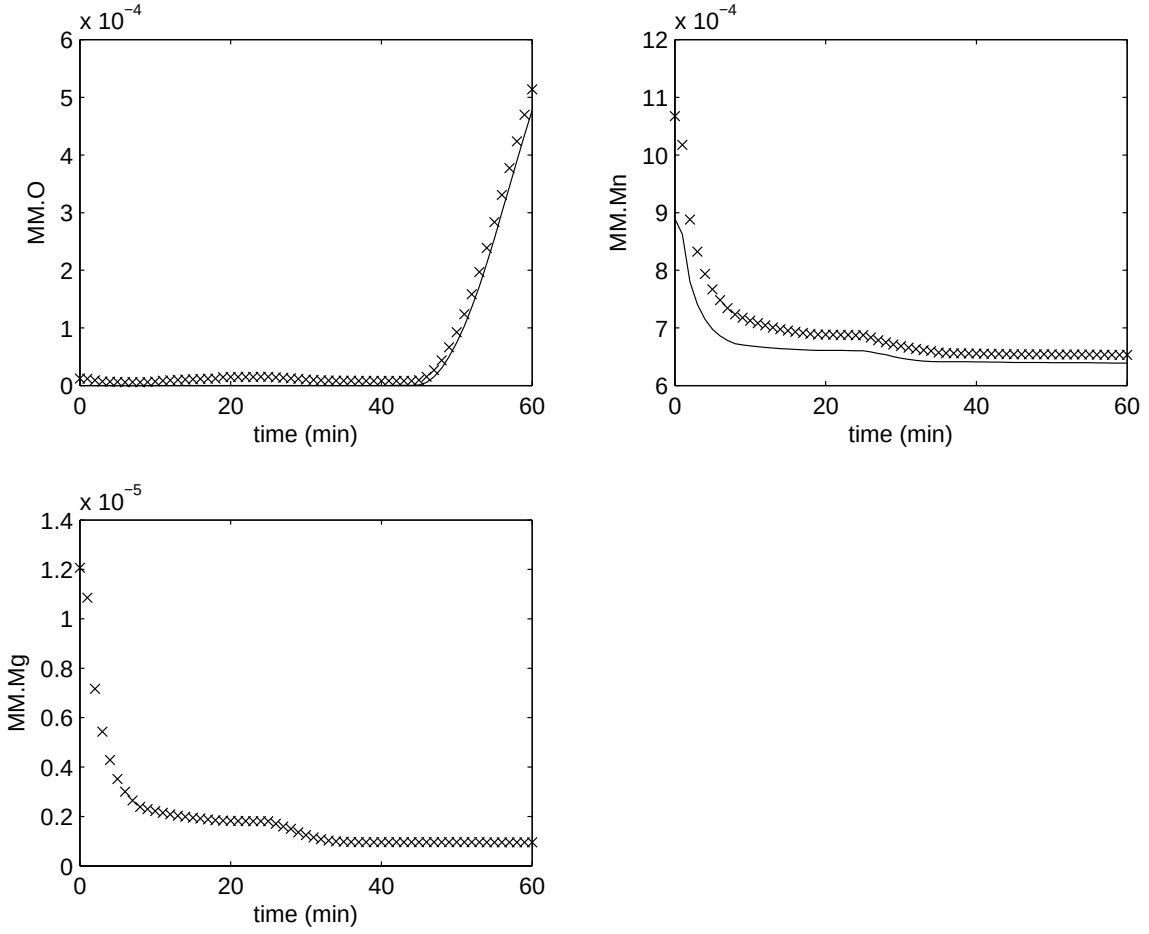

Figure C.32: Molten metal zone state profiles for the Case Study 2B with disturbance state augmentation. (×) represents the estimated states while (–) represents the actual states